Inelastic scattering studies of CO & O_2 for Astrophysical applications

Radboud Universiteit

Chandan kumar Bishwakarma
2018

Inelastic scattering studies of CO & O_2 for Astrophysical applications

Proefschrift

ter verkrijging van de graad van doctor
aan de Radboud Universiteit Nijmegen
op gezag van de rector magnificus prof. dr. J.H.J.M. van Krieken,
volgens besluit van het college van decanen
in het openbaar te verdedigen op vrijdag 9 februari 2018
om 10:30 uur precies.

door

Chandan kumar Bishwakarma
geboren op 7 juni 1984
te Parbelia Colliery (West Bengal, India)

Promotor:	Prof. dr. David H. Parker
Manuscriptcommissie:	Prof. dr. Jos Oomens (Radboud Universiteit Nijmegen, Voorzitter) Prof. dr. Bas Y. T. van de Meerakker (Radboud Universiteit Nijmegen) Prof. dr. Mark Brouard (Oxford University, Verenigd Koninkrijk)

Chandan kumar Bishwakarma, Inelastic scattering studies of CO & O_2 for Astrophysical applications
PhD Thesis, Radboud University, Nijmegen, The Netherlands
With summary in Dutch
Cover: (Front) Atom-molecule scattering and it's detection: Designed in Adobe iIlustrator
ISBN: 978-94-6295-825-8.
Printed by: ProefschriftMaken || www.proefschriftmaken.nl

The work presented in this thesis is financially supported by the European Union (EU) 7th framework programme ITN # 238671 'ICONIC' and Dutch Astrochemistry Network (DAN) by Nederlandse Organisatie voor Wetenschappelijk Onderzoek (NWO) Wetenschappelijk Onderzoek (NWO)

Inelastic scattering studies of CO & O_2 for Astrophysical applications

Doctoral Thesis

to obtain the degree of doctor
from Radboud University Nijmegen
on the authority of the Rector Magnificus prof. dr. J.H.J.M. van Krieken,
according to the decision of the Council of Deans
to be defended in public on Friday, February 9, 2018
at 10:30 hours

by

Chandan kumar Bishwakarma
born on June 7, 1984
in Parbelia Colliery (West Bengal, India)

Supervisor: Prof. dr. David H. Parker

Doctoral Thesis Committee:: Prof. dr. Jos Oomens
(Radboud Universiteit Nijmegen, Chair)
Prof. dr. Bas Y. T. van de Meerakker
(Radboud Universiteit Nijmegen)
Prof. dr. Mark Brouard
(Oxford University, United Kingdom)

Chandan kumar Bishwakarma, Inelastic scattering studies of CO & O_2 for Astrophysical applications
PhD Thesis, Radboud University, Nijmegen, The Netherlands
With summary in Dutch
Cover: (Front) Atom-molecule scattering and it's detection: Designed in Adobe iIlustrator
ISBN: 978-94-6295-825-8.
Printed by: ProefschriftMaken || www.proefschriftmaken.nl.

The work presented in this thesis is financially supported by the European Union (EU) 7th framework programme ITN # 238671 'ICONIC' and Dutch Astrochemistry Network (DAN) by Nederlandse Organisatie voor Wetenschappelijk Onderzoek (NWO).

To my Parents

Contents

Chapter 1

Introduction

1.1 Introduction

Understanding the processes that occurs during the collisions of atoms and molecules is the central goal of many branches of physics and chemistry. Collisional processes can lead to a transfer of momentum, of energy, of atoms, or of electrons and these are defined accordingly as elastic, inelastic, or reactive scattering, schematically shown in Figure 1.1. The outcome of a collision process depends on many variables, including the intermolecular potential $U(r)$, the impact parameter b, and the collision energy. Interaction at large impact parameters ($b \to \infty$) generally leads to elastic scattering, whereas interaction with smaller impact parameters leads to changes in internal degrees of freedom. In the elastic scattering kinetic energy and momentum is conserved after scattering. In inelastic scattering the collision energy between two colliding partners results in a rotational or vibrational excitation of the atoms and molecules. The chemical identity of the collision products' changes in reactive scattering processes. In recent years, there were tremendous advancements in quantum calculations describing the interaction between atoms and molecules and the scattering process. These quantum calculations are based on assumptions and approximation that still require experimental confirmation. Therefore, only the combined effort of experiments and theory ensure and widen the map of understanding of atom molecule interactions.

1.2 Importance of Rotational inelastic Scattering in Astrochemistry

Telescopes measure light emitted from objects in space such as visible light from stars but also light emitted in the infrared and microwave spectral regions from vibrationally and rotationally excited molecules, respectively. The microwave region is very interesting, especially for terrestrial telescopes such as the ALMA

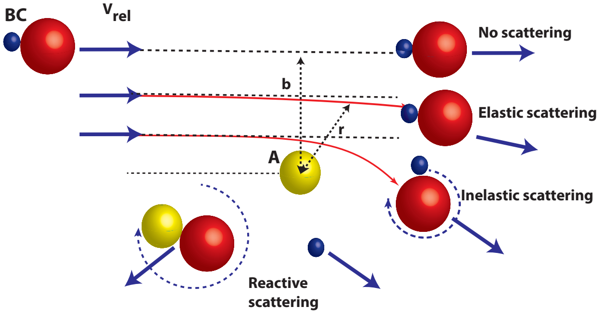

Figure 1.1: The picture shows the possible outcomes of a molecule (red-blue) interacting with a central atom (yellow). With an impact parameter b, the collision is defined as the perpendicular distance (r) between the path of a projectile and the center of a potential field $U(r)$ created by the interaction with the yellow atom as the projectile approaches.

array in Chile(1), because the Earth's atmosphere is relatively transparent in this spectral region. Molecules become rotationally excited due to collisions, primarily with H_2 and He, which are the most abundant molecules in space. It is safe to say that if there was no rotational inelastic scattering, we would know little to nothing about interstellar space, which is essentially our entire universe. The understanding of the molecular nature of the interstellar medium comes from spectroscopic observations. The gas density and the temperature in the region of a particular emitting species can be derived from the relative intensities of the rotational emission lines. To observe rotational transition in a molecule, the molecule must possess a permanent electric dipole moment. With the development of new spectroscopic techniques, CH, CH^+ and CN were the first molecules to be identified in the interstellar medium. Verification of these molecules were done by comparison with laboratory spectra. This is the case for almost all the interstellar molecules. However, there are few exceptions like H_2, CO_2 and HCCH. H_2 possesses no dipole moment and therefore shows no electric dipole-allowed rotational and vibrational transitions.

Molecular abundance in the interstellar space is defined relative to H_2 abundance. The spectroscopy of H_2 is complicated as the rotational levels are widely separated and its exists in para and ortho forms. H_2 can be observed via far-UV electronic transitions in the *Lyman* $B^1\Sigma_u^+ \rightarrow X^1\Sigma_g^+$ and *Werner* $C^1\Pi_u \rightarrow X^1\Sigma_g^+$ absorption bands below 111.5 nm(4), using the space-based far-UV spectrographs. CO_2 and HCCH possesses IR spectra corresponding to dipole-allowed transitions between their vibrational level. However, many of these frequencies are not observable in the earth atmosphere as these frequencies are absorbed. But these observations are enhanced by the use of spectrometers mounted on satellites such as the Infrared Space observatory and the Spitzer Space telescope(49).

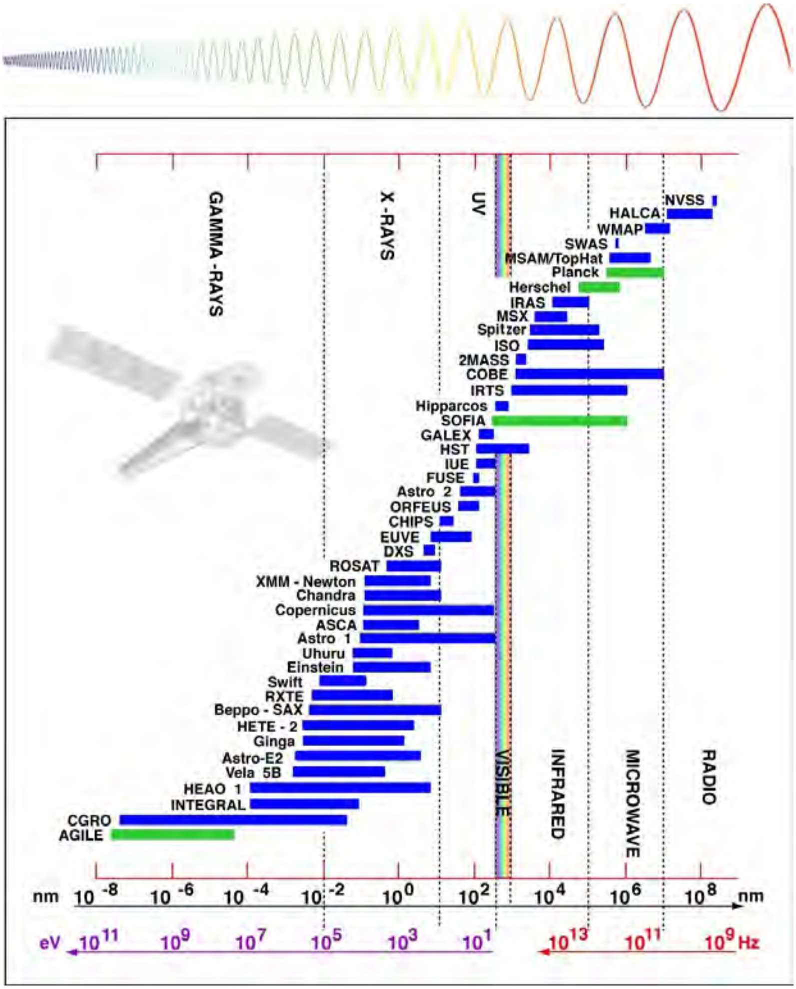

Figure 1.2: Space observatories and their wavelength working ranges as of 2005. This list is from The blue bar indicates a past/ current mission and the green bar represents a mission in development(Adapted from NASA -NSSDCA (2))

1.3 Importance of CO

Carbon monoxide (CO) is a small hetero-nuclear closed shell molecule. Carbon monoxide consists of one Carbon and one Oxygen atom connected by a triple bond. There is a net negative charge at the carbon end of the CO molecule and hence there is a very small dipole moment of 0.122 D. CO occurs naturally in the earth atmosphere. CO is also one of the major byproducts of the combustion process. It is the most abundant C-bearing molecule in the universe and therefore, a major sources of carbon compounds in the interstellar medium. It is the second most common molecule in dense interstellar clouds, after H_2. CO is one of the major constituents in the formation of methanol, which is often described as the building block of this cosmos. It is found in comets and the atmospheres of several planets. CO has also been detected in brown dwarfs such as Gliese 229b(97) and Epsilon Indi B(110) since 1952, it is known that CO is present in the atmosphere of our own sun, residing in the chromospheres. CO $v = 1 - 0$ ro-vibration transition near 4.7 μm is commonly observed from low and high-mass star-forming regions, proto-planetary disks and external galaxies. Infrared space observatories have detected a large number of CO rovibrational lines in Orion's peak 1 & 2(53). CO is observed in the interstellar media by means of its characteristic rotational spectrum. It is used as a surrogate for detecting molecular hydrogen and is consequently used extensively for mapping molecular clouds in our own galaxy and elsewhere(135; 111; 108). Apart from CO being a major molecule in astrochemistry, it is also a very useful prototype molecule widely used for basic research.

1.4 Importance of O_2

Molecular oxygen (O_2) is one of the most important molecules in our daily life and in our atmosphere. O_2 is responsible for blocking vacuum ultra violet (VUV) light from the solar spectrum at a height of 80-110 km above the earth atmosphere. O_2 is a homonuclear open shell molecule. It has no dipole moment and is extremely hard to probe by standard optical spectroscopy due to strict symmetry. Therefore, it possesses very difficult challenges in molecular photochemistry. Still, O_2 is very attractive due to its multiplet structure arising from the outer electronic shell. Oxygen is the third most common element in the universe after hydrogen and helium and the third most common interstellar molecule after H_2 and CO. Molecular oxygen was detected in the star-forming region of the Orion Nebula with combined effort of Herschel's space laboratory, European space agency and NASA(52). B. Larson et al reported molecular oxygen in the ρ Ophiuchi cloud at 118750.343 MHz (72). Discovery of O_2 in the interstellar space can help to determine what role the molecule plays in cloud cooling, which is considered as an important step in star formation. O_2 emission from the comet 67P/Churyumov-Gerasimenko was discovered by the high resolution mass spectrometry of the Rosetta space probe. They observed peak at mass 32, corresponding to oxygen mass and the high resolution of the spectrometer made it possible to distinguish it from sulphur(19).

1.5 Motivation of this thesis

The potential energy function $U(r)$, represented as a multi-dimensional potential energy surface (PES), is the critical part of astrophysical models. Sufficiently accurate potential energy surfaces are difficult to calculate and measurements that can directly validate the theory by comparing the prediction with experimental data are equally challenging. Recent studies using the velocity map imaging method(41) to study inelastic collisions, particularly those under crossed molecular-beam conditions, now make it possible to directly observe the detailed outcome of energy transfer processes under well-specified conditions. The crossed molecular-beam technique is one of the well-established experimental tools used to study collision transfer processes. The crossed molecular-beam technique was improved and applied particularly by Dudley Herschbach and Yuan T. Lee, for which they were awarded the 1986 Nobel Prize in Chemistry(73) along with John Polyani for his work on IR chemiluminescence of reaction products(3). With recent development of new detection schemes, researchers using the molecular-beam method are now able to explore increasingly subtle dynamics of interaction between atoms and molecules, to the point now that the simplest atom-molecule scattering processes are “perfectly” understood. The experimental breakthroughs that allowed this include the ion imaging method, invented by Chandler and Houston(36). The discovery of velocity map imaging (VMI) by Eppink and Parker(102) greatly enhanced the ion imaging resolution. VMI provides the so-called state-to-state differential cross section (DCS) for any two-body process in chemistry, including photodissociation, photoionization, and scattering events. As described later in this thesis, the DCS measured using VMI in a cross-molecular-beam setup that provides data for the most stringent tests of state-of-the-art theoretical quantum calculations used to model collisions. In order to extract quantitative information from telescope measurements of interstellar space, a good astrophysical model is necessary. This in turn depends on the accuracy of the potential energy surface (PES) employed. PES is constructed with the quantum scattering calculations. The differential cross-section measurements from our experiments are used to test and confirm the accuracy of the PESs and thus the quality of models used by astronomers or astrophysicists to interpret their astronomical data. Detection of new molecules in the interstellar space continues to provide new challenges to the theorist and experimentalist involved in astrophysical modeling. With the development of new techniques and better computational capacities, there has been a success in modeling progressively for larger molecules. Previously, there also was a lot of progress in molecular-beam energy transfer experiments. The discovery of new features in atom molecule interaction continued to inspire the scientist to explore further. Many in-depth studies of the scattering of the open shell NO molecules were performed with rare gases. A great amount of work

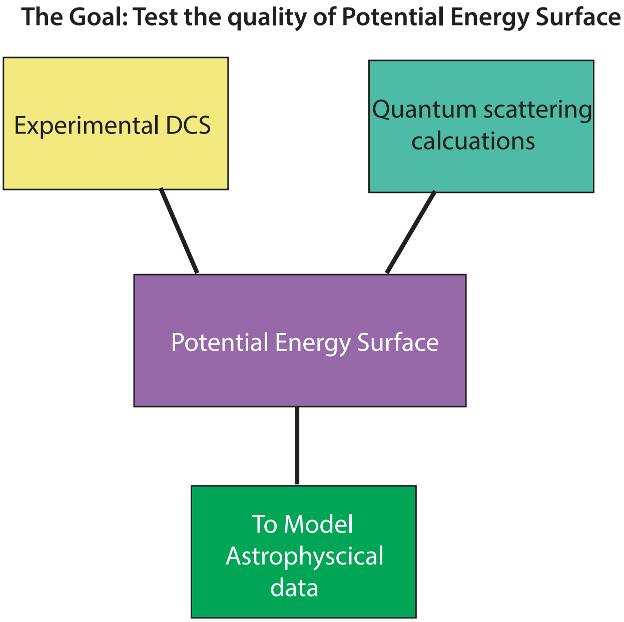

Figure 1.3: Schematic representation of the motivation of this thesis.

for the NO system was done by the group of Brouard(25; 27; 31; 26; 30), which has provided great experimental and theoretical detailed insight in atom-molecule interaction. With the development of state-of-art technique like Stark deceleration has pushed the limits of velocity map imaging (VMI) which in turn provided great insight into quantum interference in differential cross section. The group of van de Meerakker(127; 125; 98; 70) in Nijmegen has demonstrated such DCS images showing quantum interference effects. The ability to carry out low energy inelastic scattering studies and to use a sensitive detection method has been the bottleneck in these fields. With the development of state-of-art Stark deceleration technique in combination with better detection scheme like vacuum ultra violet (VUV) ionization has opened the window of opportunities to further studies in these fields.

In this PhD project, we have studied inelastic scattering of CO and O_2 with rare gases. Butz et al(33) reported one of the earliest molecular-beam experiments on CO-He in 1971. In 1975, Nerf et al(94) presented the first experimental evidence about the anisotropy of the CO-He potential. Anatonova et al(8) measured relative state-to-state integral cross sections for rotational excitation of CO with He at collision energies at 583 and 720 cm^{-1}. Lorentz et al also measured the state-to-state differential cross sections of CO collision with Ne at collision energy at 511 cm^{-1}(9). The work reported in this thesis presents the collision-induced alignment studies of CO with Ar and He. With the application of VUV detection scheme, we present an elegant demonstration of imaging the collision-induced alignment effect in inelastic scattering of CO with Ar and

He.We have used a novel means of analyzing velocity map images of angular momentum polarization in inelastic scattering.
This thesis also reports work on state-to-state differential cross sections of inelastic scattering of O_2 with He, which is also challenging system for both theory and experiment. Luzzati et al reported experimental investigation of rotational energy transfer in O_2 with He, Ne, Ar, Kr, and Xe.(82) The total differential cross sections (DCS) for the scattering of O_2 by He was performed by Beneventi et al.(17) DCSs with well resolved diffraction oscillations for Ne-O_2 collisional system was measured by Beneventi et al.(16) Faubel et al performed crossed molecular beam experiments for the Ar-O_2 collisional system and obtained individual rotational state-to state transitions(107; 46). Chefdeville et al reported state-to-state integral cross sections (ICSs) in a highly advanced crossed beam experimental study of O_2-H_2 at low energy and observed partial wave resonances that were in very good agreement with the theoretical predictions(38).

1.6 A brief summary of works

In this thesis, we have studied the imaging of crossed-beam scattering with a focus on imaging collision-induced alignment effects of CO with rare gases as well as the inelastic scattering of O_2 with He. We performed a crossed molecular-beam experiment to probe rotational excitation of CO due to scattering with Ar and He. Velocity map imaging (VMI) was combined with state-selective detection by (2+1) & $(1 + 1^{'} + 1^{''})$ resonance enhanced multi-photon ionization (REMPI) using Vacuum ultraviolet (VUV) as the laser light source. Differential cross sections were extracted from experimental image after density-to-flux corrections. The measured DCSs were compared with DCSs obtained from theoretical calculations. The DCS extracted for different collisional partners of CO reflects the nature of interaction of each system and reveals the dynamics of the process. We have placed the emphasis on an angle-resolved measurement of collision-induced alignment and show that the VUV laser probe is particularly sensitive to alignment effects. In this work, tunable VUV radiation around 150 to 154 nm was produced by resonant four-wave difference frequency mixing in Xe gas. We have probed the scattered products with horizontal and vertical VUV probe laser polarization. The results obtained from the experiment shows a strong collisional-induced alignment effect in CO colliding with Ar and He. Similarly, we have studied the inelastic scattering of O_2 with He and H_2. For this, it was first necessary to better understand the REMPI process for O_2 before performing inelastic scattering of O_2 with He and H_2.
Chapter 3 presents a novel means of analyzing velocity map images of angular momentum polarization in inelastic scattering. Without any detailed analysis using fitting or basis function, the alignment moment can be directly extracted from linear combination of angular distribution obtained from two-laser polarization.

Chapter 4 presents imaging studies of collision-induced alignment effects for inelastic scattering of CO with Argon using velocity map imaging. Rotationally excited carbon monoxide (CO) was detected with state-selective detection by $(1 + 1^{'} + 1^{''})$ VUV (vacuum ultra violet) REMPI (Resonance enhanced multi photon ionization) scheme. The detected CO molecule was imaged in a crossed-beam experimental setup using velocity map imaging (VMI). The scattered CO molecule was detected with Vertical (V) and Horizontal (H) polarization of VUV radiation. The detected scattered image shows remarkable differences in appearance, which manifest strong collision-induced alignment effect. Good agreement between theory and experimental results shows the reliability of this experiment.

Chapter 5 presents detailed study of state-to-state rotationally inelastic polarization dependent differential cross sections (PDDCS) of scattering for CO collision with He. It contains a detailed study of the differential cross sections obtained in the 2+1 and $(1 + 1^{'} + 1^{''})$ REMPI detection scheme. Like CO-Ar system, CO-He also shows strong collision-induced alignment effect.

Chapter 6 presents state-to-state inelastic scattering of O_2 due to scattering with helium with a collision energy of 660 cm^{-1}. Velocity map imaging was combined with state-selective detection of O_2 $X^3\Sigma_g^-$ by (2+1) resonance enhanced multi-photon ionization. The obtained raw O_2^+ images were first corrected from density-to-flux and the differential scattering cross sections (DCS) were then extracted for six different O_2 final states. Exact theoretical quantum mechanical calculations were also performed. A very good agreement between experimental and theoretical DCSs was found for all final state data using an initial O_2 molecular-beam population ratio of 80% for the first rotational state and 20% for the first excited state. The agreement clearly demonstrates the ability to model both theoretically and experimentally inelastic processes between O_2 molecules and rare gases.

Chapter 2

Experimental methods

Abstract: This Chapter describes the key concepts, and the experimental methodology used for the research work described in this thesis. This Chapter gives a brief description of kinematic apse model which can be qualitatively used to explain collision-induced alignment effects. A complete description of the crossed-molecular beam experimental setup with velocity maps imaging is also presented. Furthermore, this chapter describes the state preparation of O_2 and CO which are the key study items of this thesis for collision scattering experiment. It includes a full description about the VUV (Vacuum ultra violet) set-up used in the experimental work in this research where we have used a four-wave mixing technique in order to produce VUV photons. An overview of the data analysis method is presented for the density-to-flux correction. The last section describes the possible errors in the collision experiment due to various factors.

2.1 Rotational energy transfer

After collision a molecule will only rotate if the molecule experiences a torque in a period of time. When a force acting upon a molecule does not pass through the centre of mass then it can be expressed as the product of force and the shortest distance between the line of force and center of mass. If the torque F, acts for a time Δt, then there is a change in angular momentum Δp which can be expressed as

$$\Delta p = \hbar \Delta j = I \Delta \omega = F \Delta t \tag{2.1}$$

where I is the moment of inertia and $\Delta\omega$ is the change in angular velocity. Change in angular momentum can also be expressed in unit of $\hbar$ and rotational quantum number j. The change in rotational energy produced by the torque can also be expressed as

$$\Delta E = \frac{1}{2} I (\omega_0 + \Delta\omega)^2 - \frac{1}{2} I \omega_0^2 \approx I \omega_0 \Delta\omega, \tag{2.2}$$

where ω_0 is the initial angular velocity. Equation 2.2 can be alternatively expressed as

$$\Delta E = \frac{\hbar^2 (j_0 + \Delta j)^2}{2I} - \frac{\hbar^2 j_0^2}{2I} \approx \frac{\hbar^2 j_0 \Delta j}{I} \tag{2.3}$$

The equation 2.3 shows that for a large moment of inertia, a torque, which results in a significant change in j, may produce a negligible amount of change in rotational energy. For a diatomic molecule to experience rotational energy change, it should experience torque. The torque is determined by the intermolecular potential. For long range interaction, the torque experienced is weak. For short-range interaction, it probes the more anisotropic parts of the potential which results in a strong torque. Classically, we can say that the change in rotational states is mainly due to short-range repulsive forces of the potential.

2.2 Differential and integral cross-sections

Collision energy transfer is an important and ubiquitous process that keeps the world at a thermal equilibrium. Collision experiments, particularly those using crossed molecular-beams, allow to directly observe the detailed outcome of energy transfer process under well specified conditions. The amount of energy transfer depends upon the collision energy and the nature of scattering reflects the interaction between two scattering partners.

Consider a simple collision system of two collision partners, A and BC, of the masses m_1 and m_2, respectively, as shown in Figure 2.1. Let vectors $\boldsymbol{v_1}$ and $\boldsymbol{v_2}$ be the velocities of the two reactants w.r.t. the lab frame. The relative velocity $\boldsymbol{v_{rel}}$ is defined as

$$\boldsymbol{v_{rel}} = \boldsymbol{v_1} - \boldsymbol{v_2} \tag{2.4}$$

Classically, the impact parameter b is defined as the distance of the closest approach in the absence of any interaction. The magnitude of the orbital angular momentum, ℓ is defined in terms of b and μ.

$$|\ell| = \mu.v_{rel}.b \tag{2.5}$$

where $\mu = \frac{m_1.m_2}{(m_1+m_2)}$ is the reduced mass of the two reactants.
The outcome of scattering between two reactants is a function of b and thus the orbital angular momentum ℓ. Collisions with a high-impact parameter lead to low transfer of energy i.e. fewer reaction probabilities as compared to that of a head-on collision with a small impact factor. If the reactants are not orientated in space, then the probability of scattered products becomes independent of the azimuthal angle ϕ. Therefore, the cross section σ of a reaction probability is defined as

$$\sigma = \int_0^{2\pi} \int_0^{b_{max}} P(b) b db d\phi = \int_0^{b_{max}} P(b) 2\pi b db \tag{2.6}$$

where P(b) is the reaction probability as a function of b.
For head-on collision b=0 and for b=b_{max} the collision becomes too glancing. The angular distribution of the scattered products is independent of the azimuthal angle ϕ, provided the reactants are randomly oriented in space. The differential cross section, $d\sigma/d\omega$, is the effective target area of the colliding particles that leads to scattering into a particular angular range, $d\omega$. The angular range is defined in terms of the solid angle ω, with $d\omega = sin\theta d\theta d\phi$. Therefore, the angular probability distribution $P(\theta, \phi)$ can be expressed in terms of the differential cross section

$$P(\theta, \phi) = \frac{1}{\sigma} \frac{d\sigma}{\omega} \tag{2.7}$$

where $P(\theta, \phi) sin\theta d\theta d\phi$ is the probability of scattering into the solid angle in the range $\theta \to \theta + d\theta$ and $\phi \to \phi + d\phi$. The integral cross section can be obtained by integrating the differential cross sections over all solid angles.

$$\sigma = \int_0^{2\pi} \int_0^{\pi} \frac{d\sigma}{d\omega} sin\theta d\theta d\phi \tag{2.8}$$

We obtained differential cross sections from our experimental images after density-to-flux transformation. From these experiments we got a relative or normalized DCS. From this experiment, we cannot extract absolute integral cross sections as one needs accurate measurements of the densities of the molecular-beam and the collision volume, which is very difficult to measure.

2.3 Scattering in the center of mass frame and the laboratory frame

After the collision process, the scattered products are recorded in the lab frame, which is determined by the geometry of the experimental setup. In

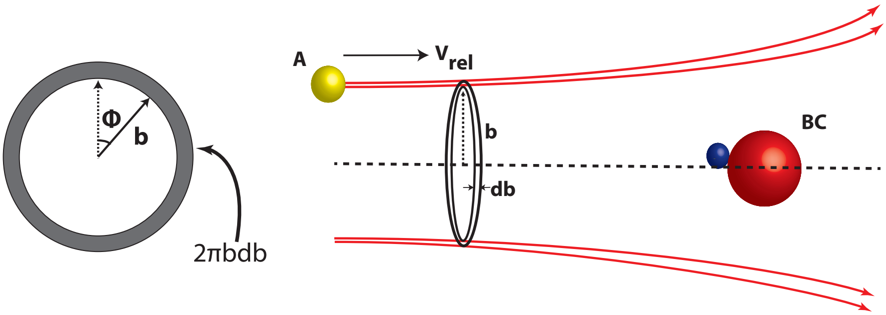

Figure 2.1: Example of the approach of the two reactants A and BC with the masses m_1 and m_2 respectively, at a well-defined impact parameter b.

order to extract the angular distribution information, the experimental data are converted from the lab frame to the center of mass frame (CM). The pictorial representation showing the relation between laboratory and CM frame is defined as a Newton diagram (Figure 2.2). The name was coined by Dudley Herschbach after Sir Isaac Newton whose law of motion governs the asymptotic behavior of reactants.

Scattering distributions in the center of mass frame are independent of the experimental geometry, which allows comparison of different types of experiments. In the center of mass frame, the observer is traveling along with the center of mass of the system. The transformation from the lab frame to the center of mass frame can be obtained from their geometries and velocity vectors. Let $\boldsymbol{v_1}$ & $\boldsymbol{v_2}$ be the velocities of the two colliding partners in the lab frame. The center of mass frame $\boldsymbol{u_1}$ and $\boldsymbol{u_2}$ are the velocities of the two colliding partners. The relation between the velocity vectors of two colliding partners in the center of mass frame to the lab frame is

$$\boldsymbol{V_{cm}} = \frac{m_1\boldsymbol{v_1} + m_2\boldsymbol{v_2}}{M} \tag{2.9}$$

$$\boldsymbol{u_1} = \frac{m_2}{M}\boldsymbol{v_{rel}} \tag{2.10}$$

$$\boldsymbol{u_2} = -\frac{m_1}{M}\boldsymbol{v_{rel}} \tag{2.11}$$

where M is the total mass of the system, $\boldsymbol{V_{cm}}$ is the center of mass velocity and $\boldsymbol{v_{rel}}$ is the relative velocity. The relative velocity is expressed as

$$\boldsymbol{v_{rel}} = \boldsymbol{u_1} - \boldsymbol{u_2} = \boldsymbol{v_1} - \boldsymbol{v_2} \tag{2.12}$$

$\boldsymbol{v_{rel}}$ is the relative velocity vector before collision and an observer moving along with the center of mass will observe two colliding partners of lab frame approaching along the relative velocity vector. After collision, the observer will see that they are moving away along the $\boldsymbol{v'_{rel}} = \boldsymbol{v'_1} - \boldsymbol{v'_2}$, the relative

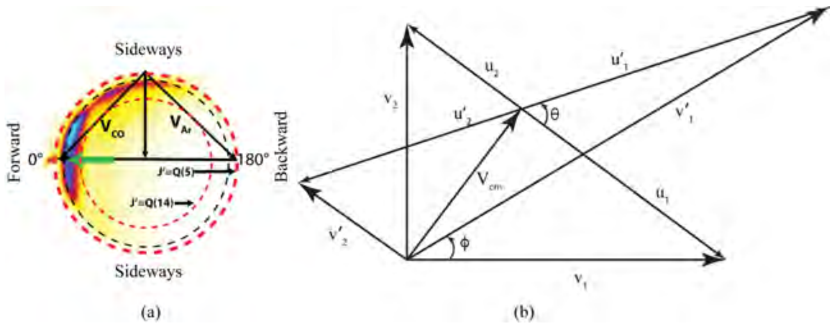

Figure 2.2: (a) The scattering image with a Newton diagram indicating forward, sideways and backward scattering. (b) The Newton diagram showing relation between center of mass frame and lab frame. Prime represents the post collision process and θ and ϕ represents the deflection angle between center of mass frame and lab frame respectively.

velocity vector. The angle between relative velocity vectors (pre-collision and post-collision) is defined as the center of mass scattering angle θ. Similarly, for the post-collision process the scattered product velocity can be given as

$$\boldsymbol{v'_1} = \frac{m_2}{M}\boldsymbol{v'_{rel}} \tag{2.13}$$

$$\boldsymbol{v'_2} = -\frac{m_1}{M}\boldsymbol{v'_{rel}} \tag{2.14}$$

Therefore, the relative kinetic energy $KE^{'}$ can be expressed as

$$KE^{'} = KE - \Delta E = \frac{1}{2}\mu \boldsymbol{v'_{rel}}^2 \tag{2.15}$$

Where $KE = \frac{1}{2}\mu \boldsymbol{v_{rel}}^2$, is the initial kinetic energy and ΔE is the energy used in excitation or de-excitation process in the scattering process.

2.4 Detection of Angular Momentum Alignment

Ion imaging with polarized laser light can provide great insight into the angular distribution of angular momentum polarization. Ionization probability is directly proportional to the scattered product angular momentum **J** and the probe laser polarization. The rotational angular momentum vector **J** is aligned if the **J** vector has preference to some reference direction but we cannot distinguish between directions. If **J** has a preferred direction then the rotational angular momentum vector **J** is said to be orientated. Therefore, in order to measure angular momentum polarization of scattered molecules, specifically its orientation and alignment, a common approach is to determine the related alignment moments(27). Based on the formalism of Fano and Macek,(45) the

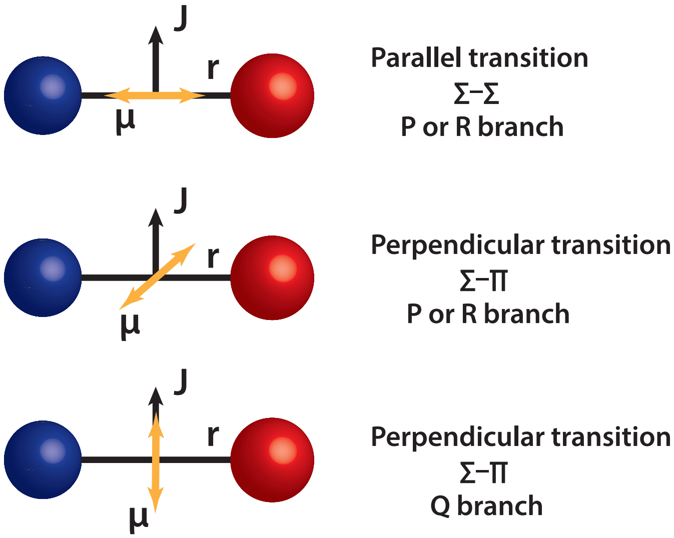

Figure 2.3: Schematic representation of P, R and Q transition. In the P and R transition the dipole moment $\boldsymbol{\mu}$ is perpendicular to $\boldsymbol{J}$ and for Q branch transition dipole moment $\boldsymbol{\mu}$ is parallel to $\boldsymbol{J}$

absorption cross-section $I(j^*, j^{'}, \theta, \phi, \chi_p)$ for linear polarized light in the probe frame can be written as

$$I(j^*, j^{',\theta}, \phi, \chi_p) = C_{det}\left\{1 - \frac{1}{2}h^{(2)}(j^*, j^{'})\left[A_0^{(2)}(j^{'}, \theta, \phi, \chi_p) - 3A_{2+}^{(2)}(j^{'}, \theta, \phi, \chi_p)\right]\right\} \tag{2.16}$$

In this equation C_{det} is the sensitivity constant, $j^{'}$ is the rotational quantum number of the scattered product prior to laser ionization and j^* denotes the resonantly excited rotational level. Here $h^{(2)}(j^*, j^{'})$ is a line strength factor depending on the branch of the spectra being probed. For a R branch $h^{(2)}(j^{'}+1, j^{'}) = -j^{'}/(2j^{'}+3)$, for a P branch $h^{(2)}(j^{'}-1, j^{'}) = (-j^{'}+1)/(2j^{'}-1)$, and for a pure Q branch $h^{(2)}(j^*, j^{'}) = 1$. $A_0^{(2)}$ and $A_{2+}^{(2)}$ are the alignment moments of the angular distribution of $j^{'}$ defined by the detector laser in probe frame(25; 26). For the P and R branch transitions, the transition dipole moment $\boldsymbol{\mu}$ is perpendicular to **J**, and for the Q branch the transition dipole moment $\boldsymbol{\mu}$ is parallel to **J**. Only those molecules whose transition dipole moments are aligned with the $\boldsymbol{\varepsilon}$ vector of the linearly polarized light, can absorb the radiation dependent on the absorption probability $\boldsymbol{\varepsilon}.\boldsymbol{\mu}$, where $\boldsymbol{\varepsilon}$ is the electric vector of the absorbed radiation.

In order to gain more insight, the alignment moment from the probe frame can be rotated to the collision frame by the rotation matrices given by Hertel and Stoll(58). A distribution is isotropic when all three alignment moments equal zero i.e.$j^{'}$ has no preferred direction. The value of $A_0^{(2)}$ reflects the alignment propensity of $j^{'}$. The value of $A_0^{(2)} = 2$ corresponds to $\mathbf{v} \| \mathbf{J}$ while $A_0^{(2)} = -1$ corresponds to $\mathbf{v} \perp \mathbf{J}$. The value of $A_{2+}^{(2)}$ reflects the extent of the alignment of the $\mathbf{J}$ vector.

An experimental image signal can be written as the product of DCS and detection probability:

$$I(\theta) = \frac{d\sigma}{d\theta}(\theta) P(\theta; \chi, \Theta, \phi), \tag{2.17}$$

where $P(\theta; \chi, \Theta, \phi)$ is the polarization-dependent transition probability which, depends on angular momentum polarization and the probe sensitivity. It can be expressed as:

$$P(\theta; \chi, \Theta, \phi) = C\Big[1 + \sum_{kq} A_q^{(k)}(\Theta) F_q^{(k)}(\chi, \Theta, \phi)\Big] \tag{2.18}$$

C is a constant, $F_q^{(k)}(\chi, \Theta, \phi)$ depends on the geometric factor that incorporates the probe sensitivity determined by the angles (χ, Θ, ϕ). The outcome of the DCS from the experimental signal, which depends on the laser polarization, is termed as polarization-dependent differential cross sections (PDDCS).

2.5 Kinematic Apse Model

There have been only a few experimental and theoretical investigations addressing rotational polarization or alignment effects. Cline et al(39) and Wade et al(129) experimentally measured the collision-induced alignment effect of the NO(X) in collisions with rare gas atoms. For lower rotational states, the experiment and theory matched reasonably. Aoiz et al used quasi-classical trajectory in order to investigate rotational polarization effects(10). The work of Lemeshko et al mainly described the alignment effect in the forward scattering region using the Fraunhofer diffraction model(74). The model accurately describes the oscillations in extreme forward scattering but says very little about alignment at sideways and backward scattering. Jambrina et al studied collision-induced orientation effects using a canonical collision mechanism theory(64). The group of Brouard extensively studied collision-induced alignment effect in NO(X)- Ar inelastic collisions(25; 31; 26). They investigated rotational angular momentum alignment effects in the rotational inelastic scattering of NO(X) with Ar by using close-coupled quantum mechanical, quasi-classical trajectory and Monte Carlo hard shell scattering calculations. It has been shown that rotational alignment in NO(X)-Ar inelastic collision is due to the hard shell nature of the probed part of the interaction potential. A kinematic apse model was tested and compared with quantum-mechanical calculations. Both were found to be in good agreement at collision energies with reasonable access of well depth. At lower collision energy, the attractive part of the potential plays an important role in the alignment dynamics.

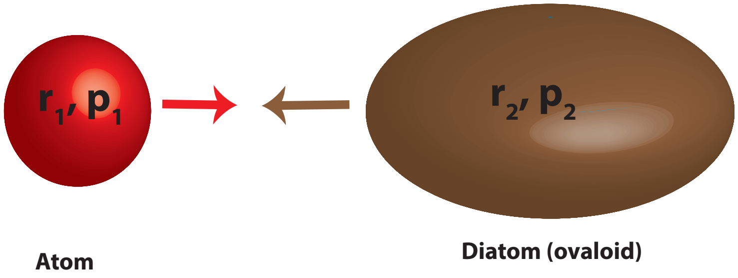

Figure 2.4: Schematic representation of a collision between hard sphere (r_1,p_1) *and a hard ovaloid* (r_2,p_2)

Khare et al(67; 66) were able to show that the component of angular momentum along particular quantization axis is the outcome of a collision between hard sphere and a hard ovaloid. They considered a simple picture of a classical impulsive collision between an atom and a rigid rotor as shown in Figure 2.4. The total angular momentum can be described as

$$\boldsymbol{J} = \boldsymbol{r_1} \times \boldsymbol{p_1} + \boldsymbol{r_2} \times \boldsymbol{p_2} + \boldsymbol{j} \tag{2.19}$$

where $\boldsymbol{j}$ is the angular momentum of the diatom and the subscript 1 and 2 denote the molecule and atom. In the impulsive collision the total angular momentum is conserved i.e. $\Delta\boldsymbol{J} = 0$, then one can write

$$0 = \Delta\boldsymbol{J} = \Delta(\boldsymbol{R} \times \boldsymbol{p}) + \Delta\boldsymbol{j} \tag{2.20}$$

where the relative scattering vector $\boldsymbol{R}$ is defined as $\boldsymbol{R} = \boldsymbol{r_1} - \boldsymbol{r_2}$ and the relative linear momentum $\boldsymbol{p}$ is defined as $\boldsymbol{p} = \mu(\boldsymbol{v_1} - \boldsymbol{v_2})$ where μ is the reduced mass. As the impulse collision is for a very short time, therefore, there is no change in collision geometry. Hence, one can write

$$\Delta\boldsymbol{j} = -\Delta(\boldsymbol{R} \times \boldsymbol{p}) \tag{2.21}$$

If we define the unit vector $\hat{\boldsymbol{a_k}}$ along the impulse i.e. along the momentum transfer vector $\Delta\boldsymbol{p}$ then

$$\hat{\boldsymbol{a_k}} \cdot \Delta\boldsymbol{j} = 0 \tag{2.22}$$

we call this vector kinematic apse

$$\hat{\boldsymbol{a_k}} = \frac{\boldsymbol{p}' - \boldsymbol{p}}{|\boldsymbol{p}' - \boldsymbol{p}|} = \frac{\Delta\boldsymbol{p}}{|\Delta\boldsymbol{p}|} \tag{2.23}$$

where $\boldsymbol{p}'$ and $\boldsymbol{p}$ are the initial and final relative momentum(see Figure 2.5). In the case of non-reactive collisions, $\boldsymbol{p}'$ and $\boldsymbol{p}$ can be substituted by $\boldsymbol{k}$ and $\boldsymbol{k}'$ as initial and final relative velocities. In a sudden collision, where the molecular axis remains unchanged during interaction, the projection of the initial and final rotational angular momenta j and j' onto the kinematic apse are equal. This

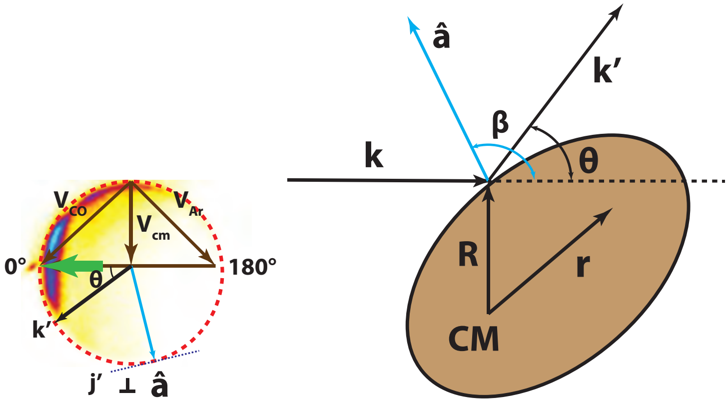

Figure 2.5: The left panel shows the Newton Diagram of a CO-Ar collision system. The scattering vector $\boldsymbol{k}^{'}$ *(black line) indicate the scattering vector in the center of mass frame under an angle* θ. $\hat{\boldsymbol{a}}_{\boldsymbol{k}}$ *is the kinematic apse vector (blue line) corresponding to the drawn scattering vector* $\boldsymbol{k}^{'}$. *A thin dotted line (dark blue) is drawn perpendicular to the kinematic apse vector. The right hand panel shows the diagram of the scattering between atom-hard shell ellipsoid in two dimensions. Generally the kinematic apse bisects the incoming* $\boldsymbol{k}$ *and outgoing* $\boldsymbol{k}^{'}$ *scattering vector in elastic collision but it is different for inelastic scattering.*

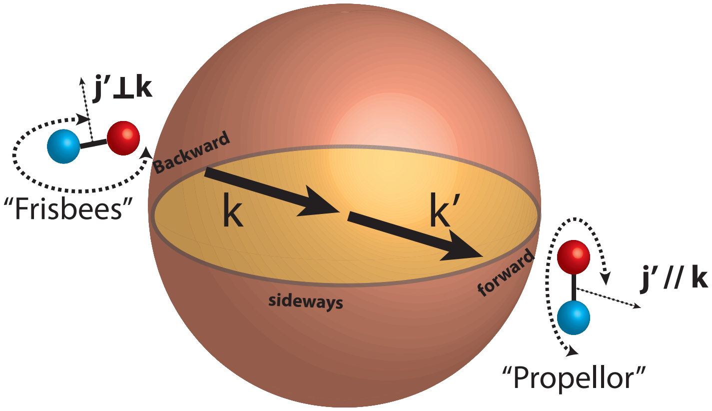

Figure 2.6: Pictorial representation of the 'frisbees' and 'propeller' rotation depending on the $j^{'}$ *orientation with respect to the initial relative velocity* $\boldsymbol{k}$. *In the forward direction, the scattered CO rotates like propellers* ($j' \parallel k$) *and like frisbees* ($j' \perp k$) *in the backward direction.*

conservation is the basis of the kinematic apse model. The information about rotational alignment in collisions of a classical hard shell can be determined by the projection of the rotational angular momentum on the kinematic apse(61). In Figure 2.5, $\hat{\boldsymbol{a_k}}$ is the kinematic apse drawn with respect to $\boldsymbol{k}'$. The angle β is defined as the apse angle between $\hat{\boldsymbol{a_k}}$ and $\boldsymbol{k}$.
In the case of an impulsive collision, there is no change in the collision geometry. Therefore, j' should have a zero projection on the kinematic apse i.e. j' is perpendicular to the kinematic apse $\hat{\boldsymbol{a_k}}$ irrespective of the scattering angle θ and final state. The degree of alignment depends on the position of collision impact, the amount of initial momentum, and the direction of the apse $\hat{\boldsymbol{a_k}}$. One of the common features of the differential cross section is that the scattering gradually changes from forward to backward scattering as a function of Δj. At lower Δj, j' is parallel to the initial relative velocity. The extent of j' being aligned parallel to $\boldsymbol{k}$ reduces with increasing Δj. With an increase in Δj, j' becomes more and more perpendicular to the apse direction. The general trend of the $A_0^{(2)}$ is that it is positive in the forward direction and becomes negative in the backward direction reveals that the origin of the angular momentum polarization is impulsive. In the forward direction CO rotates like propellers and in backward direction CO rotates like frisbees as shown in the Figure 2.6.

2.6 Velocity Map Imaging

The birth of the ion imaging method is from a 1987 paper by Chandler and Houston(36). The next major development came in 1997 with the technique of the velocity map imaging (VMI) by Eppink and Parker(41). In this method, an electrostatic lens set at a certain ratio of voltage is used to achieve momentum focusing i.e. all the ionized particles with the same velocity irrespective of their origin in the ionization volume are mapped into the same point on a two-dimensional detector surface. This method gave better resolution than ion imaging method. Since then, VMI became one of the major techniques in the world for chemical dynamics, especially in cross beam scattering experiments. In our collision experiment the scattered products are rotationally excited and ionized by a laser. The 3-D Newton sphere of these scattered ionized products is projected onto a 2-D detector. The mapped image gives us the angular distribution. Figure 2.7 shows the schematics and concept of velocity map imaging. In context to the experimental project for this thesis, rotationally excited CO and O_2 were detected by velocity map imaging using resonance enhanced multi photon ionization technique (REMPI). Velocity map imaging basically includes ion optics, a time of flight tube, and a 2-D detector that consists of micro channel plates (MCP) and a phosphor screen. The ion optics include a repeller, extractor and a ground electrode plate. These flat circular electrode plates along with the 2-D detector lies parallel to the collision plane of our scattering studies. The time-gated 2-D position sensitive detector (Advanced Performance Detector, Burle) consists of a $Chevron^{TM} - MCP$ (micro channel plate) and a phosphor screen (PS) of 40 mm diameter. Charged

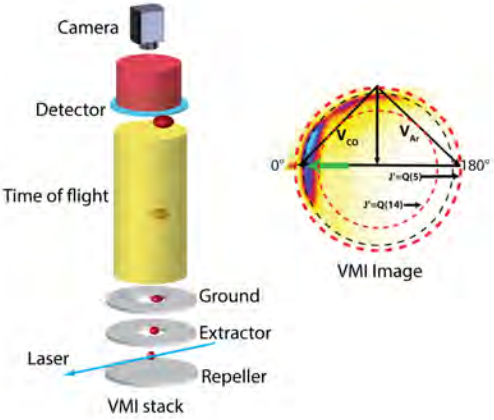

Figure 2.7: Schematic description of the velocity map imaging detection with ion optics (repeller, extractor and ground electrodes), time of flight, MCP detector, and a camera. On the right side is an example of the velocity-mapped image with its Newton diagram.

particles or photons collide with the front face of the first MCP and are converted to electrons. The P20 phosphor screen is composed of (Zn, Cd)S:Ag, which emits yellow-green photons in the wavelength range between 470–670 nm. The light signals from the phosphor screen are transferred from the vacuum by a fiber optic link and collected by the CCD (charged coupled device) camera. This CCD camera has a VGA resolution (640x480 Pixel), the CCD sensor has a monochrome output and the spectral range of the CCD is between 280–1000 nm. Inelastic scattering studies of CO and O_2 were performed. The scattered products were ionized by the REMPI process and with the method of velocity map imaging, we collected the angular distribution of the scattered products. The data acquisition was performed using a data acquisition and visualization software (DAVIS).

2.7 VUV production

Frequency mixing is one of the most general & important phenomena in non-linear optics. For linear optics, polarization is linearly proportional to the electric field and non-linearity is the outcome of a higher order susceptibility. The induced polarization P can be expressed as an expansion in the power of the electric field E.

$$\mathrm{P}{=}\epsilon_0[\chi^1 + \chi^2.E + \chi^3.E^2 + ...]E \tag{2.24}$$

where χ^1 is the linear optical susceptibility, χ^2 is the second order nonlinear susceptibility and χ^3 is the third order nonlinear susceptibility. ϵ_0 is the

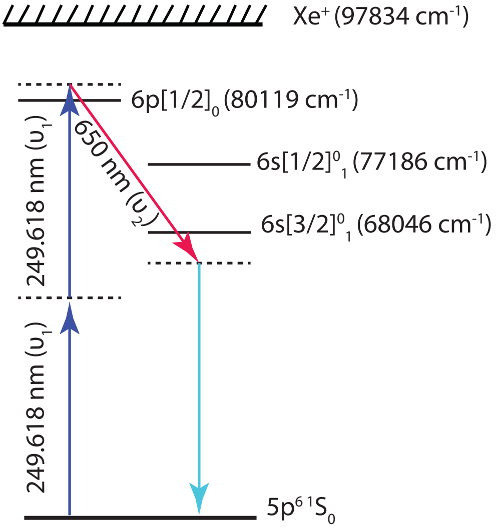

Figure 2.8: Energy level scheme of Xenon for the four-wave difference mixing process.

permittivity of free space. The third order nonlinear susceptibility χ^3 is responsible for the four wave difference-mixing process. In a non-linear process, two or more frequencies interact in a non-linear medium to produce a sum or difference frequencies(23). Tunable VUV was produced by the four-wave difference mixing technique for the experiments(122). Signals arise when three input fundamental photons from two lasers, one at frequency (ν_1), and the other at frequency (ν_2), are used to produce a fourth output photon at the difference frequency as shown in Figure 2.8. The fixed dye laser (Scanmate) output at 249.618 nm (ν_1) combined with a tunable radiation from an other dye laser (Fine adjustment) around 650 nm (ν_2) was used to produce a tunable VUV (ν_{vuv}) light around 155 nm i.e. $\nu_{vuv} = 2{*}\nu_1 - \nu_2$. The two wavelengths were focused in Xe gas (30 mbar) contained in a stainless steel cell, which served as a non-linear medium for VUV production as shown in Figure 2.9(59).

2.8 State preparation

For any crossed-molecular-beam experiment, initial state preparation is one of the important critical parameters for the quality of the experiment. Ideally the molecular-beam should be perfectly rotationally cooled i.e. the total population should be in the ground state. However, experimentally achieving this ideal state is challenging. With the development of state-of-art molecular-beam techniques, the gap between the real molecular-beam and ideal molecular-beam has been narrowed. The development of the Even-Lavie valve(42) by Even and co-workers, the cantilever-piezo valve(63) from the group of Janssen

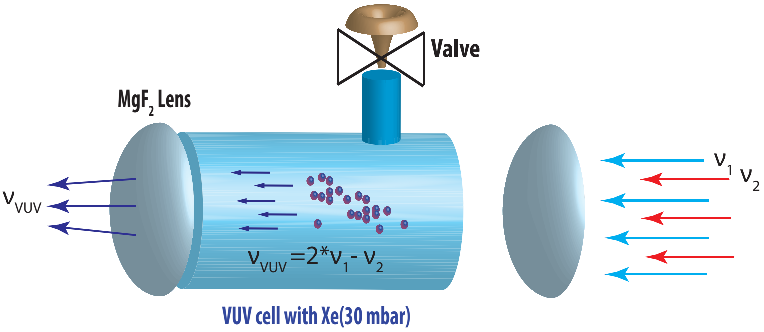

Figure 2.9: Schematic of a VUV cell with 30 mbar of Xe for the production of VUV.

and the very recently developed Nijmegen pulsed valve from our group has helped to produce rotationally cooled pulsed molecular beams. We have used the Nijmegen pulsed valve(137) and Jordan valve(50) for this experimental work. For polar molecules, the use of a Stark decelerator can slow down the molecular-beam and hence allow us to study scattering at a low energy.(123) The group of van de Meerakker successfully demonstrated quantum scattering resonances with application of Stark decelerator(70; 124).

2.8.1 O_2 molecular-beam

O_2 is a homonuclear open shell molecule with no dipole moment. With identical spin-zero nuclei, and its electronic ground state symmetry of $X^3\Sigma_g^-$, the quantum number N of molecular rotation in O_2 is restricted to odd values. For crossed-molecular inelastic scattering studies of O_2 with He, 5% O_2 in argon rotationally cooled molecular-beam was produced by supersonic expansion using a Jordan valve. State-selective detection of O_2 $X^3\Sigma_g^-$(v=0,NF) by (2+1) resonance enhanced multi-photon ionization (REMPI) around 225 nm via the $3dp^3\Sigma_{1g}^-(v = 2)$ Rydberg state was employed here(139). This transition is shown in Figure 2.10 which shows a selection of electronic states and Rydberg states of O_2. A simulated spectrum for this transition was first constructed using PGOPHER(133) and compared with the experimental spectrum for the initial beam (before scattering) in Figure 2.10. While the chosen transition is one of the strongest of the *3dp* Rydberg states, it does not allow a clean probe of the F_2 final states. From the simulated spectrum, REMPI line positions were determined for probing a range of final (NF) rotational states.

2.8.2 CO molecular-beam

CO is a heteronuclear closed shell molecule with a small dipole moment. An energy level diagram of CO is shown in Figure 2.13. For crossed-molecular beam inelastic scattering studies of CO with He/Ar, 2% CO seeded in argon

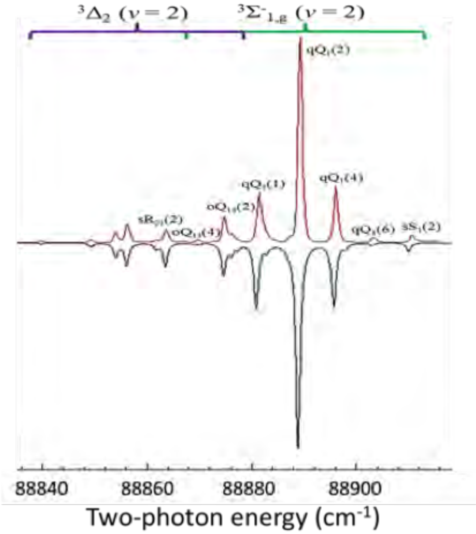

Figure 2.10: The panel shows the (2+1) REMPI spectrum of O_2. The red spectra in the panel show experimental data while the black spectra shows the simulated spectra from PGOPHER.

rotationally cooled molecular-beam was produced by supersonic expansion using the Nijmegen pulsed valve. A (2+1) and $(1 + 1^{'} + 1^{''})$ REMPI scheme was used for detection of CO(14; 60). Rotational populations of CO seeded in argon were obtained from (2+1) REMPI spectrum of $E^1\Pi \rightarrow X^1\Sigma^+$ transition of CO. The population of $j = 0$ was about 60% and $j = 1$ was about 35% corresponding to a rotational temperature of 3 K. For the experiment using $(1 + 1^{'})$ detection scheme of CO, the VUV light was resonant with CO $A^1\Pi \leftarrow X^1\Sigma^+$ (v=0) transition. The PGOPHER program was used to simulate and fit the $(1+1^{'}+1^{''})$ REMPI of CO, which shows also a rotational temperature of 3 K. In order to experimentally determine the exact frequency of the scattered higher state CO, the parent CO molecular-beam was scattered with Argon and was detected by VUV light under $(1+1^{'}+1^{''})$ REMPI scheme. Figure 2.12 shows the scattered signal of CO detected by VUV light.

2.9 Crossed molecular-beam experimental setup with 2+1 REMPI detection schemes

The data were collected in a crossed molecular-beam machine with a variable beam crossing angle, REMPI ionization of the scattered products and with velocity map imaging detection as shown in Figure 2.14. We used two skimmed supersonic beams, one of neat helium produced from a Nijmegen pulsed valve and the other of 2% CO seeded in argon produced from a second Nijmegen

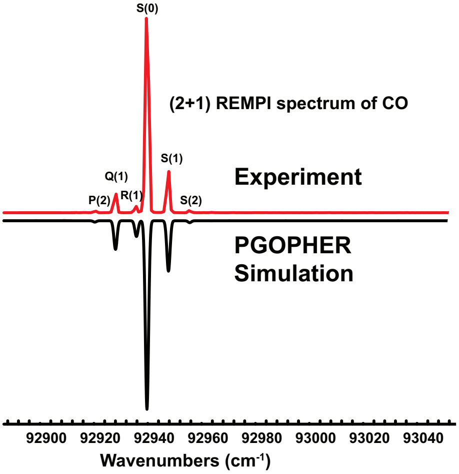

Figure 2.11: The panel shows the (2+1) REMPI spectrum of $E^1\Pi \leftarrow X^1\Sigma^+$ of CO. The red spectra in the panel shows experimental data while the black spectra shows the simulated spectra from PGOPHER.

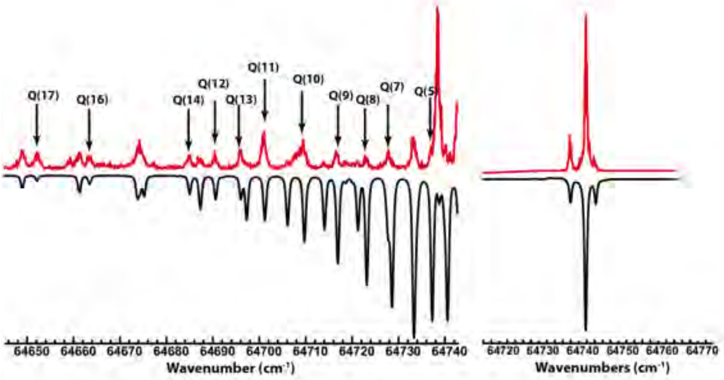

Figure 2.12: The panel shows $(1 + 1^{'} + 1^{''})$ REMPI spectrum of CO detected by VUV light. The left side of the panel shows VUV REMPI of scattered CO molecules with Ar in order to locate the exact line positions before the measurement. The right spectra in the panel shows the cold VUV REMPI. The red spectra in the panel shows the experimental data while the black spectra shows the simulated spectra from PGOPHER.

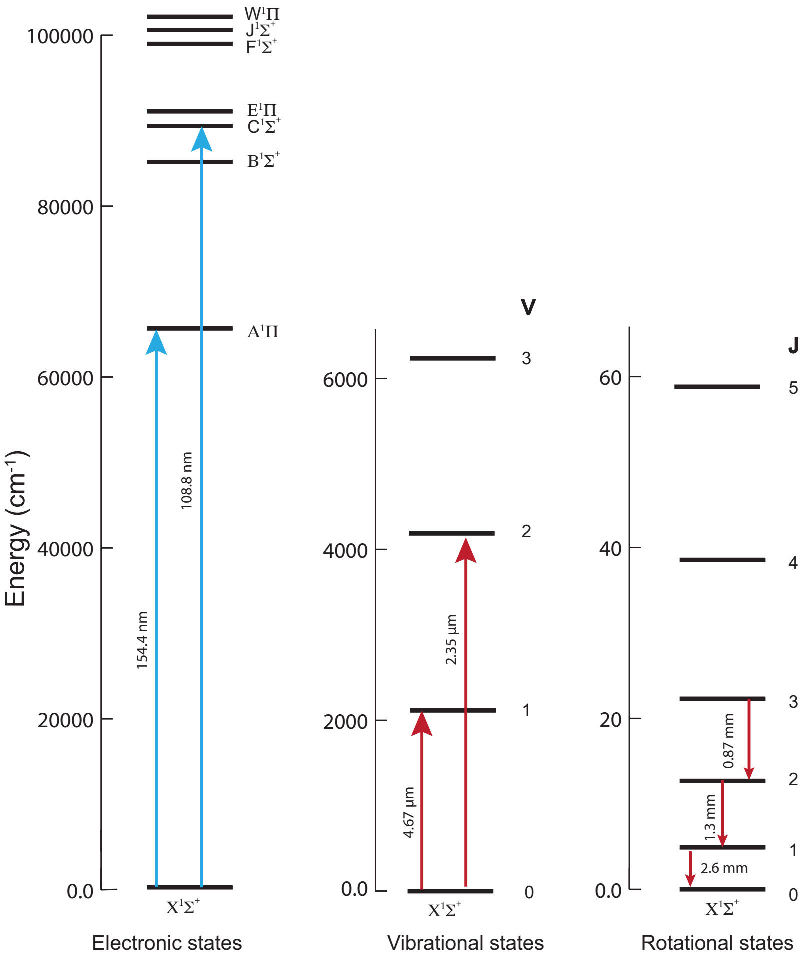

Figure 2.13: Schematic energy level diagram of CO showing its electronic, vibrational, and rotational states. CO ro-vibration transition near 4.7 μm and 2.35 μm are observed in interstellar medium. Infrared space observatories have detected a large number of CO ro-vibrational lines in Orion's peak 1 and 2(53).

pulsed valve. Backing pressure for the expansion was 3 bar for both colliding partners. The pulse duration of both valves at the crossing point was about 50 μs. The source chamber that houses the secondary beam (He) was differentially pumped and the molecular-beam passes through a skimmer with an aperture diameter of 2.5 mm positioned 3 cm away from the nozzle. The primary molecular-beam source was mounted in the differentially pumped rotatable chamber positioned 7 cm from the skimmer with an aperture diameter of 2.5 mm. Rotating the primary beam in the plane of the collision changes the angle between the two molecular-beams. Turbo molecular pumps pumped all the chambers. Two molecular-beams and the laser were coplanar parallel to the detector and were optimally aligned to ensure the best signal. For any crossed-molecular-beam experiment the initial state preparation is critical. Therefore, we analyzed the CO molecular-beam produced by the supersonic expansion of Argon. Figure 2.11 shows the REMPI spectrum transition from $E^1\Pi \rightarrow X^1\Sigma^+$ of CO. Population of ground state i.e. $j = 0$ was about 65%, $j = 1$ was about 33%, and a small fraction of higher states corresponding to a rotational temperature of 3.1 Kelvin. By comparing the PGOPHER simulated with the experimental spectrum, we can determine the REMPI line positions for higher rotational state, which is the prerequisite information for state-to-state inelastic scattering studies where we want to ionize the rotationally excited scattered products. The single collision condition must be ensured before recording the final data. Probing the depletion of CO ground state during collision, which is less than 5% ensured a single collision condition. The scattered product was ionized and was extracted by velocity map imaging ion optics lens. After 85 cm free flight along the time of flight tube, the 3-D ion sphere was crushed onto 2-D detector, which is read by CCD camera. Application of gating enables us to select our required mass and filter out the background ions of other mass. The S branch was chosen our data collection as it is well resolved and strong. The laser and both molecular-beams were operated at 10 Hz. The laser frequency was fixed during each image collection, rather than scanning the wavelengths over the full width of the Doppler profile of the REMPI transition (0.07 cm^{-1} for inelastic scattering of CO from He). However, the laser bandwidth was 0.1 cm^{-1} and the 2 mJ energy per pulse of the laser power broadened the transitions sufficiently that Doppler scanning was unnecessary. Scattered CO molecules were probed by 2+1 resonance enhanced multiple photon ionization on the $E^1\Pi \leftarrow X^1\Sigma^+$ transition using respective ultraviolet wavelengths around 215 nm. These wavelengths were generated by the frequency tripled output of a tunable pulsed dye laser (Fine Adjustment Dye laser) operating with DCM dye using a BBO crystal. The dye laser was pumped by a Nd:YAG laser (Continuum Surelite) operating at 532 nm and with 10 Hz repetition rate. Typical ultraviolet (UV) laser energies were 2 mJ per pulse with pulses duration of $7 - 9$ ns. The probe beam was focused with a 20 cm lens onto the intersection region of the molecular-beams.

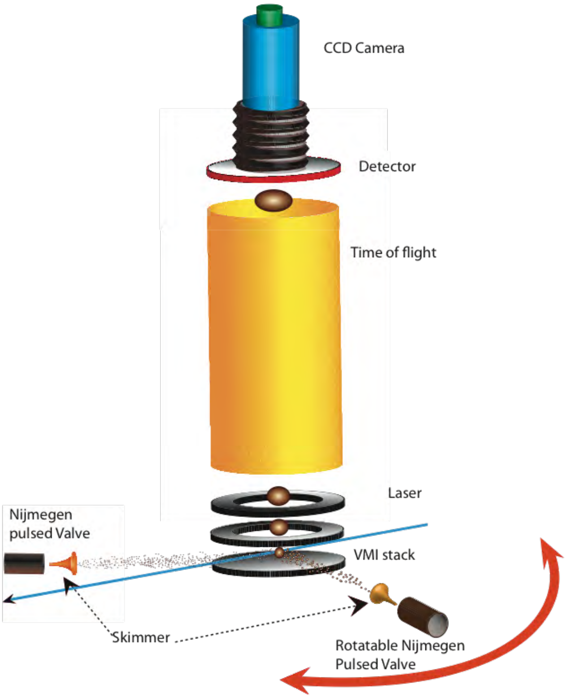

Figure 2.14: Schematic of the crossed-beam VMI setup showing two molecular-beams crossing at the center of the imaging ion optics. The angle between the two molecular-beams can be changed by rotating the primary beam around the center of ion optics in the plane of collision. The scattered product is detected by tunable dye laser system that is frequency tripled in a BBO crystal around 215 nm and focused at the center of ion optics by 20 cm lens. Laser polarization is in plane of the collision plane. The nascent CO^+ *image is mass selected by time of flight and projected onto a two dimensional (2D) imaging detector, then measured by a CCD camera.*

2.10 VUV detection of CO

To study alignment effects, we modified the rotatable crossed molecular-beam machine. A schematics of the experimental diagram is shown in Figure 2.15. The rotatable crossed molecular-beam machine was equipped with a VUV (vacuum ultra violet) REMPI ionization scheme to detect the scattered products with velocity map imaging detection. The condition was similar to that in the previous setup but now we used two skimmed supersonic beams, one of neat Argon produced from a Nijmegen pulsed valve and the other of 5% CO seeded in argon produced from a Jordan pulsed valve. Backing pressure for the expansion was 1 bar for both colliding partners. Two molecular-beams and VUV laser were coplanar and parallel to the detector and were optimally aligned to ensure the best signal. We have used four-wave mixing in Xenon to produce VUV light(59; 122). We fixed one dye laser (Scanmate) output at 249.618 nm (ν_1) combined with a tunable radiation from the other dye laser (Fine adjustment) around 650 nm (ν_2) to produce tunable VUV (ν_{vuv}) light around 155 nm using four-wave mixing i.e. $\nu_{vuv} = 2^*\nu_1 - \nu_2$. More detail about the resonance enhanced laser ionization scheme for CO via the $A^1\Pi$ state is described in the work of Sun et al(117; 96). The 355 and 532 nm output from the Nd:YAG laser (Continnum Powerlite 9010) were used to pump the two dye lasers, Scanmate and Fine adjutment respectively. The fundamental output from the fixed dye laser (Scanmate) using a Coumarin 307 dye was frequency doubled in a BBO crystal to produce the UV photon with an energy output of 5 mJ/pulse. The UV wavelength was tuned to one of the three 5p–6p two-photon resonance positions of Xe atoms. The other dye laser (Fine-adjustment) produced visible photons tunable in a region of 648-652 nm using DCM dyes. The two beams were combined with a 248 nm dichroic mirror transparent to visible light and both beams subsequently were focused into the Xe gas (30 mbar) contained in a stainless steel cell with a f = 100 mm plano-convex lens. A lens of focal length f = 1500 mm was placed 1000 mm away from the stainless steel cell to collimate only the visible light so that 249 nm and 650 nm focused at the same point inside the cell. In order to study alignment effects we used horizontal and vertical polarization of the VUV laser and photo-dissociation images from the OCS molecule ensured the polarization of VUV laser.(136) The Q branch was chosen for data collection, as it is well resolved and it shows strong alignment effect compared to the P and R branch. Application of gating enabled to select required mass and filter out any background ions of other masses. Scattered CO molecules were probed by a VUV laser on the $A^1\Pi \leftarrow X^1\Sigma^+$ transitions.

2.11 Data Analysis

2.11.1 Density-to-flux correction

The scattered products in the inelastic scattering collision experiment were detected using the REMPI technique. Scattered products were detected in the

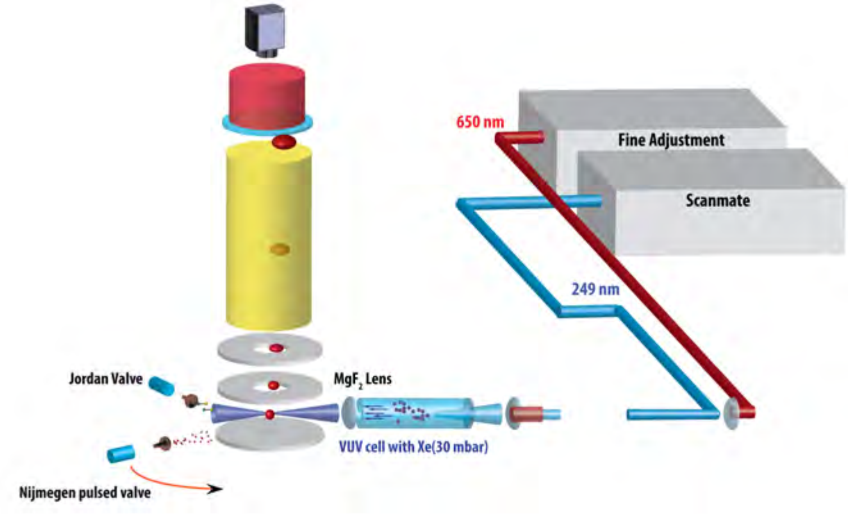

Figure 2.15: Schematic of the experimental cross molecular-beam VUV setup to study collision-induced alignment studies in inelastic scattering of CO with He and Ar. For the production of VUV light we fixed one dye laser (Scanmate) output at 249.618 nm (ν_1) *combined with tunable radiation from an other dye laser (Fine adjustment) around 650 nm* (ν_2) *to produce tunable VUV* (ν_{vuv}) *light around 155 nm using four-wave mixing technique i.e.* $\nu_{vuv} = 2^*\nu_1 - \nu_2$*.The UV wavelength was tuned to one of the three 5p–6p two-photon resonance positions of Xe atoms. The two beams were combined with a 248 nm dichroic mirror transparent to visible light and both beams subsequently focused into the Xe gas (30 mbar) contained in a stainless steel cell with a f = 100 mm plano-convex lens.*

laser focal volume but due to the geometry of the experiment, there was a detection bias in the experiment. Scattered molecules that are moving along the center of mass are faster than molecules leaving opposite to the center of mass. Slow molecules are detected with higher probability as compared with faster molecules. This leads to a detection bias which is reflected in the acquired experimental image. The angular distribution acquired from this experimental data does not purely reflect the differential cross section. The unwanted buildup of the density in the velocity map images should be corrected in order to extract actual angular distribution.
In order to correct this detection in bias angular distribution obtained from the velocity map images, density-to-flux correction technique or IMSIM developed by McBane was used.(84) IMSIM was used to extract corrected angular distribution from raw images. The two dimensional image obtained from velocity map imaging is the products of state to state total cross sections, angular distribution probability function and apparatus functions. Therefore, the time integrated intensity **I** on the image can be expressed as

$$I(v_x, v_y, v_z; j \rightarrow j^{'}, t)_{lab} = A\sigma(j \rightarrow j^{'})P(\theta, \phi)F_{app}(v_x, v_y, v_z; j \rightarrow j^{'}, t), \tag{2.25}$$

where v_x, v_y, are the velocity components in the collision plane and v_z lies parallel to time of flight axis. $\sigma(j \rightarrow j^{'})$ is state-to-state total cross section with its angular probability $P(\theta, \phi)$. 'A' is the amplitude factor depending on molecular-beam intensities. $F_{app}(j \rightarrow j^{'})$ is the apparatus function that primarily depends on experimental geometry, temporal and molecular distribution of the beam, and laser beams spatial and frequency distributions. The three dimensional Newton sphere formed from the ionized scattered products is projected to a two-dimensional detector. Therefore, the intensity of the ion signal on the detector can be expressed as a function of (x, y) or alternatively (r, θ).

$$I_{image}(r, \theta) = \sum_{v_z} I(v_x, v_y, v_z) \tag{2.26}$$

We can include σ and A in the equation above into the new apparatus function $F^{'}_{app}(j \rightarrow j^{'})$ as they serve only for intensity scaling to the DCS. Therefore, the above equation can be simplified as

$$I_{image}(r, \theta) \approx DCS_0(\theta, \phi)F^{'}_{app}, \tag{2.27}$$

where $F^{'}_{app}$ is the newly defined apparatus function, and the state-to-state differential cross sections can be extracted from the experimental image.

Using the apparatus function in the IMSIM program, an isotropic DCS in the center of mass can be simulated. Isotropic DCS means that the simulated image would have been isotropic if there would have been no detection bias of scattered products. In order to correct for the detection bias we divide the extracted angular distribution from experimental raw image by the simulated

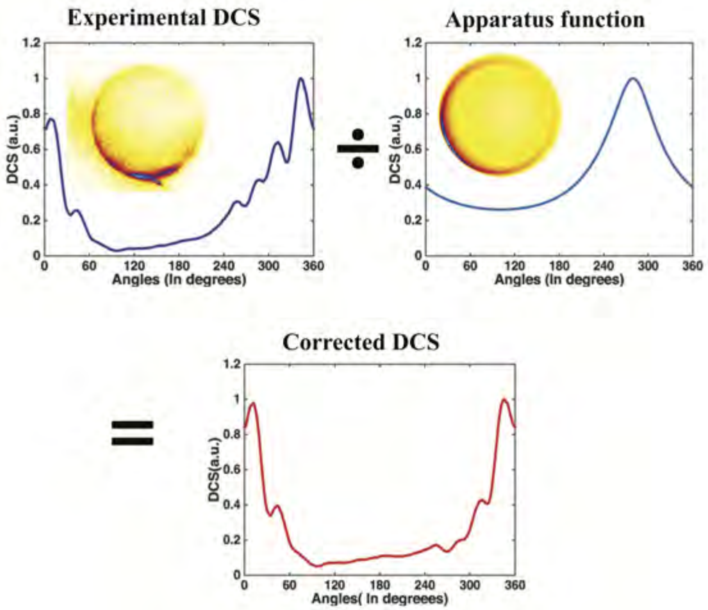

Figure 2.16: Direct extraction method of density-to-flux transformation. The angular distribution is extracted from the experimental raw image and divided by the angular distribution of simulated image. The outcome gives a corrected differential cross section by removing the effect of detection bias.

image using apparatus function. The outcome of the division negated the effect of detection bias and thus corrects the angular distribution of the scattered products. Thus, in order to obtain the correct differential cross-section it is absolutely necessary to do density-to-flux correction. Figure 2.16 shows an example of density-to-flux correction.

2.12 Discussion of possible experimental errors

The experimental data were repeated several times. There was no qualitative difference in the differential cross-sections. Therefore, the experimental data taken are reproducible. However there are certain factors, which can induce errors in the differential cross-sections

2.12.1 Under-estimation of higher $j^{'}$ states due to pre-dissociation for CO detection

Hines et al.(60) pointed out that failure to account for the C^+ channel when detecting CO^+ would undercount the higher rotational states. This decrease in sensitivity for higher states leads to undercounting effects in the integral cross-section measurements. However, undercounting would lead to a minor change in the rotational temperature. Thus, the true composition of the initial states remains ambiguous due to uncertainty in the rotational temperature. This ambiguity in the initial states could affect the differential cross-section. However if the distribution to be measured has only modest amount of rotational excitation, the error inducted by not accounting for the C^+ channel may be acceptable.

2.12.2 Post collision alignment

REMPI probe is very sensitive to the alignment of angular momentum vectors of the molecule(92; 100). Pullman et al, Alexander et al and Mayne et al have theoretically shown in their extensive work about the induction of alignment due to rotational inelastic scattering(5; 7; 83; 106). Collisional alignment followed by REMPI ionization of molecule aligned with respect to the laser polarization direction means that differential cross section is affected if the laser polarization is not favorable. Therefore, the alignment could lead to systematic undercounting, especially in higher $j^{'}$ states but does not change the peak position in differential cross-sections. For CO-Ar and CO-He system this problem is addressed using a robust polarization sensitive detection scheme i.e. VUV $(1 + 1^{'} + 1^{''})$ REMPI scheme. Angular measurement was done with different polarization that is often called polarization dependent differential cross section (PDDCS) and then it is summed up in order to negate systematic undercounting due to collision-induced alignment.

2.12.3 Error due to dislocation of laser focus

The direction of the laser propagation plays a key role. If the direction was almost perpendicular to the relative velocity vector, change of the laser focus position along the propagation direction would enhance the region of the image where molecules moving along the laser propagation directions appear. This will inflate the DCS in that region without changing the peak position of the DCS. Side-to-side displacements of the laser focus position can enhance the forward scattered part of the image with respect to the backscattered part or vice versa. Therefore, dislocation of the laser focus can affect the differential cross sections. In order to minimize the error due to dislocation of the laser focus we have ensured that the laser focus was at the center of the ion optics.

Chapter 3

Direct extraction of alignment moments

Abstract:[1]We present a novel means of analyzing velocity-map images of angular momentum polarization in inelastic scattering. In this approach, linear combinations of angular distributions obtained by integrating select regions of images obtained with two probe laser polarizations directly yield the alignment-free differential cross sections and the differential alignment moments. No fitting or basis functions are needed in the analysis. The method relies on the fact that the angular distribution for out-of-plane scattering is encoded in the distribution along the relative velocity vector, and this may be recovered quantitatively owing to the redundancy of the in-plane and out-of-plane scattering for the H case.

---

[1] Adapted from: Arthur G. Suits, **Chandan Kumar Bishwakarma**, Lei Song, Gerrit C. Groenenboom, Ad van der Avoird, and David H. Parker. *Direct extraction of alignment moments from inelastic scattering images.* The Journal of Physical Chemistry A, 119(23):5925-5931 1089-5639, 2014.

3.1 Introduction

Despite two decades of active investigation, imaging studies of inelastic scattering continue to offer surprising new insights into fundamental aspects of atomic and molecular interactions.(115; 8; 22; 128; 51; 65; 80) These studies allow stringent tests of the quality of electronic structure calculations and stimulate efforts to combine the intuition afforded by classical treatments with the rigors of a full quantum description. Among the more intriguing such examples in recent years has been the direct detection of angular momentum polarization in scattering.(87; 129; 26; 24; 31; 39; 43; 6) The power of imaging in these experiments is that it combines a spectroscopic probe (i.e., resonance-enhanced ionization) with angular distribution measurements yielding a molecular-frame description of the scattering event.(37; 41) The study of collision-induced angular momentum polarization is an example of 3-vector correlation: the initial relative velocity vector, the final relative velocity vector, and the angular momentum projection and their correlations are simultaneously measured.(56; 55; 24; 18; 86; 15) Meyer reported early investigations or rotational alignment in state-resolved scattering of NH_3 and NO(87; 68) which was followed by imaging studies by Chandler, Cline and coworkers on the argon-NO system (39; 129). Studies by Chandler and Cline and coworkers also showed that such collisions could give rise locally to rotational orientation, and the sense of this orientation and its angular distribution could be measured using circularly polarized probe lasers and this continues to be an active area of investigation.(80; 31) Very recently, Chandler and coworkers have studied scattering of electronically excited NO, even examining alignment in that system(114; 65), and Brouard and coworkers have revisited the issue of rotational alignment in the Argon-NO system and combined this with both full quantum calculations and with a quasi-quantum treatment.(43; 26; 25)

In essentially all of these inelastic scattering alignment studies, the analysis is performed by taking difference images obtained with probe polarization parallel to the detector (H) or perpendicular to the detector (V). These difference images are then fitted using various means to extract the alignment moments. For rotational alignment there are two such moments, $A_0^{(2)}$ and $A_{2+}^{(2)}$ (we will employ the Hertel-Stoll renormalized polarization-dependent differential cross sections(58; 100)) whose angular distributions are reported and related to classical treatments or to full time-independent quantum scattering calculations. Although these approaches to the analysis are clearly successful, we are naturally led to wonder if there might be a more direct way to extract these distributions from high quality scattering data rather than through fitting methods. With the remarkable resolution of velocity map imaging and the simple clarity of these images such an objective seems attainable. If we are successful, any structures in the distributions will appear automatically and we need not wonder if our analysis has overlooked some or artificially imposed others. In this paper we show just such a direct means of extracting the three key distributions: the differential cross sections (DCS) and the $A_0^{(2)}$ and $A_{2+}^{(2)}$ moments, simply through linear combinations of angular distributions obtained by integrating various regions of images obtained for H and V polarization. We will illustrate this using a single experimental image obtained for scattering of CO with argon at a collision energy of 700 cm^{-1}, and we compare our extracted distributions with quantum scattering calculations for this single rotational level. A full presentation of all the scattering results for the system and a detailed comparison to theory will be reported in a future publication.

3.2 Experimental Methods

The data were collected in a Rotatable crossed molecular-beam machine and VUV REMPI ionization of the scattered products with velocity map imaging detection.We have used four-wave mixing in Xenon to produce VUV light. The scattered product was ionized and was extracted by velocity map imaging ion optics lens.The detailed information about the experimental set up is shown in Chapter 4.

3.3 Results and Discussion

3.3.1 Overview

Our objective is to extract the DCS and the rank 2 alignment moments directly from inelastic scattering data. Our approach is to use Q-branch images for perpendicular probe transitions and consider horizontal (H) and vertical (V) polarization, where H refers to the probe polarization lying parallel to the plane of the image, and V, normal to that plane. The images that we will use for demonstration are given in Figure 3.1.

These were obtained via the Q(9) transition of CO via the A state as described in the Experimental section. The difference in the appearance of these two images is a direct manifestation of angular momentum polarization. In its absence, these images would be identical. The relevant coordinate frames we employ are shown in Figure 3.1. Our probe laser propagation direction is in the plane of the beams, perpendicular to the relative velocity vector. This defines the Laboratory Frame in which the Z-axis coincides with the CO beam direction in the center-of-mass, the X-axis is parallel to the laser propagation direction, and the Y-axis coincides with the time-of-flight axis. The alignment moments are obtained by analyzing the distributions in the Collision Frame, in which Z_{coll} again coincides with the the CO beam direction in the center of mass frame, but X_{coll} is now in the plane of the scattered CO, perpendicular to Z_{coll}. Y_{coll} is then perpendicular to Z_{coll} and X_{coll}. For CO scattering in the plane of the beams, the Laboratory and Collision Frames coincide. For scattering of CO out of the plane, the Collision Frame effectively represents a rotation of the Laboratory Frame about the Z axis.In the conventional approach, images are

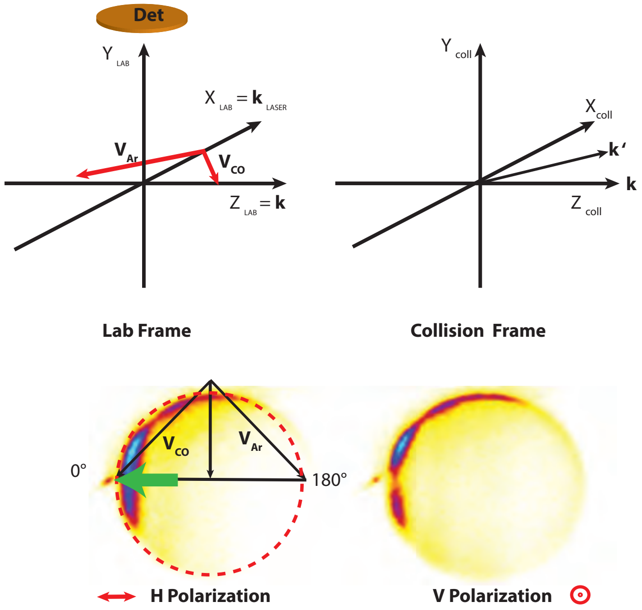

Figure 3.1: CO Q(9) images for CO-Ar scattering and indicated probe polarization. For the H image, the associated Newton diagram is shown.

recorded with H or V probe laser polarizations and the difference between these is fitted using various means to obtain the alignment moments. Our strategy instead relies on considering just three limiting distributions. We first describe intuitively how this works and how we do this analysis in practice, then we present the underlying mathematical justification.

The analysis is based upon the fact that the alignment-free differential cross section (DCS) and alignment moments may be obtained rigorously from the Collision Frame angular distributions for each of three orthogonal probe polarizations: One with probe laser polarization along Z_{coll}, parallel to the relative velocity vector, (termed H, in-plane or “HIP”), one with the probe laser polarization parallel to Y_{coll}: This is the in-plane scattering for V polarization (V,-in-plane, “VIP”). And finally from the scattering for probe polarization along X_{coll}. But for the in-plane scattering, X_{coll} also corresponds to the laser propagation direction, so that polarization geometry is not accessible. However, this geometry is equivalent to the Collision Frame which is rotated 90^o from the Laboratory Frame for Vertical polarization as illustrated in Figure 3.2. If we can obtain the angular distribution for the products scattered perpendicular to the plane of the beams (and the detector) for V polarization, we obtain the missing geometry needed to extract the parameters directly from the distributions. We have found that by analyzing a narrow rectangular stripe along the relative velocity vector and converting this to an angular distribution, we are able to obtain the distribution corresponding to the third

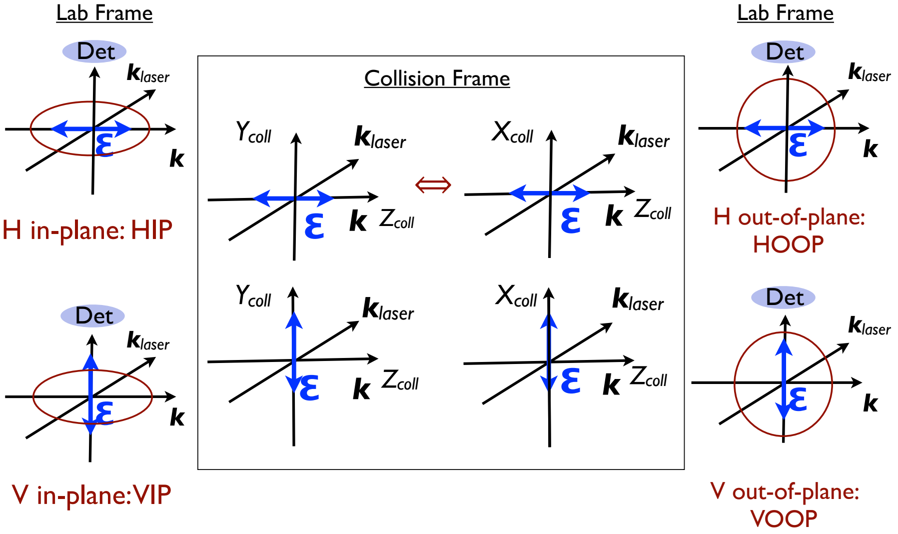

Figure 3.2: Relation of the lab frame and collision frame for the four angular distributions obtained from the images.

geometry, which we designate V, out-of-plane ("VOOP"). To obtain this distribution quantitatively, we first analyze and compare the equivalent image for H polarization ("HOOP"). In this case the two distributions HOOP and HIP should be identical. We typically adjust the limits of the region of integration (i.e., the box position) so that the features in the distributions are coincident. We then adjust the scaling so that the HOOP distribution has the same integral as the HIP distribution. An example of this analysis is shown in Figure 3.3. When we obtain the appropriate segment of the image that gives two nearly-identical angular distributions for H images, we employ the same rectangular image segment, integration and scaling for V images obtained under otherwise identical conditions. This yields three effective angular distributions: $I_H(\theta)$, $I_{VIP}(\theta)$ and $I_{VOOP}(\theta)$. The alignment-free differential cross sections and the polarization moments are then obtained simply as appropriate linear combinations of these three distributions. The sensitivity of the reported distributions to various aspects of the analysis is examined below. We note also that this strategy, which rests on the recognition that the angular distribution may be accurately obtained simply by integrating the region along the relative velocity vector, may find other uses, for example in photodissociation or reactive scattering particularly involving polarization studies.

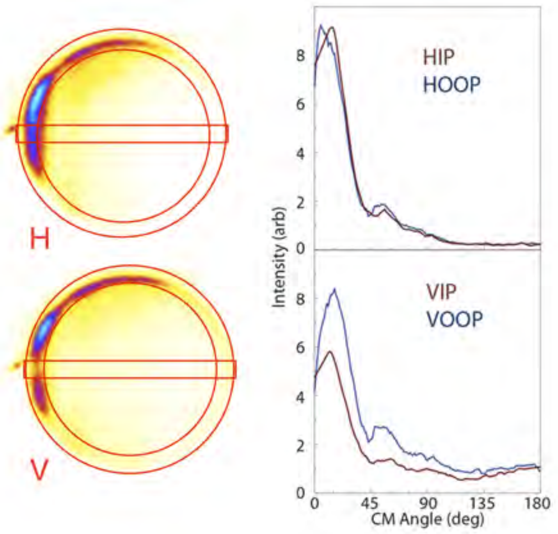

Figure 3.3: CO Q(9) images for indicate probe polarizations and the four distributions extracted from them. Although the overall intensity scale for the angular distributions is arbitrary, the two plots are on the same scale.

3.3.2 Mathematical foundation

To obtain the form of these distributions, we loosely follow the approach of Brouard(25), which in turn rests on a celebrated paper of Fano and Macek(44), although many have made contributions in this area. In addition to the alignment-free DCS, there are two angle-dependent parameters that embody the description of the alignment distribution for collisions of unpolarized beams: $A_0^{(2)}$ and $A_{2+}^{(2)}$. $A_0^{(2)}$ embodies the **v**-**J** correlation, with limiting values of -1, corresponding to **v**$\perp$ **J** and +2 corresponding to **v** $\parallel$ **J**.A$_{2+}^{(2)}$ reflects the extent to which the **J** vectors align parallel to to Y_{coll} ($A_{2+}^{(2)}$=-1) or X_{coll} ($A_{2+}^{(2)}$=+1).(58; 100) We write the signal appearing in a given angular range in the image as a product of the DCS and the detection probability:

$$I(\theta) = \frac{d\sigma}{d\theta}(\theta)P(\theta;\chi,\Theta,\phi) \tag{3.1}$$

The polarization-dependent transition probability $P(\theta;\chi,\Theta,\phi)$ depends both on the angular momentum polarization and the probe sensitivity to that polarization(25):

$$P(\theta;\chi,\Theta,\phi) = C\left[1 + \sum_{kq} A_q^{(k)}(\theta)F_q^{(k)}(\chi,\Theta,\phi)\right] \tag{3.2}$$

In this expression C is a constant and the $F_{q\pm}^{(k)}(\chi, \Theta, \phi)$ functions are geometric factors that embody the probe sensitivity as determined by the angles (χ, Θ, ϕ) characterizing the linear probe laser polarization: Θ and ϕ are the polar and azimuthal angles of $\mathbf{k}_{laser}$ in the Collision Frame, and χ is the third Euler angle needed to specify the laser polarization direction in that frame. These functions take the general form(25)

$$\begin{aligned}
F_0^{(2)}(\chi, \Theta, \phi) &= \frac{1}{4} h^{(2)}(j_i, j_f)(3\sin^2\Theta\cos 2\chi - [3\cos^2\Theta - 1]) \qquad (3.3)\\
F_{1+}^{(2)}(\chi, \Theta, \phi) &= \frac{\sqrt{3}}{4} h^{(2)}(j_i, j_f) c_2(j_i)(2\sin\Theta\cos\phi\sin 2\chi + \\
&\quad 2\sin\Theta\cos\Theta\sin\phi\cos 2\chi - \sin 2\Theta\cos\phi)\\
F_{2+}^{(2)}(\chi, \Theta, \phi) &= \frac{\sqrt{3}}{4} h^{(2)}(j_i, j_f) c_2(j_i)([1 + \cos^2\Theta]\cos 2\phi\cos 2\chi - \\
&\quad 2\cos\Theta\sin 2\phi\sin 2\chi - \sin^2\Theta\cos 2\phi)
\end{aligned}$$

They are functions of the laser polarization direction and the line strength factor $h^{(2)}$, which for Q-branch transitions is always unity.(44) We will confine our treatment to scattering directly in the detector plane or perpendicular to it. We then have only two polarization geometries for each of these two collision frame distributions, characterized by particular values of (χ, Θ, ϕ) and given in Table I. Substituting these values into eq. 3.2 we obtain the following expressions for the angular distributions in the different probe geometries:

$$I_H(\theta) = \frac{d\sigma}{d\theta}(\theta) C[1 + A_0^{(2)}(\theta)] \qquad (3.4)$$

$$I_{VIP}(\theta) = \frac{d\sigma}{d\theta}(\theta) C[1 - \frac{1}{2} A_0^{(2)}(\theta) - \frac{\sqrt{3}}{2} A_{2+}^{(2)}(\theta)] \qquad (3.5)$$

$$I_{VOOP}(\theta) = \frac{d\sigma}{d\theta}(\theta) C[1 - \frac{1}{2} A_0^{(2)}(\theta) + \frac{\sqrt{3}}{2} A_{2+}^{(2)}(\theta)] \qquad (3.6)$$

We give only one H result as HIP and HOOP are identical. Table I and these equations show a number of key features of the polarization sensitivity. First, it is seen that the scattering signal for the H polarization has no sensitivity to the $A_{2+}^{(2)}$ parameter. This is expected given the cylindrical symmetry of this geometry. Furthermore, if we compare V and H in-plane, for example by taking a difference image as is commonly done, we can eliminate the population contribution but we cannot disentangle the $A_0^{(2)}$ and $A_{2+}^{(2)}$ contributions. However, by averaging these three angular distributions together we obtain a distribution directly proportional to the DCS, free of any polarization modulation. We can then use this to normalize the other distributions to isolate the alignment moments. By taking the difference of the VOOP and VIP distributions we obtain a signal that is directly proportional to the $A_{2+}^{(2)}$ parameter (with the same proportionality as the DCS). Finally, the

Table 3.1: Geometric factors for indicated distributions.

	HIP	HOOP	VIP	VOOP
(χ, Θ, ϕ)	$(\pi, \frac{\pi}{2}, 0)$	$(\pi, \frac{\pi}{2}, \frac{\pi}{2})$	$(\frac{\pi}{2}, \frac{\pi}{2}, 0)$	$(\frac{\pi}{2}, \frac{\pi}{2}, \frac{\pi}{2})$
$F_0^{(2)}$	1	1	$-\frac{1}{2}$	$-\frac{1}{2}$
$F_{2+}^{(2)}$	0	0	$-\frac{\sqrt{3}}{2}$	$\frac{\sqrt{3}}{2}$

$A_0^{(2)}$ moment is obtained simply from the H distribution and the alignment-free DCS.The relevant expressions needed are

$$\frac{d\sigma}{d\theta}(\theta) = \frac{1}{3}[I_H(\theta) + I_{VIP}(\theta) + I_{VOOP}(\theta)] \tag{3.7}$$

$$A_{2+}^{(2)}(\theta) = \frac{\sqrt{3}[I_{VOOP}(\theta) - I_{VIP}(\theta)]}{I_H(\theta) + I_{VIP}(\theta) + I_{VOOP}(\theta)} \tag{3.8}$$

$$A_0^{(2)}(\theta) = \frac{3\, I_H(\theta) - [I_H(\theta) + I_{VIP}(\theta) + I_{VOOP}(\theta)]}{I_H(\theta) + I_{VIP}(\theta) + I_{VOOP}(\theta)} \tag{3.9}$$

The results of this analysis for the images in Figure 3.1 are shown in Figure 3.4 and compared to theory. The overall trends are reproduced quite well but one should take note of the different scales. A number of qualitative features are seen in the theory and reproduced in the experimental analysis, and the details of this will be discussed in a future publication. However, we make a few observations here. The $A_0^{(2)}$ moment rises from a highly negative value in the backward direction to a positive value in the forward direction, as is widely seen and rationalized in the kinematic apse (KA) picture. In this view the collision is sudden and the angular momentum change is perpendicular to the direction of linear momentum transfer. The result is that for the directly backscattered product, the angular momentum has no projection on the recoil direction ($A_0^{(2)}$ = -1, $\mathbf{J} \perp \mathbf{v}$), while in the forward direction there is a tendency to positive alignment, $\mathbf{J} \parallel \mathbf{v}$. For the pure forward scattering the projection of **J** onto the recoil direction must vanish by symmetry, but as is usually the case, this sharp transition is not detected experimentally. The other notable feature is that the overall magnitude of the $A_0^{(2)}$ moment is consistently lower in experiment than in the theory in the backward direction. This is seen almost universally, and remains a rather puzzling aspect of these studies. The $A_{2+}^{(2)}$ moment shows interesting structure in the theory that is clearly captured in the experiment. Its magnitude increases from a maximum at 45^o to zero for the most forward scattered product. This sharp decrease in $A_{2+}^{(2)}$, along with the rise in the $A_0^{(2)}$ moment in the same region, combine (owing to opposite signs) to give rise to the gap in the forward scattering for the V image (and to the forward notch in the difference images commonly shown).

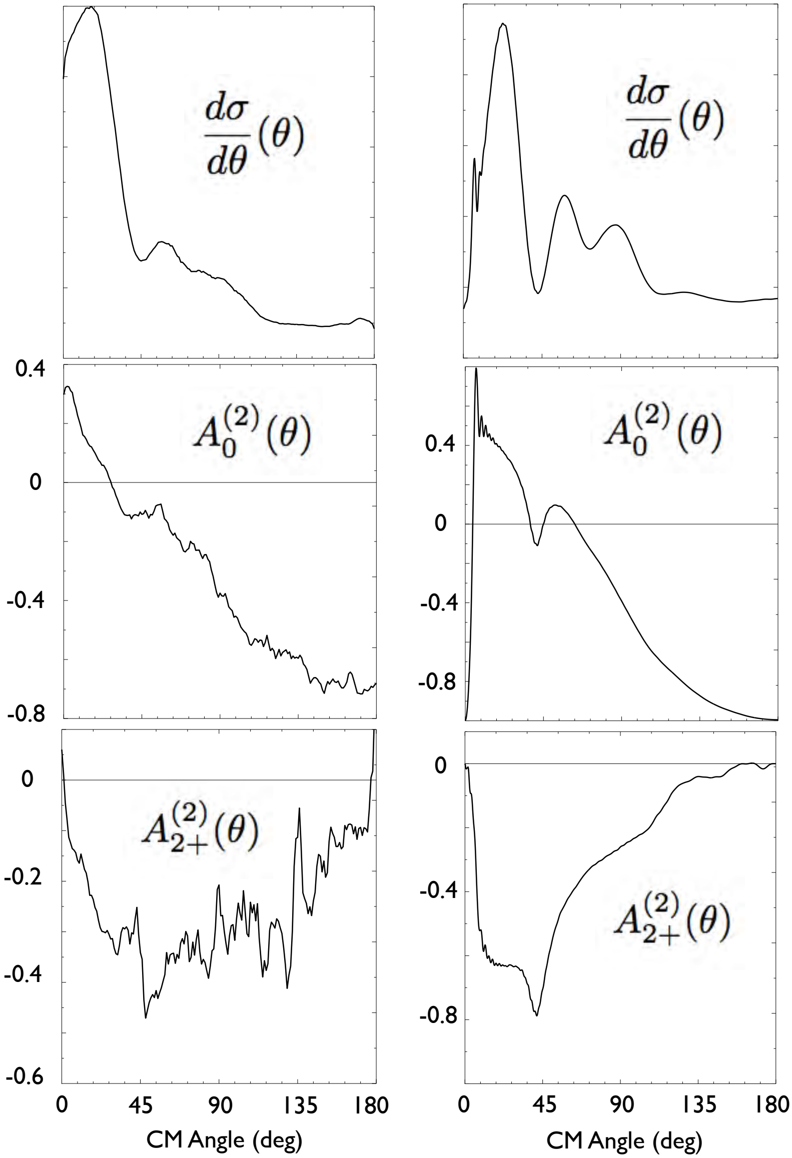

Figure 3.4: DCS and alignment moments obtained from the analysis (left) and from theory (right).

3.3.3 Sensitivity

We also examined the sensitivity of the inferred moments and the DCS to various aspects of the analysis. One point we note is that to obtain accurate DCSs that exhibit some of the structure in the theoretical results, we must include the slow (in the lab frame) portion of the angular distribution. However, when we the strategy to generate the alignment moments, substantial deviations from expected values are obtained and it is difficult to obtain HIP and HOOP distributions that agree. It may be that these images are partly "sliced" so that the out of plane scattering is undercounted. Or there may be some nonlinearities in the detection that are equalized for the HOOP and the HIP obtained from the fast (in the lab frame) side of the scattering image. We plan future experiments to probe these questions.

The general sensitivity analysis results are compiled in Figure 3.5 In each case we simply superimpose the results for a range of different parameter sets to convey the range of the distributions obtained. Figure 3.5A shows the consequence of changing the width of the rectangular "box" used for the VOOP integration from 8 to 30 pixels. It is clear that the distributions are quite insensitive to this value. Similarly, Figure 3.5B shows the results for changing the width of the ring integrated to give the VIP and HIP distributions over a range of 5 to 23 pixels. There is some slight variation in the DCS and the q=0 moment, and greater associated variation in the q=2 moment. Figure 3.5C shows the result of changing the origin of the box by up to four pixels. At this point the HIP and HOOP distributions become noticeably dissimilar, yet only the forward scattered edge of the q=2 moment shows any significant sensitivity to this. Figure 3.5D shows the result of reducing the V image intensity by 5 and 10%. There is surprisingly little variation in any of the extracted distributions in this case, which is heartening given that it is always difficult to ensure that the the intensities are well controlled as the polarization is changed. The last panel, Figure 3.5E, shows the result of translating the V image by 2 and 3 pixels in X and Y. This has a large effect on the $A_{2+}^{(2)}$ moment and a significant effect on the $A_0^{(2)}$ moment but again little impact on the inferred DCS. This would only occur if the image focusing conditions or camera moved in the course of changing the polarization. In all, the results presented in Figure 3.5 show that this approach is remarkably robust.

3.4 Conclusion

We have outlined a simple approach to extract alignment moments and the alignment-free DCS directly from state-resolved images of inelastic scattering. The approach is demonstrated in application to velocity-mapped images of CO scattering off argon into $j^{'}$=9, probed via A state. The results are compared to theoretical calculations of these moments, and good agreement is seen in many features of the distributions, although the magnitude of the alignment for the most backscattered product is underestimated as is generally found to be the

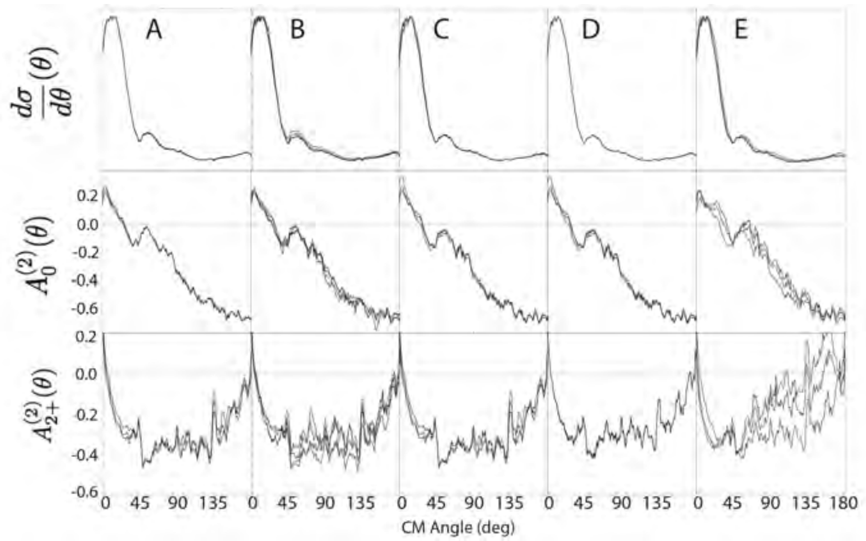

Figure 3.5: Results of sensitivity analysis. Variations in box width (A), ring width (B), box origin (C), relative image intensity (D) and relative image position (E) were examined (see text).

case experimentally. The approach may have other potential applications to photodissociation and reactive scattering.

Chapter 4

Imaging collision-induced alignment effects for inelastic scattering of CO with Argon

Abstract: The collision-induced alignment arising from the inelastic scattering of Carbon Monoxide (CO) with Argon at a collision energy of 700 cm^{-1} was studied by measuring polarization-dependent state-to-state differential scattering cross sections for rotationally excited CO molecules using a crossed molecular beam apparatus and velocity map imaging. A $(1 + 1^{'} + 1^{''})$ VUV (Vacuum Ultra-Violet) REMPI (Resonance Enhanced Multi Photon Ionization) scheme was used and images were obtained by setting the VUV light polarization direction parallel or perpendicular to the scattering plane. Large differences between the images for the two polarizations were observed. A direct analysis procedure as described in Chapter 3 of this thesis(116) was used to extract the DCS (differential cross sections) and the X and Y alignment moment for each final rotational state. These were then compared with the well-established theory. Good agreement between theory and experimental results showed the reliability of this experiment.

4.1 Introduction

Rotational excitation of atoms and molecules has been studied in great detail(32). There are ample experimental investigations that have measured the state-to-state vibrational and rotational energy transfer, but experimental investigations on the collision-induced angular momentum polarization that should arise in such scattering processes are less common. Detection of collision-induced angular momentum polarization in a crossed beam scattering experiment provides a stringent test for quantum scattering calculations. Collision-induced alignment has been studied for NO scattering with Ar but there have been fewer studies on polarization effect studies on CO with Argon. The group of Meyer reported an early investigation of collision-induced rotational alignment for the NH_3 molecule(87). Velocity Map Imaging(41) allows a more detailed measurement of polarization dependent differential cross sections (PDDCS) in inelastic scattering studies. The group of Chandler and Cline has used the $(1 + 1^{'})$ REMPI ionization scheme and velocity map imaging to study collision-induced alignment of NO with Argon(39; 130) and even determined the angle dependent orientation of circular polarization in the collision plane.(29; 28) collision-induced orientation and alignment effects in the scattering of NO final rotational angular momentum as a function of the final scattering angle has been reported by the group of Brouard, using the hexapole state selection(25; 31; 26). We compare our results with their reports of NO collisions with Ar at 533 cm^{-1} collision energy. This chapter describes the experimental study of collision-induced angular momentum polarization for inelastic scattering of CO with Ar at a collision energy of 700 cm^{-1}. A closed-shell molecule such as CO is attractive for probing alignment effects compared to the open-shell NO molecule, which shows alignment depolarization due to a slow angular momentum coupling with electron spin. However, detection of CO using velocity map imaging is much more challenging compared to NO because the excited electronic states that can be used as resonance step in the ionization detection process for CO lie deep in the vacuum ultraviolet (VUV). Here we employ a very simple three-color VUV REMPI detection scheme where all three colors are from VUV difference frequency mixing process and the VUV is not separated from the two laser beams needed for its generation. Ref(117) characterized this VUV detection method as a $(1 + 1^{'} + 1^{''})$ REMPI process which can be combined with velocity map imaging to measure polarization dependent differential cross sections (PDDCS). Chapter 5 of this thesis report CO-He scattering PDDCSs using this VUV scheme measured DCSs using polarization insensitive (2+1) REMPI of CO via the B-state(112). Chapter 3 of this thesis(116) established a simple analysis scheme for extracting polarization moment or collision-induced alignment directly from the polarization sensitive images measured from velocity map imaging. In contrast, the Brouard group uses (with success) a basis set expansion approach which reproduces the experimental images in order to obtain the alignment parameters. We tested our direct analysis method for collisions with Ar producing CO (j'=8) and showed good agreement of advanced ab-initio theory with the experimental result for polarization dependent differential cross-sections. In these experiments, 3-D Newton spheres for scattered CO molecules were crushed onto a 2-D detector to form a 2-D ring. The variation of scattering signal around the ring from vertical compared to horizontal polarization of the detection laser provides the polarization independent differential cross section (DCS) and the two moments $A_0^{(2)}(\theta)$ and $A_2^{(2)}(\theta)$ describing the angular momentum distribution. In contrast to our study of CO-He scattering in Chapter 5, the experimental geometry used for CO-Ar scattering is not sensitive to the $A_{1+}^{(2)}(\theta)$ moment. This Chapter shows the full range of accessible CO j' final states from CO-Ar scattering that the direct analysis yields DCS, $A_0^{(2)}(\theta)$ and $A_2^{(2)}(\theta)$ parameters that agree well with predictions of the advanced ab initio theory.

4.2 Experimental method

Figure 4.1 represents an overall picture of the experimental setup. The data were collected in a rotatable crossed molecular-beam machine and the VUV REMPI ionization of the scattered products with velocity map imaging. Two skimmed supersonic beams were crossed, one of neat pure argon produced from a Nijmegen pulsed valve(137) and the other was a 5% CO beam seeded in Ar, produced from Jordan pulsed valve. The backing pressure for the expansion was 1 bar for both colliding partners. The pulse duration of Nijmegen pulsed valve is about 50 μs and pulse duration of the Jordan valve is about 60 μs. The source chamber that houses the primary beam (CO) was differentially pumped and the molecular-beam through a skimmer with an aperture diameter of 2.5 mm positioned 7 cm away from the nozzle. The secondary (Ar) source was mounted in the differentially pumped rotatable chamber positioned 3 cm from the skimmer with an aperture diameter of 2.5 mm. The three chambers were pumped with separate turbo molecular pumps. The two molecular-beams and VUV laser beam were coplanar and were optimally aligned to ensure the best signal condition. The collision energy, 700 ± 50 cm^{-1}, was determined from the velocity mapped beam spot positions and spread of CO in Ar. For the secondary beam a small amount of CO was seeded in the Ar beam. This value for the collision energy was confirmed by the variation in size of the scattering image as a function of the rotationally excited CO internal energy after scattering. VUV light was produced by difference frequency mixing of two dye laser beams in xenon gas. We fixed one dye laser (Scanmate) output at 249.618 nm (ν_1) combined with tunable radiation from the other dye laser (Fine- Adjustment) at around 650 nm (ν_2) to produce tunable ν_{vuv} light around 155 nm where $\nu_{vuv} = 2^{*}\nu_1 - \nu_2$. The fundamental output from the fixed dye laser operating with Coumarin 307 dye was frequency doubled in a BBO crystal to produce the UV photon (ν_1) with an energy output of 5 mJ/Pulse. The UV wavelength was tuned to a 5p-6p two-photons resonance of Xe. The other dye laser (Fine-Adjustment) produced visible photon tunable in a region between 648-652 nm. The two beams were combined at a 248 nm dichroic mirror and

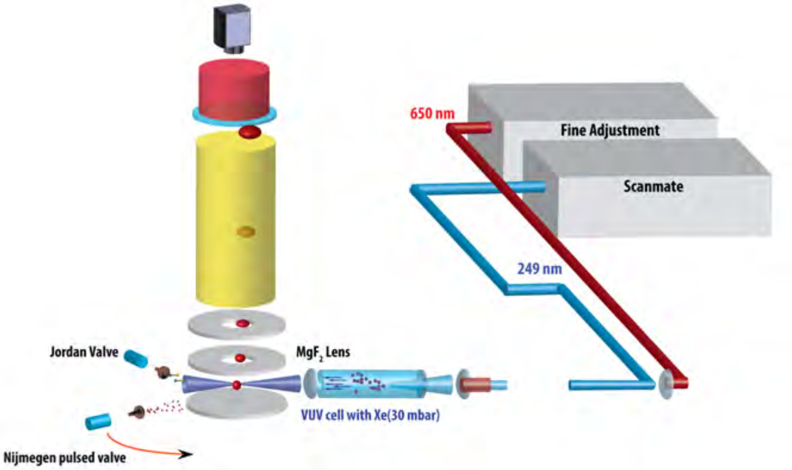

Figure 4.1: Schematic of crossed-beam VMI experimental setup for $(1 + 1^{'} + 1^{''})$ *VUV REMPI detection for aligned CO scattered from Argon. Two perpendicular skimmed supersonic molecular-beams were used, one of neat pure Argon produced from a Nijmegen pulsed valve and an other 5% CO seeded in Argon produced from the Jordan pulsed valve. The backing pressure for the expansion was 1 bar for both colliding partners. The scattered product is excited by VUV radiation resonant with CO X* $\rightarrow$ *A transition. VUV radiation was generated from four-wave mixing in Xe cell using 249 nm and 650 nm radiation from two tunable dye laser systems. Rotating 650 nm radiation changed the VUV laser polarization, which was verified with the OCS photo-dissociation image.*

subsequently focused in Xe gas contained in a stainless steel cell with a f =100 mm Plano convex lens. A pressure of 30 mbar Xe resulted in optimum VUV production. A lens of focal length f =1500 mm is placed 1000 mm away from the Xe cell to collimate only the visible light so that 249 nm and 650 nm will focus at the same point inside the cell. collision-induced alignment was probed using horizontal and vertical polarization of VUV light, which was prepared by rotating the polarization of the 650 nm laser beam. The purity and direction of the polarization of the VUV light in the detection zone was confirmed by photodissociation images of OCS.

The VUV light is resonant with the CO $A^1\Pi \leftarrow X^1\Sigma^+$ (v=0) transition. Our previous study(117) showed that the next step is near-resonant excitation from the A-state by the UV light (ν_1) to the $E^1\Pi$(v=6) state, followed by ionization by the 650 nm (ν_2) laser beam. Accidental resonance in the second step (ν_1)

leads to enhancement of transitions involving the $j' = 11$ state, which is not probed in this study.

Scattering images on $Q(j')$ branch were obtained with horizontal polarization (VUV laser polarization direction in scattering plane) and vertical polarization (VUV laser direction is perpendicular to the scattering plane) of VUV laser light. Two sets of angular distributions were extracted from vertical polarization and horizontal polarization images by integrating over outside annulus and over a stripe through the middle of the image along the relative velocity vector. In total four sets of angular distributions were obtained for one rotational excited state. For vertical polarization image, VOOP (vertical out of plane) and VIP (vertical in plane) were obtained and similarly for horizontal polarization, HOOP (horizontal out of plane) and HIP (horizontal in plane) was obtained. The initial state distribution of CO beam was optimized from the VUV $(1 + 1^{'} + 1^{''})$ REMPI spectrum of the parent molecular beam signal using the PGOPHER simulation program. Less than 5% out-scattering from the initial state was observed when the Ar beam is present. Figure 4.2 shows a portion of the VUV $(1 + 1^{'} + 1^{''})$ REMPI spectrum taken for CO after scattering with Ar. We chose the strong Q-branch transitions free of overlap with P-branches. Q(13) was not probed, for example, due to overlap with P(8). In the case of Q(7), the laser was set at the blue shoulder of the transition to avoid overlap with P(7).

4.3 Result & Discussion

The overview of methodology and the mathematical formulation for extracting PDDCS and the alignment parameters from the experimental images are extensively described in Chapter 3 of this thesis. Vector correlations between atom and molecule velocities in the collision reveal valuable information about the scattering process. The relationship between initial velocity vector k and final velocity vector $k^{'}$ provides an information about conventional DCS, where-as the triple correlation between initial velocity vector k, final velocity vector $k^{'}$ and $j^{'}$ gives an idea of the angular momentum polarization. Brouard et al calculated the relationship between polarization moments and alignment parameter(26). The alignment results in this chapter are presented in Hertel-Stoll renormalized polarization parameters $A^{k}_{q}(\theta)$. The $A^{(0)}_{0}(\theta)$ represents the conventional DCS while $A^{(2)}_{0}(\theta)$ and $A^{(2+)}_{0}(\theta)$ represent PDDCS, which is basically the triple correlation between initial velocity vector k, final velocity vector $k^{'}$ and $j^{'}$.

Due to the spread in collision energy, theoretical calculations were performed and their sum weighted for three different energies, 650 (25%), 700 (50%) and 750 (25%) cm^{-1}. Raw images for both vertical (V) and horizontal (H) polarization were measured from $j^{'}$=5-14 final states, where 'H' refers to the probe polarization lying parallel to the plane of the image and 'V' being normal to the plane. The images were first transformed for the density-to-flux correction using the IMSIM program of McBane and differential cross sections

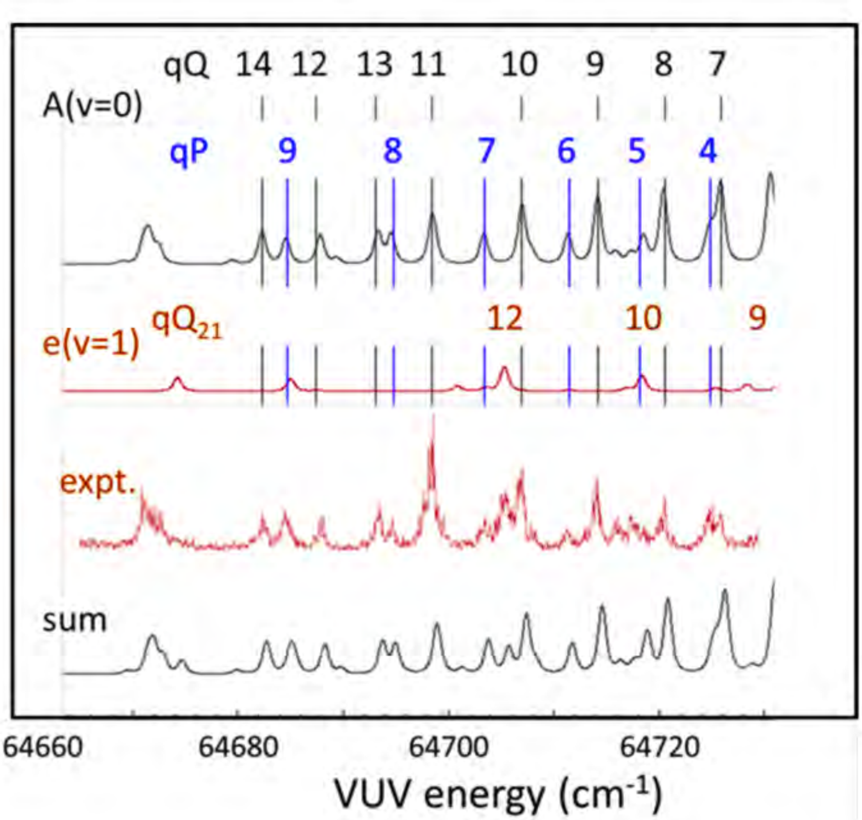

Figure 4.2: Simulated (pGopher) CO $A^1\Pi \leftarrow X^1\Sigma^+$ (v=0) VUV spectrum and experimental spectrum obtained while scattering with Ar. The position of the Q(j′) and P(j′) branches for the A(v=0) state simulation are labeled in the top row. The second trace shows a simulation of the perturbing e(v=1) state and the sum of both simulations is shown in the lowest trace. Above the sum spectrum is the experimental out-scattering spectrum. The lower two spectra compare favorably and show the enhancement of the Q(11) transition along with partial overlap of Q(10) with $Q_{21}(12)$ of the e-state. A temperature of 300 K was used in the simulation only to make most of the peaks visible, a non-Boltzmann final j′ state distribution for the experiment is expected.

were obtained by integrating along the outer edge of the flux-corrected image. On the right side of Figure 4.3 the experimental raw images obtained from H and V polarization are presented. Angular distributions are shown on the left side of Figure 4.3 with black and red lines in the graph showing in-plane and out-of-plane data, respectively, as extracted from the H experimental image. Green and blue lines show in-plane and out-of-plane data respectively, obtained from the V experimental image. As stated above, the HIP and HOOP curves should be identical; and indeed, the black and red lines overlap each other well. A more striking difference in green and blue lines in the graph is observed. As Δj increases, this difference increases which indicates a larger degree of alignment in higher final rotational states. The reliability of the extracted data is affected by numerous factors, especially the overlap of other transitions in the selected Q(j') REMPI transition. For example, Q(10) is partially overlapped by $Q_{21}(12)$ of the e-state as shown in Figure 4.2. In this analysis we have also assumed that the laser propagation direction is perpendicular to the relative velocity vector; deviation from this, especially due to the rather large beam spreads used in the apparatus, will impact the observed alignment effects. The high probability of elastic scattering, especially in forward scattered region, and other secondary collision effects can also affect the estimation of collision-induced alignment due to the inelastic scattering. Careful inspection of the V and H experimental images reveals clear distinctions in the forward scattered region and the V experimental image shows more sideways and back scattered signals, which are also evident from the PDDCSs extracted from the V and H images. The blue and green curves are higher as compared with black and red curves at higher scattering angles θ in Figure 4.3. These facts suggest that collision-induced alignment effect is stronger for the higher j' states, which is also rationalized in the kinematic apse picture from Brouard et al. Brouard et al have shown that rotational alignment effect in rotationally inelastic scattering of NO with Ar (and in general) originates primarily from the hard shell nature of the interaction potential. Collisions producing higher j' states are increasingly sensitive to the shorter intermolecular distances and thus the hard shell. For the CO-Ar system, collisional depolarization due to elastic or possibly multiple scattering effects appears to mainly affect the forward scattering regions. In contrast, the backward scattering region shows the maximum possible amount of collision-induced alignment effects, which is visually evident in Figure 4.3.

The resulting polarization-dependent differential cross section distributions derived from analysis of the HIP, HOOP, VIP, and VOOP curves are shown in Figure 4.4. The left panel in the Figure 4.4 shows the conventional DCS extracted from the experimental H and V images. In order to visualize both, the cross section and angular distribution the DCS is weighted by $sin\theta$. The red lines presents the theoretical calculations whereas the blue lines show the experimental data obtained from the experimental images. Regardless of the probe polarization, there is a clear trend in the nature of scattering. For lower to higher rotational states, scattering tends to move from forward to backward

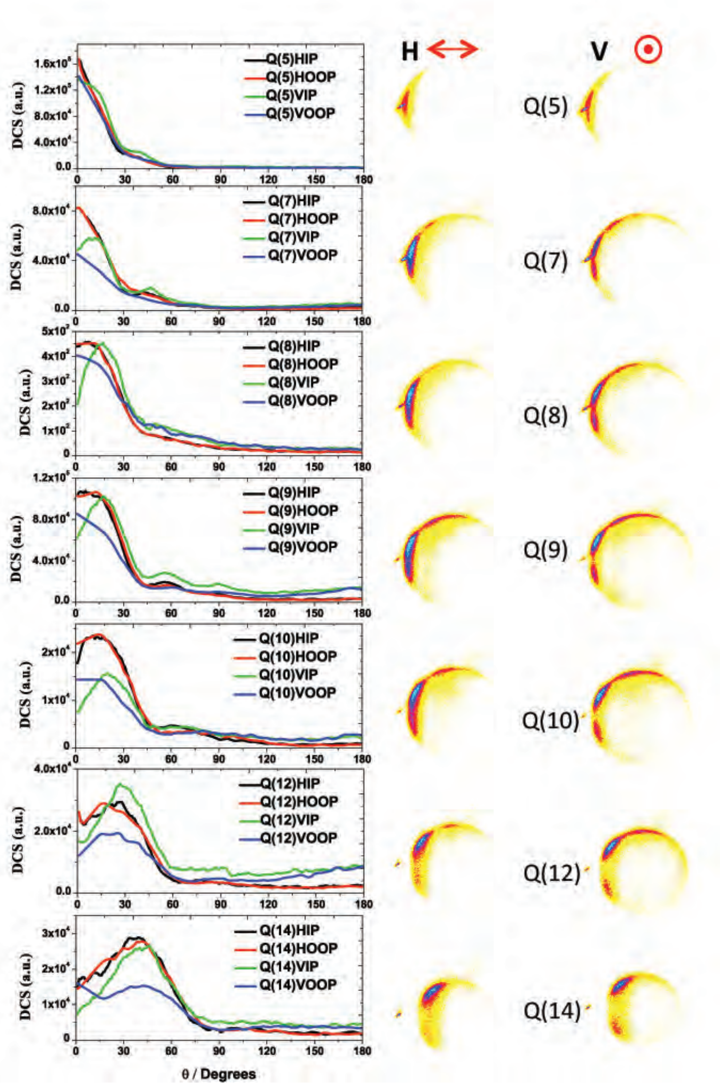

Figure 4.3: The panels show the PDDCS obtained from the experimental H and V images. From the H experimental image we have extracted HIP and HOOP signal represented as black and red color while VIP and VOOP signal were extracted from V image are in green and blue color respectively. The right panel shows the experiment image of CO-Ar system obtained with Horizontal and Vertical polarization of light.

scattering which is in accordance with conventional scattering dynamics. The match between theory and experiment is poor in the forward direction; they match quite well from sideways to backward scattering regime. The discrepancy between theory and experiment in forward scattering especially for higher states can be attributed to many factors. One of the key factors is the presence of elastic scattering in forward scattering regime where the collision cross section is comparatively very high to inelastic scattering. The presence of higher states in the parent beam can also lead to higher cross section, which has been shown in Chapter 5. The middle panel in Figure 4.4 shows the $A_0^{(2)}(\theta)$ moment which goes from positive values in the forward direction to high negative values in the backward direction. This trend is very similar to observations in the work of Brouard et al on NO-Ar collisions(25). In the CO-Ar system the 'propeller' like alignment is dominating the forward direction while 'Frisbee' like alignment is mostly dominates backward scattering. The $A_0^{(2)}(\theta)$ moment also shows deviation in forward direction which could be due to presence of elastic scattering as the collision-induced alignment effect due to elastic scattering and inelastic scattering are opposite in nature.(112)The right panel in Figure 4.4 shows $A_2^{(2)}(\theta)$) moment, which shows oscillations which are also predicted by theory. Though the experimental signal is noisy, it captures the essence of the theoretical predictions.

4.4 Conclusion

We have shown that the analysis method for extraction of polarization dependent differential cross sections directly from the experimental data works quite well for CO-Ar collisions when using the VUV REMPI detection scheme. Differential cross sections (DCSs) and alignment parameters for a range of final j' values of CO were obtained and there was good agreement of the experiment with the high level ab initio theory predictions. The trends observed were similar to those reported for the NO-Ar system,(25; 26; 28) and are in good agreement with the intuitive predictions of 'frisbee' versus 'helicopter' motion provided by the classical kinematic apse model. The derived CO-Ar PDDCSs are more reliable for CO-Ar than those from the CO-He study in Chapter 5,(112) which reflects the larger cross sections and more favorable kinematics for Ar compared to He scattering. The direct analysis method relies on integration along a stripe through the plane of the 2-D crushed image and thus partial slicing should be avoided. This is possible for inelastic scattering images which (even for CO-Ar) are still relatively small. We are currently testing direct analysis adapted for partial slicing using CO images for OCS and CO_2 photodissociation around 154 nm with VUV $(1+1^{'}+1^{''})$ REMPI.

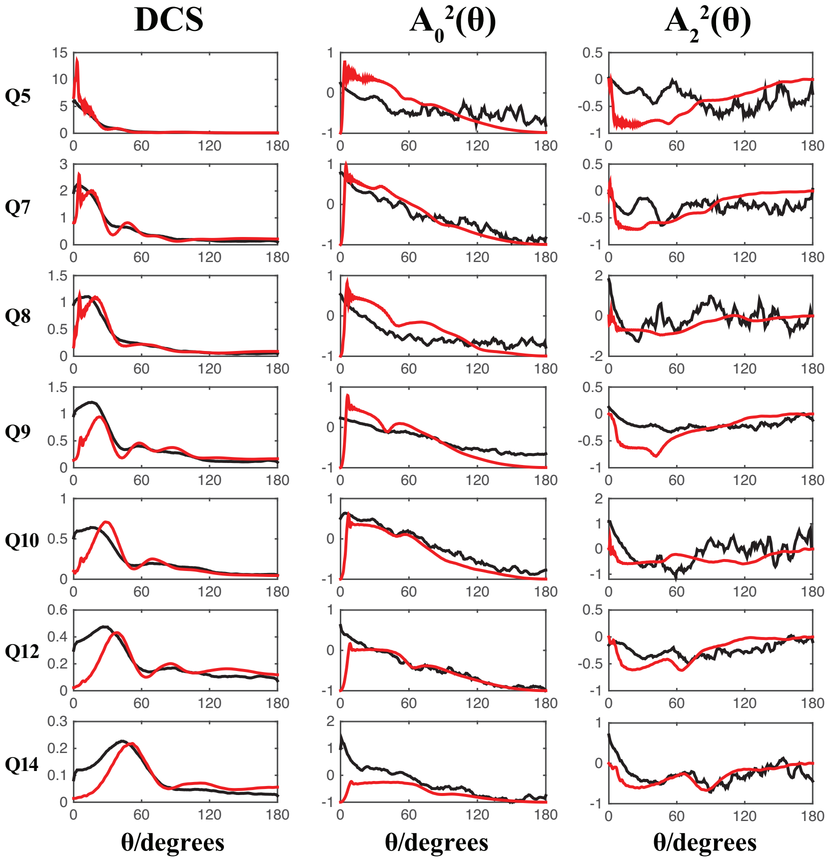

Figure 4.4: The left panel shows the conventional DCS obtained from experimental images obtained from the H & V polarization of light. This DCS is free from alignment modulation. In order to visualize both, the cross section and angular distribution the DCS is weighted by sinθ. The middle and right panels show the $A_0^{(2)}$ *and* $A_{2+}^{(2)}$ *moments extracted with direct extraction method as described in Chapter 3. The black graph represents the experimental extracted data while the red graph represents the theoretical calculations.*

Chapter 5

Inelastic scattering of CO with He: polarization dependent differential state-to-state cross sections

Abstract:[1] This chapter shows the study of state-to-state rotationally inelastic polarization dependent differential cross sections (PDDCSs) for Carbon Monoxide (CO) ($v = 0, j = 0, 1, 2$) molecules colliding with helium is reported for collision energies 513 and 840 cm^{-1} . In a crossed molecular-beam experiment, velocity map imaging (VMI) with state-selective detection by (2 + 1) and $(1 + 1^{'} + 1^{''})$ resonance enhanced multi-photon ionization (REMPI) is used to probe rotational excitation of CO due to scattering. While the supersonic expansion used to rotationally cool the CO is efficient ($T_{rot} \sim 3K$), contributions from the remaining 20% & 30% population of the $j = 1$ state are experimentally not possible to separate from those of CO (j= 0). By taking account of the known fractions of j= 0, 1 and 2, *ab-initio* theory based on high quality potential energy surfaces for the CO-He interaction is used to simulate the differential cross sections for the mixed initial states. Using polarization-sensitive $(1 + 1^{'} + 1^{''})$ REMPI detection and a direct analysis procedure described in Suits et al(116), alignment moments are extracted from the images and compared with images simulated by theory using the calculated DCS and alignment moments. In general, good agreement of theory with the experimental results is found, indicating the reliability of the experiment in reproducing state-to-state differential and polarization-dependent differential cross sections

---

[1] Adapted from: Lei Song, Gerrit C Groenenboom, Ad van der Avoird, **Chandan Kumar Bishwakarma**, Gautam Sarma, David H Parker, and Arthur G Suits. *Inelastic Scattering of CO with He: Polarization Dependent Differential State-to-State Cross Sections.* The Journal of Physical Chemistry A, 119(50):1252612537, 2015.

5.1 Introduction

Rotational excitation of diatomic molecules by collisions with atoms has been studied in intricate details over past few years, particularly for collisions of Argon (Ar) with the molecule Nitrous oxide NO(129; 116; 27), where state-to-state measurements of collision-induced orientation and alignment of the NO final rotational angular momentum as a function of scattering angle has been determined. Recently, these measurements on NO-Ar have been extended to study the effects of pre-orientation of the NO molecular axis before collision(95). Because these are nearly perfect experiments where all reactant and product variables are controlled, they form a suitable challenge for ab initio quantum theory. In practice, the systems studied so far are simple enough that theory at present has proven to be more accurate than experiment, even for the open-shell NO molecule. In this case, imperfections in experiment, noted as deviations from theory, can then be identified, accounted for, and/or improved. This bootstrap process is necessary to prepare for experimental studies of scattering processes involving more than 3-4 atoms, which offer significant challenges for a fully quantum theoretical treatment. In this direction, encouraging agreement has already been found between advanced experiment and semi classical or reduced dimensional quantum theory for the systems OH-O(69), H_2O-H_2(138), NH_3-H_2(120) and CH_3-N_2(119) for example. In this Chapter, we describe the experimental and theoretical study at a similar level of detail as for the recent studies on NO-He/Ar, but now for collisions of He with the closed-shell molecule CO. There is a long history of CO-He inelastic scattering studies, as outlined later in this section. An experimental study with angular momentum polarization-sensitive state-selective detection of CO is, however, far more challenging than for NO because the excited electronic states that can be used as a resonance step for CO lie deep in the vacuum ultraviolet (VUV). Although CO inelastic scattering is less challenging for ab initio full quantum theory than NO, prediction of state-to-state polarization-dependent differential scattering cross sections (PDDCS) for CO-He elastic and inelastic scattering, as described here, has not been reported. In our experiment, we utilize two different laser ionization detection schemes with resonance enhanced multiphoton ionization (REMPI) of CO in the (2+1) and $(1 + 1^{'} + 1^{''})$ configurations, couple this with velocity map imaging (VMI) detection(41), and measure (PD)DCSs describing collisions of CO ($j = 0; 1; 2$) with helium at collision energies 513 and 840 cm^{-1}. Here, j refers to an initial rotational state of CO while j' refers to a nascent state populated by collision. (2+1) REMPI detection of CO via the E-state(60) is highly efficient, convenient, and for our conditions, polarization insensitive, and thus useful for extracting the pure DCS. We have shown in Chapter 3 & 4 that the $(1+1^{'}+1^{''})$ detection method for CO-Ar collisions is both polarization sensitive and produces high-resolution images. Taking advantage of the sharp and polarization sensitive images, we demonstrated a simple scheme for extracting the polarization moments describing collision-induced alignment for the CO-Ar (final CO state j'= 9) system directly from the measured VMI images. We test this method here for

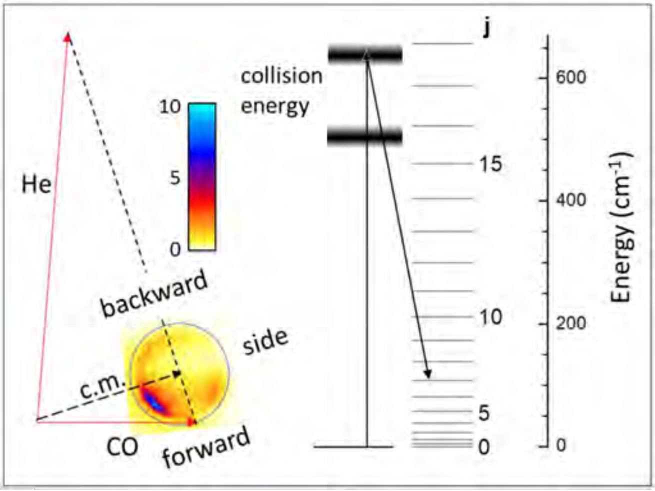

Figure 5.1: Left: Newton diagram with velocity vectors for He and CO molecular-beams crossed at an angle of 85°, center of mass (long dash) and relative velocity vectors (short dash). The circle represents elastic scattering (j = 0 final state), corresponding to a collision energy of 840$\pm$*40*cm^{-1}*. An image for the CO* $j^{'}$ *=7 final state is in set in the circle, and a color bar is shown to decode the signal level. Positions of forward, sideways, and backward scattering are indicated. Right: Energy level diagram with CO rotational energy spacings and energetics for excitation of* $j = 0$ *to* $j^{'} = 7$ *at 840* cm^{-1} *collision energy. Measurements at 513* cm^{-1} *collision energy where* $j^{'} = 15$ *is the highest energy final state are also reported here.*

CO-He collisions for a range of final rotational $j^{'}$states of CO.

CO-He has served as a benchmark for energy-transfer dynamics, and also as a model for the CO-H and CO-H_2 collision systems. Earlier work has been done in order to identify the key aspects of the potential energy surface. Early molecular-beam experiments on CO-He was reported by Butz et al in 1971(33), and Nerf et al in 1975 presented the first experimental evidence of sensitivity to anisotropy of the CO-He potential(94). Antonova et al(8) measured relative state-to-state integral cross sections for rotational excitation of CO in collision with helium at collision energies of 583 and 720 cm^{-1}. They compared their experimental data with results from two high quality potential energy surfaces, the ab initio SAPT surface of Heijmen et al. and with the XC (fit) surface of LeRoy et al(75) and found better agreement for the SAPT surface(57). Lorenz et al measured state-to-state differential cross sections for rotational excitation of CO in collision with Ne at collision energy near 511 cm^{-1} and they have compared their experimental data with results based on the CCSD(T) surface of McBane and Cybulski and the surface of Moszynski et al(81)(85)(93). In 2004, Smith et al.(109) reported state-to-state rotational transition rate constants for CO-He obtained from infrared double resonance measurements and scattering calculations based upon the SAPT potential of Heijmen et al. Their work provided a nice demonstration of the quality of the SAPT potential. This chapter presents the collision-induced alignment effect for CO-He observed experimentally. It also shows the comparison of the differential cross sections from our experimental measurements with the theoretical calculations. Carbon monoxide is of high astrochemical relevance. Radiation emitted by CO is commonly used as a tracer to extract astrophysical parameters, as the rotational transitions of the asymmetric molecule CO provide the best means to determine the physical conditions of the interstellar medium. Many models of the processes occurring in such environment are based on the assumptions of local thermodynamic equilibrium (LTE). However when investigating the hot stars, low-density chromospheres and the coronae of the solar-type stars the LTE approximations breaks down and for which non-LTE modeling is required. Successful modeling of observed CO spectral lines requires depends on the accuracy of collision rate coefficient of CO with its collision partners. Rate coefficients are commonly obtained by theoretical calculations. The quality of these rate coefficients is tested by experimental data. Differential cross sections (DCS) measured in crossed-molecular-beam experiment have shown to provide one of the most stringent tests for state-of-art theoretical calculations.(77; 76) To introduce the energetics of the CO-He imaging experiment, a Newton diagram and a typical scattering image for the $j^{'} = 7$ final state of CO is shown in Figure 5.1. The images are two-dimensional 'crushed' projections of the three-dimensional velocity spheres, having the form of a ring displaced from the center of the image (zero velocity position) by the velocity of CO relative to the center-of-mass velocity. The variation of the intensity around the ring provides the nature of scattering, e.g., forward or backward scattering, which in turn reveals the nature of the interaction between the colliding species.

5.2 Experimental methods

The data were collected in a crossed molecular-beam machine with a variable beam crossing angle and REMPI ionization of the scattered products with velocity map imaging detection which is described in more detail in Chapter 2 & 4. For the experiment of CO-He system, we used two skimmed supersonic beams, one of neat helium produced from a Nijmegen pulsed valve and the other of 2% CO seeded in argon produced from a second Nijmegen pulsed valve. For CO-He system, we utilized (2+1) & $(1 + 1^{'} + 1^{''})$ REMPI for the DCS measurement. Rotational populations of the parent CO/Ar beam were obtained from the (2 + 1) REMPI spectrum of the $E^1\Pi \rightarrow X^1\Sigma^+$ transition of CO.(30) Similar to the results of Antonova et al,(8) the population of $j = 0$ was about 65% and of $j = 1$ about 33%, corresponding to a rotational temperature of 3 K, and a small fraction of higher states with a close to thermal distribution are present. By comparing the PGOPHER(132) simulated spectrum with the experimental one, we can determine the most favorable

REMPI line positions for detection of higher rotational states, which is the prerequisite information for state-to-state inelastic scattering studies. Under collision conditions, depletion of the CO $j = 0$ ground state was measured to be less than 10%, which should ensure a single inelastic collision.(77)(76) The scattered product was ionized using either (2 + 1) or $(1 + 1^{'} + 1^{''})$ REMPI, and the ionic velocity sphere extracted by a velocity map imaging electrostatic lens. Typically, 20-50 000 laser shots were averaged for each image, under interleaved conditions with and without the He beam in time overlap with the CO beam. The second condition was used for background subtraction; difference images are taken when the final-state population in the parent is significant and overlaps the scattered-in final-state image. This subtraction method is not ideal; it leads to problems, especially in the forward scattering region, as discussed later in the text. The laser frequency was fixed during each image collection, rather than scanning the wavelength over the full width of the Doppler profile of the REMPI transition (0.07 cm^{-1} for inelastic scattering of CO from He), because the laser bandwidth with both (2 + 1) and $(1+1^{'}+1^{''})$ REMPI is ~0.1 cm^{-1}. For (2 + 1) REMPI the 2 mJ energy per pulse power broadening of the transitions was also sufficient to make Doppler scanning unnecessary for (2 + 1) REMPI on the $E^1\Pi \rightarrow X^1\Sigma^+$ transition, well-resolved and strong S-branch transitions around 215 nm were used for data collection. Ultraviolet (UV) laser energies were typically ≈2 mJ per pulse in pulses of duration 4-6 ns. The probe beam was focused with a 20 cm lens onto the intersection region of the molecular-beams. For (2 + 1) REMPI of CO the $E^1\Pi$ state was used as the resonant state instead of the commonly used $B^1\Pi$ state where the low-j levels are overlapped. Detection on the S-branch of the $E^1\Pi$ state should in principle be polarization sensitive but repeated measurements (under the same experimental conditions as $(1+1^{'}+1^{''})$ REMPI) did not reveal any sensitivity to the laser polarization. Due to the low ionization efficiency and small probe volume, it was necessary to use 2 mJ laser pulse energy, which is likely to be too high to retain polarization sensitivity. Antonova et al.(8) used 100 μJ per pulse, for example, and estimated that the maximum polarization effect in the integral cross section for CO-He scattering with E-state detection was less than 10%.

Experiments employing $(1 + 1^{'} + 1^{''})$ REMPI of CO were described briefly in Chapter 4. The collision energy was 840 cm^{-1} for the geometry used for the $(1+1^{'}+1^{''})$ REMPI detection experiments. This is higher than in the (2 + 1) REMPI detection experiments due to a different mounting of the pulsed valves, which led to a higher equilibrium temperature after warming up. The collision energy was estimated for both REMPI detection methods by combining data both from the initial beam velocities and from the size of the images as a function of the final rotational state $j^{'}$. The PGOPHER program(132) was used to fit the CO $X \rightarrow A$ $(1 + 1^{'} + 1^{''})$ REMPI transition, which shows P, Q, and R branches of similar intensities, and (as with the (2 + 1) REMPI spectrum) a rotational temperature of $\sim$ 3 K. This similarity indicates that the ionization step in the $(1 + 1^{'} + 1^{''})$ process does not significantly perturb

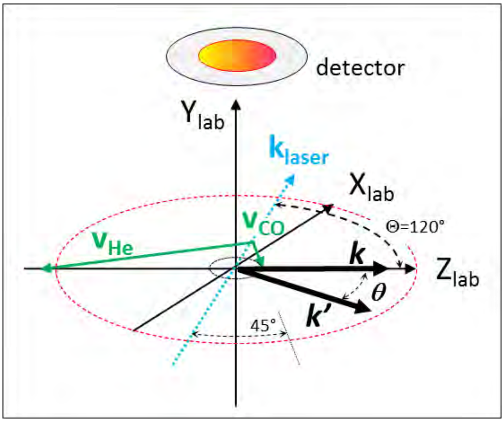

Figure 5.2: Definition of the laboratory frame coordinate system for the He-CO scattering process.

the spectrum. The measured images for the same $j^{'}$ are different when a P, R, or Q branch transition is used. For the same transition branch the images differ with H (VUV laser polarization direction in the scattering plane) versus V polarization where the VUV polarization is directed perpendicular to the scattering plane, along the time-of-flight axis, as shown later. As described in ref (116), all H and V polarization images were obtained for Q-branch transitions. The raw H and V images were first converted from density-to-flux using the IMSIM program, although for the polarization analysis method this was not essential. The asymmetry in the raw images disappears to a large extent upon density-to-flux correction. Because the effective angular resolution varies widely with scattering angle, the images still do not look fully symmetry after correction. The density-to-flux correction is a secondary effect in that at any scattering angle the alignment moments are obtained by differences divided by the DCS. For each $j^{'}$ final state, two angular distributions were extracted from the H and V images by integrating over the outside annulus of the image, or over a stripe through the middle of the image along the initial relative velocity vector, as described in Chapter 3 & 4(116). This yields four polarization angular distributions: HIP, horizontal in-plane; VIP, vertical in-plane; HOOP, horizontal out-of-plane; and VOOP, vertical out-of-plane polarization. An important difference between the present CO-He experiment and the CO-Ar experiment described in Chapter 4 is the direction of laser propagation, k_{laser}. Using the standard reference frame as sketched in Figure 3, the z axis is parallel to the initial relative velocity vector k, xz is the scattering plane containing $k^{'}$ and the product relative velocity vector k, and the y axis is parallel to k and $k^{'}$. Using linearly polarized light, the electric field of the laser can be directed either along z (labeled horizontal or H polarization) or along the ion time-of-flight axis y (vertical, V polarization) when k_{laser} is directed along the x axis. In the laboratory frame, k_{laser} is the same as in the CO-Ar experiment, fixed at an angle of 45° with the CO initial velocity vector v_{CO}.

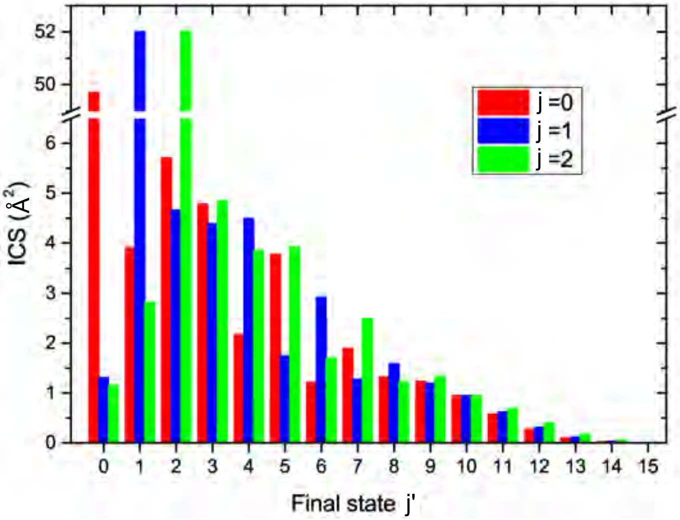

Figure 5.3: Integral cross sections for elastic and inelastic scattering from the initial j *= 0, 1, 2 states to the* $j^{'}$ *= 0-15 final states at collision energy 513* cm^{-1}.

In the CO-Ar case, this angle and the angle of 85° between the CO and Ar beams, cf. Figure 5.2, implied that the laser beam was perpendicular to the initial relative velocity vector k. Also in the CO-He experiments the CO and He beams cross at an angle of 85° and for the collision energy of 840 cm^{-1}, where the CO final-state detection is polarization sensitive, the velocities of CO and He are such that the angle between k_{laser} and k is 120°. The implications of this different geometry are discussed later in the text.

5.3 Results & Discussion

5.3.1 Theoreticals Results

This section of the chapter only gives a brief overview from the theoretical methods. More detail about the theoretical method is described in Ref.(112; 12; 57; 105) Differential, Integral and polarization-dependent differential state-to-state cross-sections for CO-He collision were calculated with the quantum closed coupling method.(12) These potentials were also compared for calculations of the differential cross sections from the initial state with j = 0 to the final states $j^{'}$ = 1, 4, 8, and 12 at a collision energy of 513 cm^{-1}. The DCSs show the expected trend of the cross section decreasing and more backscattering as the final state increases. While the peaks in the DCS for the CBS potential are slighted shifted to smaller scattering angles (corresponding to higher collision energy or a more attractive PES), the shifts are quite small. Figure 5.3 presents the elastic and inelastic integral cross sections ICSs from the initial states with $j = 0, 1, 2$ to the final states with $j^{'}$ up to 15. Elastic ($j = j^{'}$) integral cross-sections are typically 1-2 orders of magnitude stronger than the inelastic cross sections. For the later, the cross sections obviously depend strongly on Δj and they decrease for larger j values because of the larger energy gap between the higher rotational states. As mentioned in the experiment section, the present experiment does not achieve pure initial state selection; the parent CO beam contains a mixture of j= 0, 1, and 2 states, which due to their differing internal energy and quantum numbers show widely varying scattering behavior.

5.3.2 Vector Correlations

Investigations of vector correlations in inelastic scattering processes reveal valuable information on the underlying dynamics.(25) Most previous studies have used different expressions for describing the angular momentum distributions describing inelastic scattering, which are generally presented in terms of renormalized PDDCSs. Brouard et al(25) listed the relationship between the polarization moments and alignment parameters used in various papers. We present our alignment results in terms of the Herte-Stoll renormalized $A_q^k(\theta)$ polarization parameters, which are the irreducible components of the scattering density matrix related to the classical probability density function. They are defined in the scattering frame with the z-axis along the initial relative velocity vector k. $A_0^{(0)}(\theta)$ is directly related to the conventional DCS, which reveals the vector pair correlation between the initial and final relative velocity vectors k and $k^{'}$, and θ is the angle between k and $k^{'}$ in the collision plane, as shown in Figure 5.2. Polarization-dependent differential cross sections (PDDCS), represented by the $A_0^{(2)}(\theta)$, $A_{1+}^{(2)}(\theta)$, and $A_{2+}^{(2)}(\theta)$ polarization moments, describe the triple correlation between k, $k^{'}$ and the final rotational angular momentum j. In the case of inelastic atom-molecule scattering, the A_0^2 (θ) moment for the $j^{'}$, k correlation is related to the population of the $j^{'}$ substates with different $m_{j'}$. It ranges from -1 when $j^{'}$ is perpendicular to k to +2 when $j^{'}$ is parallel to k. Its value is sometimes expressed as the degree of ‘frisbee’ ($j^{'} \perp k$, $k^{'}$) versus ‘propeller’ ($j^{'} \parallel k$, $k^{'}$)alignment of the final angular momentum $j^{'}$ with respect to the k, $k^{'}$ scattering plane. The $A_{1+}^{(2)}$ (θ) and A_{2+}^2 (θ) moments contain the off-diagonal elements of the density matrix; they range from -1 to +1. Introduction of the linearly polarized laser beam propagation along k_{laser} in Figure 5.2 breaks the cylindrical symmetry along k and allows probing of the propensities for alignment of $j\ j^{'}$ relative to the X, Y, Z axes of the collision frame, where k lies along Z_{coll}. In the laboratory frame, Figure 5.2, the present CO-He collision study differs from the Ar-CO collision study described in Chapter 3 & 4. In the Ar-CO experiment the laser beam crossed k at 90°; i.e. it was parallel to X_{lab} in Figure 5.2. Due to the different relative velocity, this was not possible for CO-He and the laser now propagates at an angle of 120° with k and thus with Z_{lab}. In the lab-to-collision frame transformation described in ref 14, the frame rotation angle θ becomes $\theta = 120°$ instead of $90°$, as is discussed in more detail later in the text. Algebraic combination of the four experimental HIP, HOOP, VIP, and VOOP distributions yields the polarization moments for the angular distributions: $A_0^{(2)}(\theta)$, $A_{1+}^{(2)}(\theta)$, and $A_{2+}^{(2)}(\theta)$, as well as $A_0^0(\theta)$, which is the DCS.

5.3.3 Experimental Results

Angular distributions extracted from velocity map images for collision-induced alignment from rotational energy-transfer processes can be expressed in the form

$$I(\theta) = C\frac{d\sigma}{d\theta}\Big[(1 + \sum_{kq} A_q^{(k)}(\theta)F_q^{(k)}(\chi, \Theta, \phi)\Big] \tag{5.1}$$

where $\frac{d\sigma}{d\theta}$ is the DCS, C is a constant factor that includes the effect of the density-to-flux correction, and the quantity in square brackets describes the renormalized alignment distribution. The function $F_q^{(k)}(\chi, \Theta, \phi)$ contains all information on the experimental variables needed. In the case of (2 + 1) REMPI detection, described first in this section, the experimental conditions are such that the $F_q^{(k)}(\chi, \Theta, \phi)$ values in equation 5.1 are effectively zero (i.e., there is no alignment sensitivity in the experiment) and the DCS can be determined directly from the density-flux corrected image and compared with theory. Next, the angular distributions determined using polarization-sensitive $(1 + 1^{'} + 1^{''})$ REMPI detection are described.

Differential Cross Sections at 513 cm^{-1} Collision Energy Using (2 + 1) REMPI Detection.

Raw images taken at 513 cm^{-1} collision energy with (2 + 1) REMPI detection are shown on the left-hand side of Figure 5.4 for final states in the range $j^{'} = 3 - 11$. Simulated images from the IMSIM program, which account for the divergence and velocity spread of the molecular-beams and their relative timing, as well as the laser ionization timing, volume, and propagation direction, are shown in the middle column. All final states from $j^{'} = 3$ to 11 were measured except for $j^{'} = 5$, in which case the S(5) and R(11) branches are fully overlapped. The S(6) transition is also overlapped with R(15), but the latter final state is very close to the energetic limit; its population is thus negligible.

As mentioned previously, detection with (2 + 1) REMPI under our experimental conditions showed no measurable sensitivity to the direction of the laser polarization. The experimental DCSs from the IMSIM program are shown on the right-hand side of Figure 5.4 and compared with theoretical predictions.

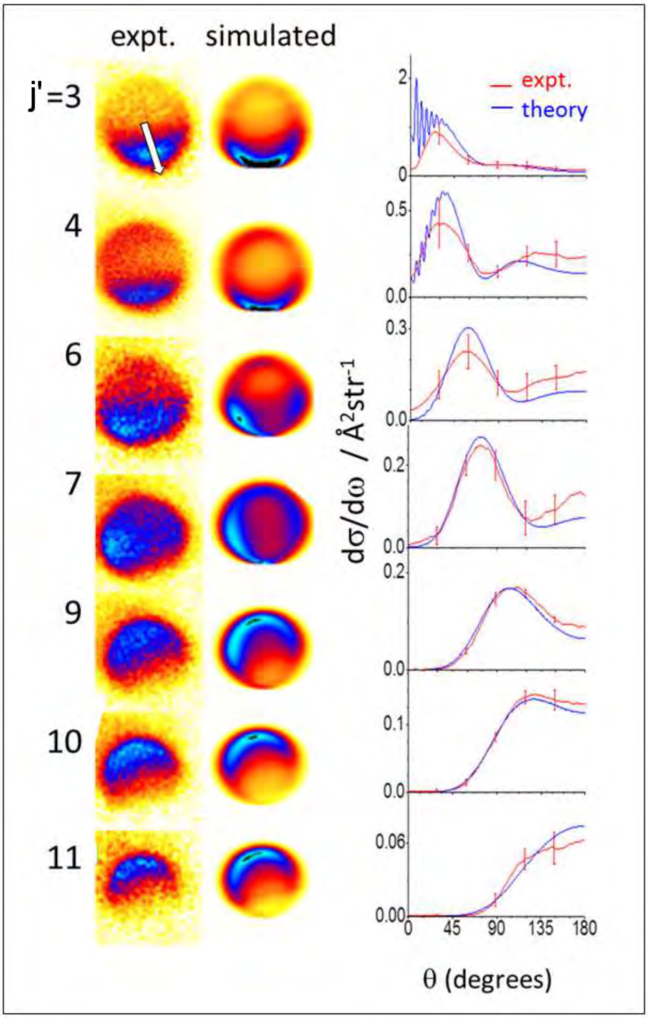

Figure 5.4: Raw experimental two-dimensional velocity map images of the $j^{'} = 3 - 11$ final states using (2 + 1) REMPI detection at collision energy $513 \pm 40\ cm^{-1}$, on the left-hand side. The direction of the initial relative velocity vector is shown as a white arrow in the image for the $j^{'} = 3$ state. The color code is shown in Figure 5.1. Images simulated using the IMSIM program are shown (middle column) for comparison with the experimental image. On the right-hand side experimental DCSs are compared with theoretical predictions for each final state, where the experimental curve is scaled by a constant factor to match theory.

Table 5.1: Geometric factors for indicated distributions.

	HIP	HOOP	VIP	VOOP
(χ,Θ,ϕ)	$(\pi,\frac{2\pi}{3},0)$	$(\pi,\frac{2\pi}{3},\frac{\pi}{2})$	$(\frac{\pi}{2},\frac{2\pi}{3},0)$	$(\frac{\pi}{2},\frac{2\pi}{3},\frac{\pi}{2})$
$F_0^{(2)}$	0.625	0.625	-0.5	-0.5
$F_{1+}^{(2)}$	0.375	-0.375	0.375	0.375
$F_{2+}^{(2)}$	0.217	-0.217	-0.87	0.87

Polarization-Dependent Differential Cross Sections at 840 cm^{-1} Collision Energy.

In previous work on collision-induced alignment in NO-Ar collisions,(25) (26) reasonable assumptions were made to extract the DCS and alignment functions from the data. The DCS was extracted from the image data $I(\theta)$ by assuming the $A_q^k(\theta)$ values from the kinematic apse model (26)(68) or from a full quantum mechanical (QM) scattering calculation. For determining the $A_q^k(\theta)$ values, the DCS was taken from the QM calculations. Note that three polarization parameters can be predicted from the kinematic apse model and all three are measurable. The $A_{q1+}^2(\theta)$ parameter, however, is not accessible when k_{laser} is perpendicular to the initial velocity vector k, as in the CO-Ar experiment described in ref(116). The frame transformation angles and functions $F_q^{(k)}(\chi,\Theta,\phi)$ for the geometry in the present experiment are given in Table 5.1.
Following the procedures outlined in Chapter 3(116), the $F_q^{(k)}(\chi,\Theta,\phi)$ factors are combined with the polarization moments to yield the angular distribution for each polarization geometry as

$$I_{HIP}(\theta) = \frac{d\sigma}{d\theta}(\theta)C[1 + 0.625A_0^{(2)}(\theta) + 0.375A_{1+}^{(2)}(\theta) + 0.217A_{2+}^{(2)}(\theta)] \quad (5.2)$$

$$I_{HOOP}(\theta) = \frac{d\sigma}{d\theta}(\theta)C[1 + 0.625A_0^{(2)}(\theta) - 0.375A_{1+}^{(2)}(\theta) - 0.217A_{2+}^{(2)}(\theta)] \quad (5.3)$$

$$I_{VIP}(\theta) = \frac{d\sigma}{d\theta}(\theta)C[1 - 0.5A_0^{(2)}(\theta) + 0.375A_{1+}^{(2)}(\theta) - 0.87A_{2+}^{(2)}(\theta)] \quad (5.4)$$

$$I_{VOOP}(\theta) = \frac{d\sigma}{d\theta}(\theta)C[1 - 0.5A_0^{(2)}(\theta) + 0.375A_{1+}^{(2)}(\theta) + 0.87A_{2+}^{(2)}(\theta)] \quad (5.5)$$

In the setup of HIP and HOOP distributions must be identical, so that the position and scaling of the rectangular region used to obtain the HOOP distribution could be adjusted to match the HIP distribution. The same position and scaling could then be used for the VOOP distribution. Here, we have θ= 120° and it is apparent from the above equations that HIP and HOOP are not identical, so that this scaling method is not applicable. A solution to this problem is to measure also at a different k_{laser} direction; for example, at θ= 0° where VIP = HOOP and HIP = VOOP. As this proved inconvenient, theory was again called on, and the relative cross sections from theory were used to calibrate the experimental scaling factor relating the HIP and HOOP curves. The same scaling was then applied to the experimental VIP and VOOP distributions. In this approach, the length of the integration region for HOOP and VOOP was fixed at the average radius of the annulus used for the HIP and VIP integrations. Linear combination of the expressions in equation 5.2, 5.3, 5.4 & 5.5 yields the differential cross section.

$$\frac{d\sigma}{d\theta}(\theta)C \approx \frac{1}{4}\Big[I_{HIP}(\theta) + I_{HOOP}(\theta) + I_{VIP}(\theta) + I_{VOOP}(\theta)\Big] \tag{5.6}$$

$$\frac{d\sigma}{d\theta}(\theta)C = \frac{d\sigma}{d\theta}(\theta)C\Big[1 + \frac{1}{16}A_0^{(2)}(\theta) + \frac{3}{16}A_{1+}^{(2)}(\theta)\Big] \tag{5.7}$$

where, considering the small values of their scaling coefficients and their tendency to cancel each other, the last two terms in equation 5.7 are ignored. This approximation was confirmed to be valid by comparing the exact and approximate forms of equation 5.2, 5.3, 5.4 & 5.5 using the polarization moments and DCS from theory. Other combinations yield the polarization parameters:

$$A_0^{(2)}(\theta) = \frac{1}{4}\Big[\frac{I_{HIP}(\theta) + I_{HOOP}(\theta)}{\frac{d\sigma}{d\theta}(\theta)C} - 2\Big] \tag{5.8}$$

$$A_{1+}^{(2)}(\theta) = \frac{1}{4}\Big[\frac{I_{HIP}(\theta) + I_{HOOP}(\theta)}{\frac{d\sigma}{d\theta}(\theta)C} - 0.43A_{2+}^{(2)}(\theta)\Big] \tag{5.9}$$

$$A_{2+}^{(2)}(\theta) = \frac{I_{VOOP}(\theta) - I_{VIP}(\theta)}{1.74\frac{d\sigma}{d\theta}(\theta)C} \tag{5.10}$$

(4) where the two combinations for $A_{1+}^{(2)}(\theta)$ from the experimental data were averaged. As shown in ref(116), $(1+1^{'}+1^{''})$ REMPI of CO allows measurement of polarization-dependent DCSs. Both V and H polarization images measured for $j^{'}$ = 5-14 final states using $(1 + 1^{'} + 1^{''})$ REMPI detection on Q-branches around 154 nm are shown in Figure 5.5. In these measurements the collision energy is 840±40cm^{-1}. For the $j^{'}$ = 5 state a CO-beam-only image was subtracted from the CO + He image, for higher $j^{'}$ states the parent beam signal is sufficiently far from the scattering ring that subtraction was not necessary. For $j^{'}$ ¡5 no Q-branch probe transitions free of overlap with other states could be found. Raw H and V images (without density-flux correction) are shown in the left panel of Figure 5.5. HIP, HOOP, VIP, and VOOP angular distributions for each final state are shown in the middle panel of Figure 5.5. HIP and VIP curves are obtained by integration around the annulus shown schematically as circles superimposed on the $j^{'}$= 9 V image, whereas the HOOP and VOOP curves

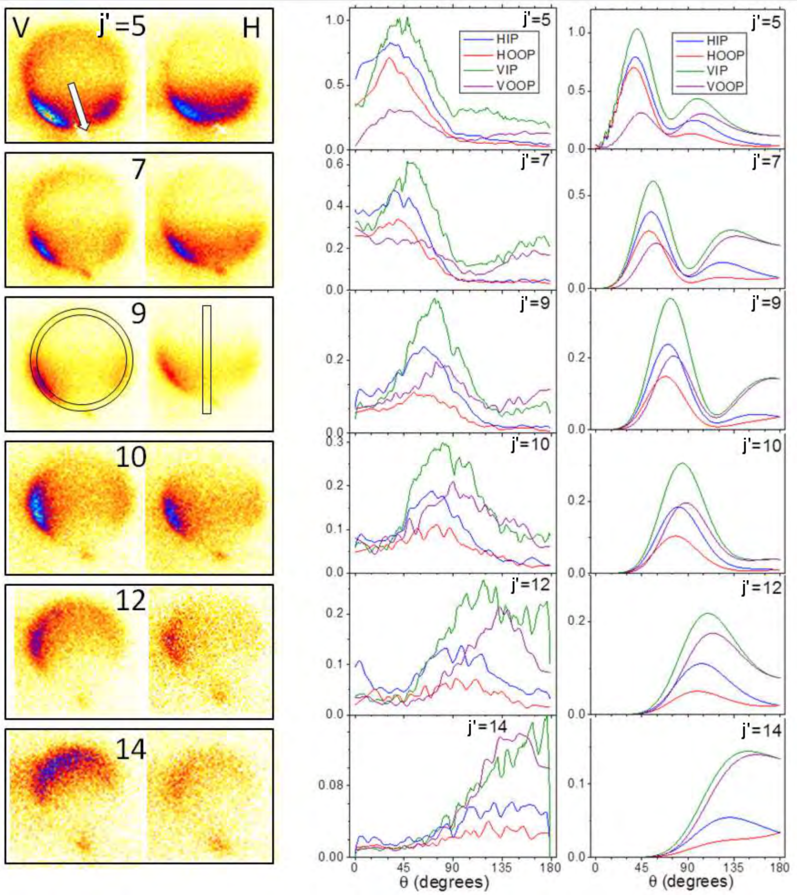

Figure 5.5: Raw two-dimensional velocity map images of the $j^{'} = 5$*-14 final states using* $(1+1^{'}+1^{''})$ *REMPI detection at collision energy 840* $\pm 40 cm^{-1}$*. The direction of the initial relative velocity vector is shown as a white arrow in the image for the* $j^{'} = 5$ *state. The polarization of the (resonant) VUV photon is indicated by V for polarization perpendicular to the collision plane and H parallel to the collision plane. The sensitivity scale for each pair of images is adjusted to make the main features visible. The middle panel shows HIP, HOOP, VIP, and VOOP distributions extracted from these images and the right panel shows theoretical predictions corrected for the laser geometry. Each experimental curve was scaled by a constant factor to match the corresponding theory curve.*

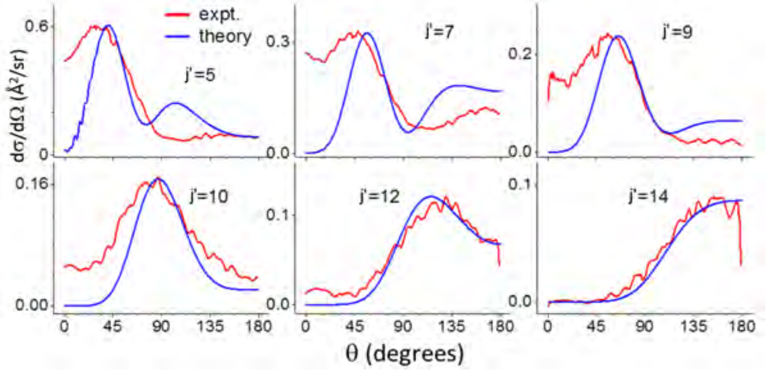

Figure 5.6: DCSs for $j^{'} = 5$-14 computed with the use of equation 5.7 from HIP, HOOP, VIP and VOOP angular distributions extracted from the measured images in comparison with calculated DCSs at collision energy 840 ± 40 *cm^{-1}*

are obtained from integration along the vertical stripes shown schematically on the $j^{'} = 9$ H image.
As a test of the HIP-HOOP scaling procedure described above, the resulting HIP, HOOP, VIP, and VOOP curves (middle column) are compared with predictions from theory shown in the right column of Figure 5.5. In all cases scaling factors did not vary by more than a factor of 2 from the amplitudes of the raw data curves. Although the noise is considerable, the shapes and areas of each experimental curve are in reasonable agreement with theory for all measured final states. DCSs obtained by application of equation 5.2, 5.3, 5.4 5.5 are compared with theoretical predictions in Figure 5.5. Polarization moments extracted from the experimental I(θ) curves are shown in Figure 5.7.

5.3.4 Discussion

CO is a closed shell molecule with a relatively small dipole moment (0.122 D), and He is a small atom with a low polarizability. Therefore,, the interaction of CO with He is dominated by short-range interactions that require small impact parameters. For this repulsive interaction system *l-type* rainbows, which have been shown to have remarkable polarization effects for NO-Kr collisions(30; 35) are not expected or seen in the theoretical analysis. Instead, the kinematic apse model(26), which describes the system classically as a hard sphere colliding with a rigid ellipsoid, should yield an accurate prediction of collision-induced alignment effects, as shown in previous studies of NO-He, Ne, and Ar collisions. Indeed, the polarization moments predicted by theory here for the CO-He system are almost quantitatively similar to those predicted for the NO-He, Ne, and Ar systems. (30; 35; 25; 95) The magnitude of the energy-transfer cross sections between CO-He and CO-Ar, however, is quite different. For example, the ICS for the $j^{'} = 7 \leftarrow j = 0$ excitation for CO-Ar is 8 times larger than that for CO-He at 513 cm^{-1} collision energy, and similar differences are found for the

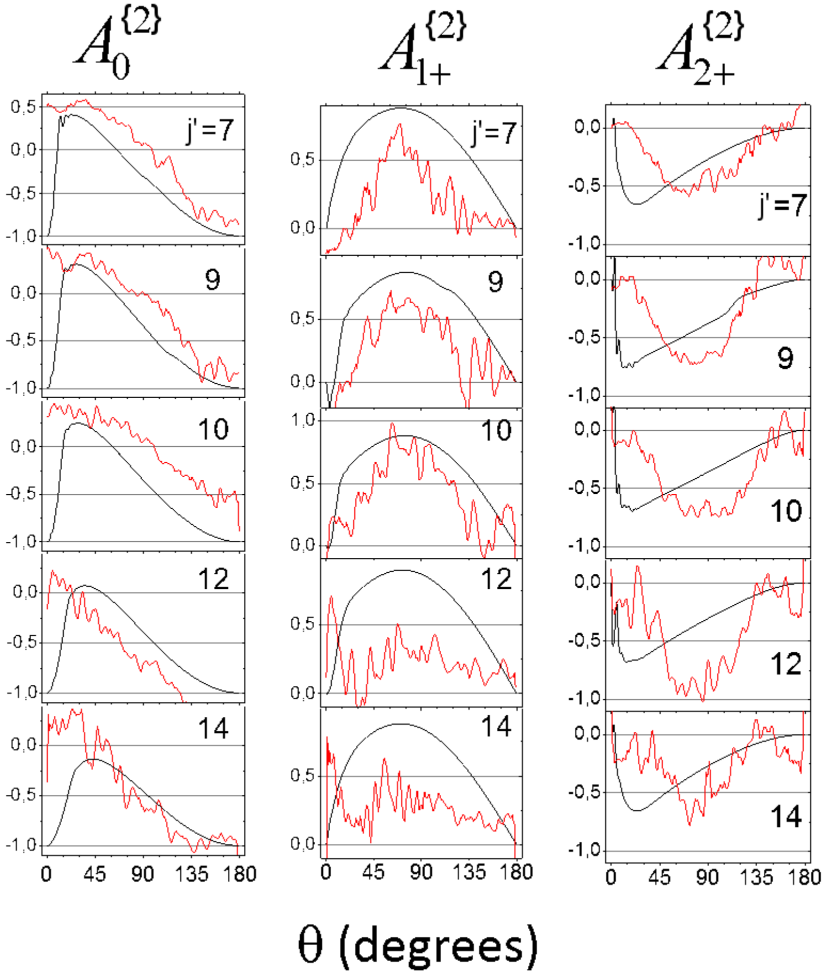

Figure 5.7: Renormalized alignment moments for j'=7-14 computed with the use of equation 5.8, 5.9 & 5.10 from the HIP, HOOP, VIP and VOOP angular distributions extracted from the measured images in comparison with calculated moments at collision energy

NO-He versus NO-Ar systems.The smaller cross sections make collision-induced alignment studies with He as the collision partner much more difficult and up to the present only Meyer(68) has reported CIA(collision-induced alignment) studies of NO-He at the (high) collision energy of 1185 cm^{-1}. CO-He is thus not an easy system for experimental study, and as expected, this results in lower quality DCS and alignment data than CO-Ar. Regardless of the small cross section, the DCSs recovered when (2 + 1) REMPI detection is used and agree quite well with theoretical predictions(Figure 5.4). Note again that theory takes into account the mixture of initial states in the experiment. With the relatively high-intensity laser pulses needed for the (2 + 1) REMPI detection, it is clearly possible to detect a significant fraction of the scattered molecules without distortion due to complete saturation or space charge. In this aspect, the laser confocal diameter is roughly 30 μm for the 20 cm focal length lens used, but the $\approx$ 1 cm confocal length of the laser beam exceeds the length of the $\approx$ 4 X 4 X 4 mm collision volume. DCSs recovered from the full polarization study using $(1+1^{'}+1^{''})$ REMPI at 840 cm^{-1} collision energy are also in reasonable agreement with theory, although for the lower $j^{'}$ final states the second rainbow peak in the side to backscattering region is broader than predicted. The shape of the DCS, especially in this region, is sensitive to the value of the polar angle θ and to the amount of $j = 0$ versus $j = 1$ in the initial beam. Considering that the experimental I(θ) curves match the shape of the corresponding theory curves (Figure 5.5), when only HIP an HOOP are scaled using theory, again confirms the general agreement of experiment and theory for the DCSs. Rescaling of the experimental curves was necessary because the total sensitivity for each image could not be held sufficiently constant when the laser polarization was rotated. The direct extraction method yields polarization parameters (Figure 5.7) that are also qualitatively in agreement with theory predictions. As is typical, the $A_0^{(2)}(\theta)$ parameter is most reliable whereas the $A_{2+}^{(2)}(\theta)$ parameter (obtained only from the VIP-VOOP curves) is noisy and quite sensitive to the scaling method. The $A_{1+}^{(2)}(\theta)$ parameters show the expected shapes in general, although for the weak and quite small $j^{'} > 10$ images substantial deviations are observed. All three experimental polarization parameters tend to reach their minimum values, in contrast to previous work on NO-rare gas studies, where typically $A_0^{(2)}(\theta)$ reached only -0.4 to +0.5 instead of -1.0 at the backscattering angle. This difference could be due to the lack of nuclear spin in CO compared to NO, where any stray magnetic field could depolarize the nascent NO on the time scale of the scattering measurement. Another effect, as suggested by Brouard and co-workers, is depolarization due to secondary collisions. In our measurement, both the DCSs and polarization parameters show significant deviation from theory in the most forward scattering direction. We believe this is due mainly to elastic scattering following the inelastic event, as discussed next. For any study of inelastic (or reactive) scattering the effects of elastic scattering must be considered. Two features of elastic scattering are a much larger total cross section and strongly forward scattering. The theoretical calculations in Figure 5.8 shows the elastic

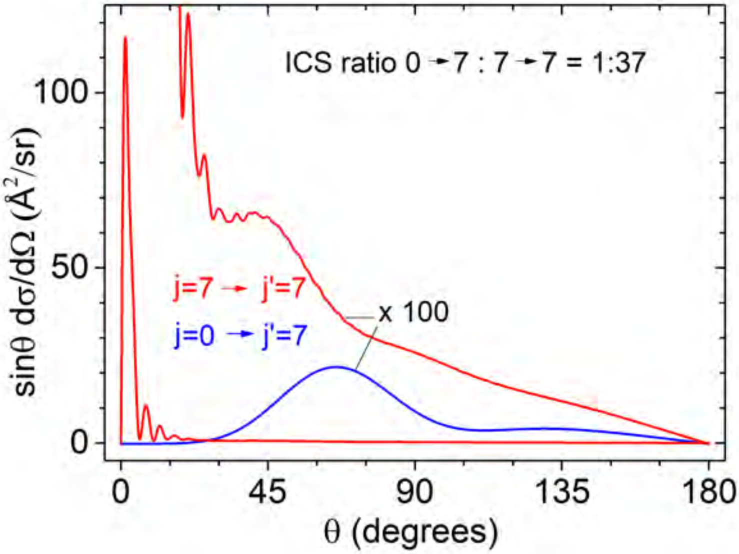

Figure 5.8: Comparison of the DCS for elastic $j = 7 - 7$ *and inelastic* $j = 0 - 7$ *CO-He collisions at collision energy 800 cm*$^{-1}$

scattering DCS for the $j^{'} = 7$ state, a typical final product measured in this study. To visualize both the magnitude of the cross section and the angular distribution, the DCS is weighted by sin θ in Figure 5.8 where the area under the curve is then the integral cross section. The $j=$ 7-7 ICS (similar to all of the other elastic ICSs) is 37 times larger than the $j^{'}$ = 0-7 ICS, which is typical for all of the lower initial states. The probability for an elastic collision after the $j^{'} = 7$ state is formed but before laser ionization takes place under the present condition of $\approx$ 5% inelastic scattering is close to 100%. Also apparent in Figure 5.8 is that although the elastic scattering is mostly forward, even at 20° there can be a significant effect on the DCS. The probability in the side scattering region for $j=$ 7-7 elastic scattering is greater than that of the 0-7 inelastic scattering event. When a final state with a substantial fraction is detected in the parent beam ($j = 1, 2, 3, ...$), the measured image will thus also reflect elastic scattering and a simple beam-off background subtraction is not valid. An elastic scattering event shows collision-induced alignment effects that tend to be opposite to those of inelastic scattering polarization which is illustrated Ref.(112) In the forward scattering region, elastic scattering can thus cause significant depolarization, and forward scattering is where the largest deviation in the polarization parameters between experiment and theory is seen in Figure 5.7. Elastic scattering will not cause significant deflection of the nascent molecules. Once inelastically scattered, however, these molecules are no longer moving with their parent beam velocity and further collisional

depolarization and elastic scattering with the carrier gas of the parent beam with much higher cross sections becomes possible.
For the present CO-He system, collisional depolarization appears to mainly affect the forward scattering region whereas the backscattering region shows the maximum possible collision-induced alignment, within the large error margin of the experiment. For the CO-Ar system where the inelastic scattering cross section is nearly an order of magnitude larger, collisional depolarization should play a more important role and this is indeed observed in the preliminary results of Chapter 3 & 4, where in the backscattering region the polarization parameters do not reach their maximum expected values. Finally, for very dilute systems such as those with hexapole or Stark deceleration state selection the probability of an inelastic collision can be sufficiently low that depolarization by elastic scattering with the rare gas partner should not be important.

5.4 Conclusion

The rotational excitation of CO molecules due to scattering with He atoms at collision energies of 513 and 840 cm^{-1} was studied in a crossed molecular-beam setup and velocity map imaging (VMI) with state-selective and polarization-sensitive detection through $(1+1^{'}+1^{''})$ and (2 + 1) REMPI. The incoming CO beam had a rotational temperature of $T_{rot} \approx 3K$ with j= 0, 1, and 2 states populated in a ratio of 65:33:2%. Differential cross sections (DCSs) and alignment parameters for a range of final $j^{'}$ values of CO were extracted from the measured images by a direct analysis procedure described by Suits et al, but generalized here to account for a different laser beam direction. The same DCSs and alignment parameters, averaged over the initial-state distribution of CO, were obtained from quantum mechanical close-coupling calculations based on two accurate ab initio potentials for CO-He. Good agreement between the experimental and theoretical results was found, in general, which illustrates the reliability of the experiment, as well as of the procedure used to extract state-to-state differential and polarization-dependent differential cross sections from the measured images.

Chapter 6

State-to-state inelastic scattering of O_2 with He

Abstract:[1]. Molecular oxygen (O_2) is extremely important for a wide variety of processes on and outside Earth. Indeed, O_2-He collisions are crucial to model O_2 abundance in space or to create ultra-cold O_2 molecules. A crossed molecular-beam experiment to probe rotational excitation of O_2 due to helium collisions at energies of 660 cm-1 is reported. Velocity map imaging was combined with state-selective detection of O_2 $^3\Delta_g^-$ by (2+1) resonance enhanced multi-photon ionization. The obtained raw O_2^+ images were corrected from density-to-flux and the differential cross sections (DCS) were then extracted for six O_2 final states. Exact quantum mechanical calculations were also performed. A very good agreement between experimental and theoretical DCSs was found using an initial O_2 beam population ratio of 80% for the first rotational state and 20% for the first excited state. The agreement demonstrates our ability to model inelastic processes between O_2 molecules and rare gas both theoretically and experimentally.

---

[1] Adapted from: **Chandan Kumar Bishwakarma**, George van Oevelen, Roy Scheidsbach, David H Parker, Yulia Kalugina, and Francois Lique. *State-to-state inelastic scattering of O_2 with helium.* The Journal of Physical Chemistry A, 120(6):868-874, 2016

6.1 Introduction

Molecular oxygen (O_2) is an extremely important species for a wide variety of processes on and outside Earth. While the O atom is the third most abundant atom in the Universe, and numerous oxygen-containing molecules like CO, H_2O, OH or NO are easily detected in the interstellar medium, the O_2 molecule itself is quite difficult to detect because of the absence of an electric dipole moment. Its highest occupied molecular orbital (π_g^2) is open shell, leading to a complex electronic structure and transitions that cannot be easily probed by standard optical spectroscopy due to the strict symmetry selection rules applicable to homonuclear diatomic molecules. The search of O_2 molecules was one of the goals of astrochemistry for several decades. Recently, emission between sub-states of the ground rotational level (see Figure. 6.1) of molecular oxygen has been observed in the interstellar medium(13). In the laboratory, O_2 can be detected by resonance enhanced laser ionization(79; 139) but because photoionization must compete with photodissociation(101) and ion fragmentation(102), it was not clear if this approach is sensitive enough for detection of the low densities of O_2 inherent in crossed-beam scattering under single collision conditions. Here, we show that differential cross sections taken under single-collision conditions can indeed be obtained using laser ionization of O_2 for comparison with state-of-the-art theoretical predictions. Much of what we know about molecules in the Universe comes from observations of emission from rotationally excited molecules, especially CO and other small molecules. As both collisions and the radiation field can excite interstellar molecules, there has thus been considerable interest in rotational excitation processes. Hence, for astrophysical applications, such studies provide state-to-state rotational inelastic scattering of a molecule with He and H_2, the predominant scattering partners in space(107). In this article we report inelastic scattering of O_2 with He. In addition, the splitting of rotational levels of an open shell molecule like O_2 by spin-spin and spin-rotation couplings makes it an interesting target for collision studies. Because O_2 is paramagnetic it can be used in magnetic trapping(21; 126)or Zeeman deceleration(134) experiments, making O_2 a candidate for collision studies at very low translational energy. Several experimental investigations of rotational energy transfer in O_2 due to collision with rare gases have been reported. Luzzatti, et al.(82) reported absolute total elastic cross sections for collision of O_2 with He, Ne, Ar, Kr and Xe. High resolution crossed molecular-beam measurements of the total differential cross sections (DCS) for the scattering of O_2 by helium was performed by Beneventi et al.(17) DCSs with well resolved diffraction oscillations for Ne-O_2 collisional system was measured by Beneventi et al.(16) Faubel et al.(107; 46) performed crossed molecular-beam experiments for Ar-O_2 collisional system and obtained individual rotational state-to state transitions. Collisional excitation of O_2 by small diatomic molecules have been also studied and recently, Chefdeville et al.(38) reported state-to-state integral cross sections (ICSs) in a highly advanced crossed beam experimental study of O_2-H_2 at low energy and observed partial wave resonances that were in very good agreement with the theoretical predictions by some of us. With identical spin-zero nuclei and the electronic ground state symmetry ($X^3\Sigma_g^-$), the quantum number N of molecular rotation in O_2 is restricted to odd values. Spin-rotation coupling also splits the rotational levels. Departure from pure Hund's case (b) is taken into account through an intermediate coupling representation. In Hund's case (b), the total molecular angular momentum j is defined by:

$$j = N + S \tag{6.1}$$

where N and S are the nuclear rotational and the electronic spin angular momenta.

In the intermediate coupling scheme, the rotational wave function can be written as(78):

$$|F_1 j_m\rangle = cos\alpha|N = j - 1, S_{jm}\rangle + sin\alpha|N = j + 1, S_{jm}\rangle \tag{6.2}$$

$$|F_2 j_m\rangle = |N = j, S_{jm}\rangle \tag{6.3}$$

$$|F_3 j_m\rangle = -sin\alpha|N = j - 1, S_{jm}\rangle + cos\alpha|N = j + 1, S_{jm}\rangle \tag{6.4}$$

where $|NS_{jm}\rangle$ denotes pure Hund's case (b) basis functions and the mixing angle α is obtained by diagonalization of the molecular Hamiltonian. In this paper, the labelling convention of Lique(78) where the energy levels are labelled by N, the rotational quantum number and the spectroscopic index F_i is used. The correspondence between Hund's case (b) limit and the present labelling is as follows:

- F_1 corresponds to N=j-1
- F_2 corresponds to N=j
- F_3 corresponds to N=j+1

A rotational energy diagram for ground vibrational state of O_2 is shown in Fig. 6.1 for NF levels up to N=9. For N≤5, the F_3 level has a lower energy than the F_1 level, but after N = 5 this switches.

Note that the N=3 levels are only $\sim$ 4cm^{-1} higher than those of N=1. State-to-state collision studies use supersonic expansions to rotationally cool a molecule to its lowest rotational level. In a study by Chefdeville et al.(38), a special pulsed valve operating at 60 K was used to cool O_2 to its lowest spin-rotation state (N=1, F_3). Single state selection is not possible with the room temperature pulsed valves used in our experiment, but this is somewhat compensated by allowing study of both the F_3 and F_1 levels in this work. The presence of a small fraction of O_2 in the N=3 state can have a strong effect on the measured data, as shown in the experimental part of this paper. Fortunately, accurate theoretical calculations are able to unravel the contribution of single initial states. We report here the experimental determination of state-to-state DCS for inelastic collisions of O_2 and He at collision energy of 660 cm^{-1}.

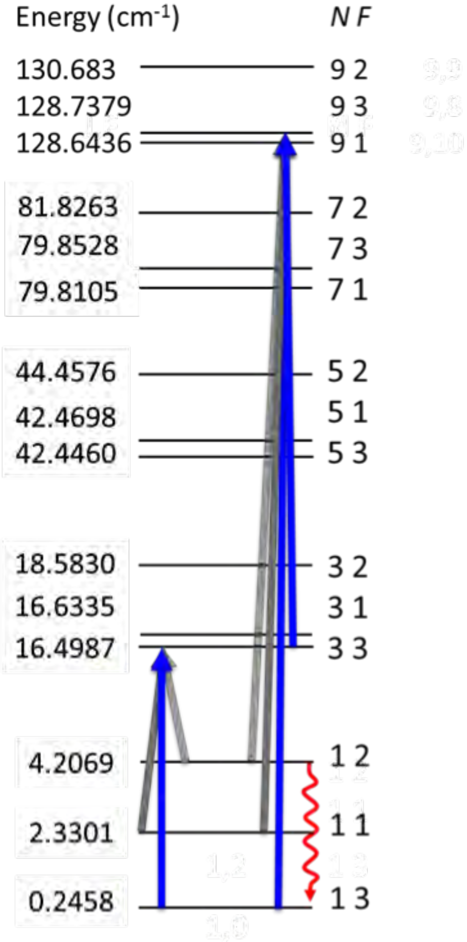

Figure 6.1: Schematic rotational energy level diagram of O_2 showing the fine structure levels and labelling of the quantum numbers N and F. Emission from NF: 12-13, indicated by the wavy line, has been detected in interstellar clouds. Vertical arrows are shown to indicate excitation from different initial states with N=1 and 3 to the NF=91 and NF=33 final states.

6.2 Experimental Methods

Data were collected in a crossed molecular-beam machine with variable beam crossing angle and resonance enhanced multi-photon ionization (REMPI) of the scattered products with velocity map imaging detection(41), as shown schematically in Figure 2.13. Two skimmed supersonic beams, one of neat helium produced from a Nijmegen pulsed valve(137) and the other of 5% O_2 seeded in argon produced from a second (Jordan) pulsed valve were used. The backing pressure for the expansion of both colliding partners was around 2 bars. The pulse duration of the Nijmegen pulsed valve is about 30 μs and the pulse duration of the Jordan valve was 60 μs. The source chamber that houses the secondary beam (He) was differentially pumped and the molecular-beam passes through a skimmer of aperture diameter 2.5 mm positioned 7 cm away from the nozzle. The primary molecular-beam source was mounted in the differentially pumped rotatable chamber positioned 3 cm from the skimmer of aperture diameter 2.5 mm. Rotating the primary beam in the plane of collision can change the angle between the two molecular-beams. For this experiment, the angle between two beams was 900. Turbo molecular pumps evacuated all the chambers. The two molecular-beams and laser were coplanar parallel to the detector and were optimally aligned to ensure the best signal. The collision energy for the O_2-He collisions is 660 cm^{-1}. This is larger than the (540±40)cm^{-1} collision energy expected when using molecular-beam velocities of room temperature O_2 seeded in Ar and He of 640 m/s and 1800 m/s, respectively. The estimated spread in the collision energy was $\pm 40\mathrm{cm}^{-1}$. Warming up of the pulsed valves, which are not sufficiently thermally grounded to the apparatus, probably causes this deviation. Depletion of the O_2 ground state by collision was measured to be less than 10%, which ensured single collision conditions.

The laser and both molecular-beams were operated at 10 Hz. As described in more detail below, 2+1 Resonance Enhanced Multi-Photon Ionization (REMPI) around 225 nm to the $3d\pi(X^3\Sigma^-_{1g})$ v=2 Rydberg state at 11.02 eV was used to excite the molecules by two-photon excitation and then ionize the molecules so that they could be detected using VMI. During image collection the laser frequency was fixed rather than scanning the wavelength over the full width of the Doppler profile of the REMPI transition. However, the laser bandwidth was $\sim 0.1\mathrm{cm}^{-1}$ and the $\sim$ 2 mJ energy per pulse of the laser power broadened the transitions sufficiently that Doppler scanning was unnecessary. These wavelengths were generated by frequency doubling the output of a tunable pulsed dye laser (Scanmate) operating with Coumarin dye using a BBO crystal. The dye laser was pumped by a Nd:YAG laser (Continuum Powerlite) operating at 355 nm and with 10 Hz repetition rate. Typical ultraviolet (UV) laser energies were 2 mJ per pulse with a pulse duration of 7-9 ns. The probe beam was focused with a 20 cm lens onto the intersection region of the molecular-beams. The scattered product was ionized and was extracted by velocity map imaging ion optics lens. After 85 cm free flight along the time of flight tube, the 3-D ion sphere was crushed onto 2-D detector, which is read by CCD camera. Application of gating enables us to select our required mass and filter out the background ions of other mass. Typical images were recorded with 100,000-300,000 laser shots.

6.3 Theory

This paragraph presents the key highlights of the theoretical calculations. The Potential energy surface (PES) from Groenenboom and Struniewicz(54) was used for theoretical calculations. The O_2-He PES was calculated at the partially spin-restricted coupled cluster with the single, double and perturbative triple excitations [RCCSD(T)] level(71). Details of computations are given in Ref.(54; 118; 20) The scattering calculations were carried out for collisional energy E_{col} = 660 cm^{-1}. We have computed the DCS out of N = 1 and N = 3 to N = 1 - 9. The reduced mass of the system μ is 3.557 amu. In the scattering calculations, as we were only interested in pure rotational excitation, the O_2 intermolecular distance was fixed at a value of 2.28 bohr corresponding to the equilibrium distance. In the O_2 $(X^3\Sigma^-_{1g})$ electronic ground state, the rotational levels are split by spin-rotation coupling(91). To take into account this spin-rotation coupling, it was assumed that in the intermediate coupling scheme, the rotational wave functions are linear combination of pure Hund's case (b).

Orlikowski(99) has shown that neglecting the energy splitting can lead to errors of 10-30% in the calculated cross sections. Accordingly, all calculations reported in the present paper(20) were carried out taking into account the exact energy splitting of the levels. The rotational energy levels of the O_2 were computed with the use of the experimental spectroscopic constants of Endo and Mizushima(40). The standard time-independent coupled scattering equations were solved using the MOLSCAT code(62), modified to take into account the fine-structure of the energy levels and the intermediate coupling scheme.

6.4 Results

The population distribution of our cold O_2 beam is estimated from simulation of the 2+1 REMPI spectrum, and confirmed by reconstruction from theory of the measured differential cross sections from individual initial states. State-selective detection of O_2 $(X^3\Sigma^-_{1g})$(v=0,NF) by (2+1) resonance enhanced multi-photon ionization (REMPI) around 225 nm via the $3dp^3\Sigma^-_{1g}(v = 2)$ Rydberg state(139) was employed here. A simulated spectrum for this transition was first constructed using the PGOPHER(133) program and compared with the experimental spectrum for the initial beam (before scattering) in Figure 6.2. Simulations using PGOPHER show that all three F_i levels of $3dp^3\Sigma^-_{1g}(v = 2)$ upper state are present instead of only the F_2 levels predicted in Ref.(139) While the chosen transition is one of the strongest of the $3d\pi$ Rydberg states, it does not allow clean probing of the F_2 final states.

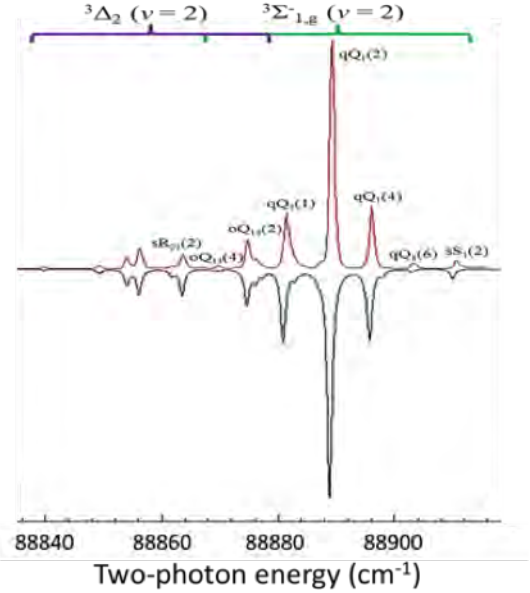

Figure 6.2: Experimental (upper curve) and simulated (lower curve) 2+1 REMPI spectrum of the initial beam of O_2 *via the* $3dp^3\Sigma^-_{1g}(v = 2)$ *and* $^3\Delta_{2,g}(v = 2)$ *Rydberg states. Peaks are labelled* $(\Delta j)_{Fi(Ryd)Fi(ground)(jground)} where F_i = 1$*, 2 or 3, and Ryd signifies the upper Rydberg state and ground is the lower ground electronic state of* O_2*. When* F_i*(Ryd)=Fi(ground) only one* F_i *value is shown. The simulated spectrum is fit by the PGOPHER program for a rotational temperature of* $\sim 11K$*.*

The peak labelled Q2(1) at 88881.2 cm^{-1} in the figure has initial (and final) F_2 states but it is overlapped by transitions from other F_2 levels at higher temperatures. However, most of the possible F_1 (except the lowest, NF=13) and F_3 states can be probed, and theory does not predict any significant deviation in behaviour for the F_2 states. From the simulated spectrum, REMPI line positions were determined for probing a range of rotationally excited (NF) rotational states.

In the temperature fit of the initial beam spectrum (Figure 6.2) it was necessary to adjust the ‘temperature’ of the F manifolds individually. For the shown fit, temperatures of F_1: 11 K, F_2: 3.5 K, and F_3: 10 K were used. Although the fit under this assumption looks encouraging, beam spectrum taken under weaker expansion conditions shows that the peaks for the higher N levels are increasingly weaker than predicted, indicating significant NF-dependent pre-dissociation. By increasing the laser power it is possible to compete with pre-dissociation and observe higher final N states up to N=9. A complete study of pre-dissociation and ion fragmentation when probing the Rydberg manifold is underway in our laboratory. It should be noted that is not possible to obtain reliable relative population information from the simulation, especially for $N \geq 3$.

To determine the inelastic differential cross-sections (DCS), we used the exact Close Coupling approach of Arthurs and Dalgarno(11). All calculations were carried out with the exact energy levels including the fine structure interaction. The quantal coupled equations in the intermediate coupling scheme were solved using the MOLSCAT code(62) modified to take into account the fine structure of the O_2 energy levels. The accurate O_2 -He PES of Groenenboom and Struniewicz(54), computed at the coupled clusters level with large atomic basis set, was used in the calculations. For our calculations, we used the same parameters than Lique(78). The computed scattering matrices were then used for the determination of DCS for collisional energy $E_{col} = 660\ cm^{-1}$ using the formula of Arthurs Dalgarno(11). The DCS are obtained by summing the scattering matrices over a sufficiently large number of values of the total angular momentum **J** until convergence is reached. State-to-state DCS for transitions out of N = 1, 3 states to N = 1 - 9 states were computed.

Raw O_2^+ images for specific final states from the scattering of O_2 with He are shown in Figure 6.3. While in all images the laser polarization direction is in the scattering plane, repeated measurements with perpendicular polarization showed no observable differences, which indicates that the present experiment is not sensitive to collision-induced alignment effects(25; 112).

Raw images were first transformed from density-to-flux using the IMSIM program of McBane(84) and differential cross sections shown in Figure 6.4 were obtained by integrating along the outer edge of the flux-corrected image. Note that for scattering angles less than 30 degrees, the effects of elastic scattering of warm molecules in the parent beam (thus especially for the lower levels) with the same final state N value as that being probed makes background subtraction unreliable. We choose to ignore this region of the DCS. For increasing final state energy, the inelastic scattering changes from forward scattered towards backwards scattering. The results also show that for the same N quantum number, the DCSs are similar. These trends are concordant with the theoretical predictions.(78)

The simulated DCSs in Figure 6.4 are built from theory DCSs of the possible initial rotational states (N=1,3) going to the same final NF rotational state. The individual theoretical DCSs are summed to produce the total theoretical DCSs shown in Figure 6.4. Best agreement with the theoretical DCSs was found for all data when the composition of the initial O_2 molecular-beam population ratio is 80% N=1 with equal F_j populations of F_1=F_2=F_1; and 20% N=3, again with equal F_3, F_2, and F_1 populations, corresponding to a temperature of $\sim 8K$; which is in quite reasonable agreement with the initial fit of 11 K. Note that since no F_2 final states were probed, the DCS fit is less sensitive to the initial F_2 state populations. Analysis of the NF dependent O+/O_2^+ branching ratios and pre-dissociation rates confirms that for the lower NF initial states N=1,3 F=1,3, the relative sensitivities for transitions to the same final state are similar, which validates the summation of theoretical cross sections used

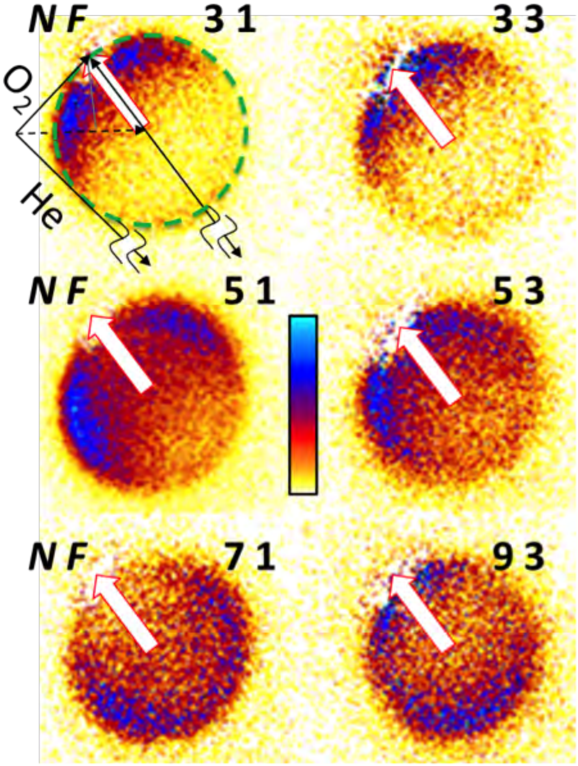

Figure 6.3: Experimental raw O_2^+ images for the inelastic scattering of O_2 with He at 660 cm^{-1} collision energy. A color bar is shown in the middle of the figure for decoding of signal intensity. Superimposed on the NF=31 final state image is a schematic Newton diagram along with a dashed circle indicating the dimension for elastic scattering. White arrows show the direction of the initial relative velocity vector for each image.

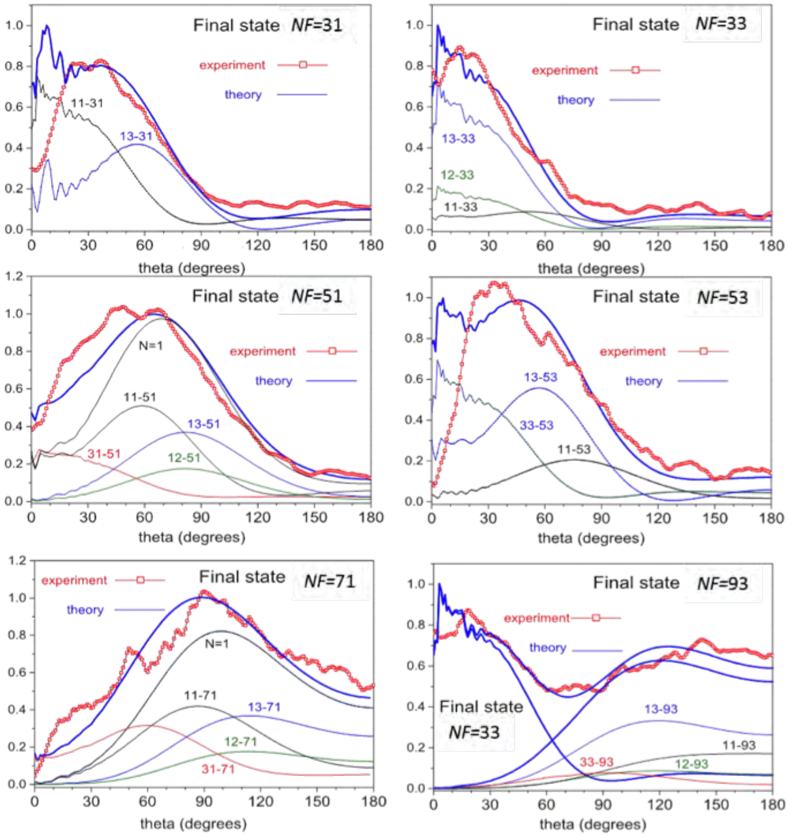

Figure 6.4: Differential cross sections derived from the O_2^+ images shown in Figure 6.3. The red line with boxed symbols represents the experimental DCS while the heavy blue line represents the total theoretical DCSs, which are normalized to unity for better comparison. The composition of the theory DCSs are shown as lighter lines and labelled $NF - N'F'$ where NF is the initial state and $N'F'$ is the final state. For the final state NF=93 two theory curves are shown, one at small scattering angles for the NF=33 final state and at larger angles for the NF=93 final state.

here.
Overlap with (2+1) REMPI lines of the $3d\pi^3\Delta_{2,g}(v=2)$ Rydberg state takes place when using REMPI of the $3d\pi^3\Delta_{2,g}(v=2)$ transition to probe the higher N levels of the F_3 manifold. For the NF=93 final state probed by the Q13($j=8$) band there is overlap with the S_{23}(j=2) band of the $3d\pi^3\Delta_2(v=2)$ state, probing thus the NF=33 final state level. Although both final states are probed, they show quite different DCSs and this allows fitting the low and high NF final state mix, as shown in Figure 6.4. In this case the forward part (low N probed via the $^3\Delta_2$ state) was first fit independently and scaled to blend with the backward scattering (high N, $^3\Delta_{2,g}$ state) part of the image. Rydberg transitions to the $3d\pi^3\Delta_{0,g}(v=2)$ band around 89380 cm^{-1} also give a strong O_2^+ signal and nicely resolved differential cross sections. Further analysis of the spectrum as a function of laser power should eventually allow extraction of (relative) populations from the signal intensity. The $3d\pi^3\Delta_{0,g}(v=2)$ transition needs further population analysis but it does provide relatively strong DCSs and also gives the possibility of measuring higher j-states.

6.5 Summary and Conclusions

In summary, the theoretical predictions of Lique(78) for rotationally inelastic collisions between O_2 and He have been confirmed by measurements of DCSs, which provide the most sensitive test of scattering and potential energy surfaces. The O_2 -He collisional data can now be used with confidence to derive the interstellar O_2 abundance from astronomical observations. The data can also be used for applications in the cold molecules field. We have also demonstrated a (2+1) laser ionization scheme that can be combined with the powerful velocity map imaging technique to yield high quality information for a wide variety of dynamical processes involving the all-important O_2 molecule. For example, we are presently investigating scattering of O_2 at ice surfaces and detection of nascent O_2 as a photodissociation product using this approach. Lower rotational levels are detected in this work but on-going studies of laser ionization in O_2 should allow procedures for attaining quantitative population information on higher rotational and ro-vibrational states.

Appendix A

Imaging ion molecule reactions

A.1 Ion molecule reactions

Ion molecule gas phase chemical processes occur in our environment, in planetary atmospheres, in interstellar medium and in the outer shells of atmosphere of stars and gas planets.(47) Ion molecule reactions are one of the key chemical processes in the interstellar medium for the evolution of astronomical objects. Ion molecule reaction are of great importance to astrochemists or astrophysicists for their endeavor to understand the life cycle of molecules in the galaxy. The long range interaction of ions with neutral atoms or molecules leads to large scattering cross sections for inelastic and reactive process. Reaction dynamics of ion molecule reactions in the gas phase is very interesting, particularly the dependence on which initial quantum states of the reactant lead to different quantum states of the products.(88) The application of velocity map imaging to ion molecule gas phase reaction has enabled a wealth of information, for example,(131) the group of Wester has shown new and unexpected reaction mechanisms. (90; 113; 121) $Ar^+ + N_2$ charge transfer reaction is studied extensively in Ref(34; 48). The group of Farrar studied charge-transfer reactive scattering for $C^+ + NH_3$ and $N^+ + CH_4$ at a collision energy of a few electronvolts using velocity map imaging measurements.(103; 104)

The first motivation of our experiment was to observe reactive scattering signal using ion molecule scattering. We chose the known system of $Ar^+ + N_2 \rightarrow N_2^+ + Ar$ which was very well studied in the group of Wester(89; 121). We have studied cation-molecule reaction using velocity map imaging in crossed beam experimental setup, for the charge transfer reaction of $Ar^+ + N_2$, $Ar^+ + O_2$. Ion molecule reactions are attractive for imaging experiments in that the signal should be large, no (expensive) lasers are needed, and the reaction product is at a different mass than the ionic reactant. However, the velocity spread of the ion beam is very poor compared to supersonic neutral beams; space charge limitations affect the intensity of the ion beam, and the ion beam size is much larger than a typical laser-ionized volume. These problems greatly limit the image resolution, as seen in the publications listed above.

A.2 Experimental Setup for Ion-molecule reaction

A mini cross beam experimental setup was used. A schematic of the mini apparatus is shown in Figure A.1. The mini crossed beam experiment set up consists of one compact low energy pulsed ion source and a Nijmegen pulsed valve as the supersonic neutral beam source, a pulsed velocity map imaging spectrometer and a pulsed micro channel plate detector with CCD camera. The whole ion source is housed in a cylindrical vacuum chamber of 65 mm outer diameter reaching into the scattering chamber. The ion source was pumped by a 70 l/s turbomolecular pump maintaining a pressure around 1 x 10^{-4} mbar at a pulse length of 70 μs and a repetition rate of 10 Hz. Depending on the extraction voltage applied this compact ion source can make positively and negatively charged ions. Low energy ions were produced by electron impact in a pulsed supersonic beam coming out from a piezo electric valve with nozzle diameter of 0.2 mm. A custom made hot cathode electron source was mounted near the exiting pulsed molecular beam. The hot cathode electron source consists of filament. The generated heat load due to hot cathode electron source was removed by a cold finger reaching into vacuum in order to avoid damage of the piezo valve. The front side of the piezo electric valve, nozzle, a cylindrical electrode and the electron gun forms the ion terminal. The terminal was kept at a potential relative to the potential of the interaction region. The electrode of the imaging spectrometer and the endcaps of the beam chambers were biased by using same voltage as used for the terminal. The kinetic energies of the ions produced depends on the relative terminal potential. The conventional velocity map imaging spectrometer was not sufficient for studying ion molecule reaction for several reasons. First, there is no laser ionization to provide a t=0 for the time of flight. Second, the collision zone must be field free in order not to affect the reactant ion beam. The collision volume is quite large, as defined by the ion beam size. For these reasons we defined the starting point by the time when we pulsed on the repeller and extractor after the ion beam has entered the collision zone, and extra lenses were used in the VMI region to allow good mapping with larger ionization volumes. For more spatial information a modified version of the velocity map spectrometer was used. The larger Newton sphere together with a pulsed extraction was key for ion molecule reaction imaging. The pulsed extraction was done by home built fast switches. Timings of the valve, detector, ion imaging spectrometer was synchronized for the optimum signal.

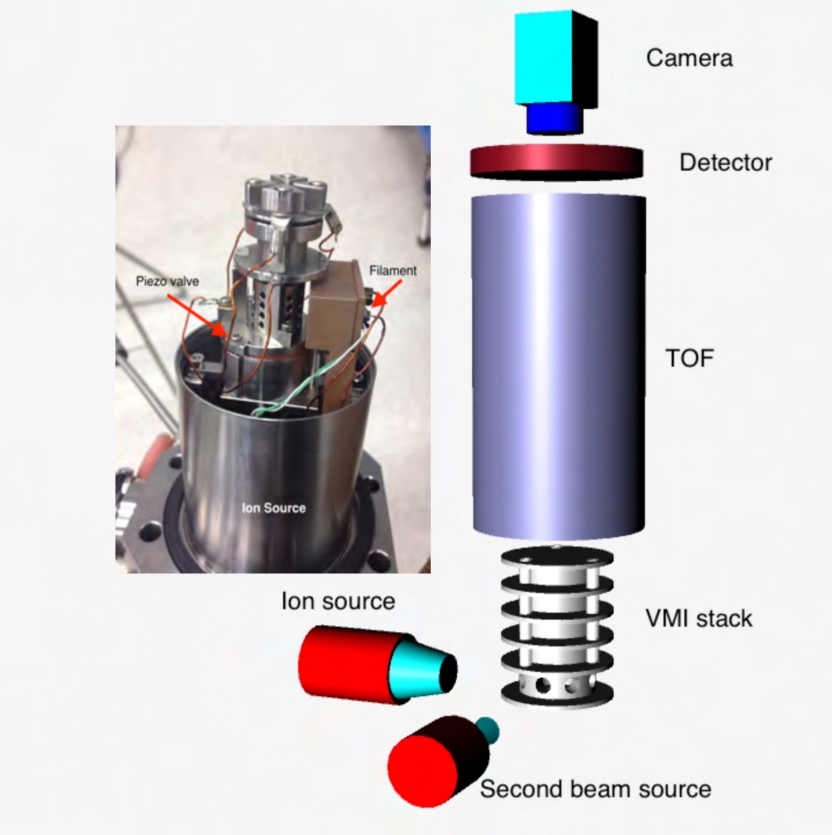

Figure A.1: Ion-molecule reaction experimental setup at Nijmegen. The compact ion source is from the group of Wester and adopted to the mini crossed beam apparatus. Ions are produced by electron impact on a pulsed molecular beam created by a piezo electric valve. The secondary pulsed molecular beam is created by a Nijmegen Pulsed Valve.

A.3 Results & Outlook

We observed a very strong reactive scattering signal for $Ar^+ + N_2$ reaction. A low collision energy signal for $Ar^+ + N_2$ was also measured. The ion molecule reaction was repeated for $Ar^+ + O_2 \rightarrow O_2^+ + Ar$. Figure A.2 shows reactive scattering signal for two systems, $Ar^+ + N_2 \rightarrow N_2^+ + Ar$ and $Ar^+ + O_2 \rightarrow O_2^+ + Ar$. The strong reactant ion beam signal leaks through the mass gate and is seen in our product mass image. No extra structure is seen in the images that would indicate vibrational resolution. More analysis needs to be done for the observed scattering signal in order to fully understand the dynamics of the reactive scattering signal. The strong signal of ion molecule reaction is encouraging and once we can make significant improvements in the ion source temperature and velocity spread we will carry on further studies.

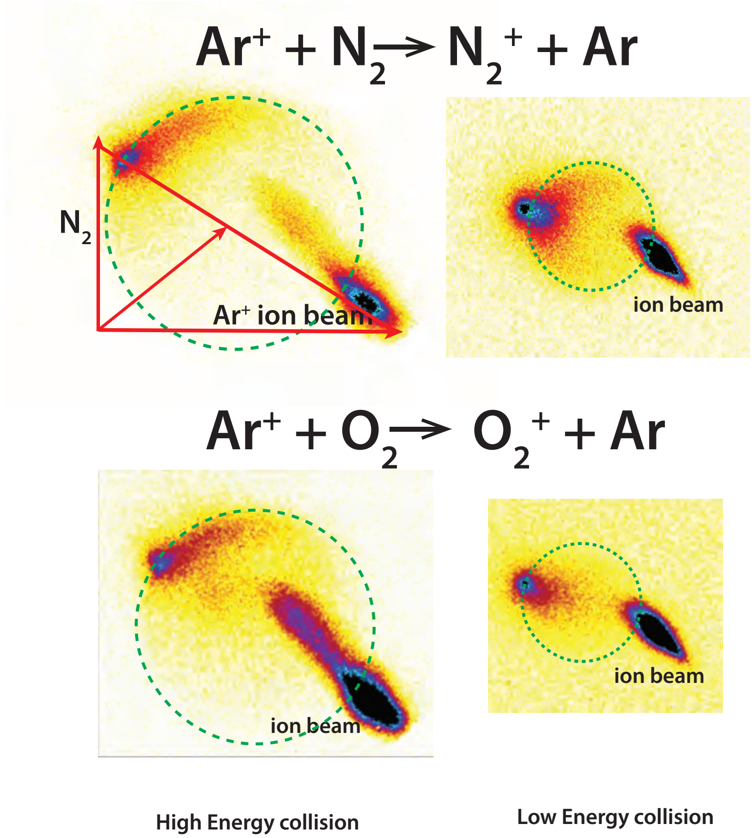

Figure A.2: The Figure shows Ion-molecule reaction for two systems $Ar^+ + N_2 \rightarrow N_2^+ + Ar$ *and* $Ar^+ + O_2 \rightarrow O_2^+ + Ar$. *The left hand panel of both system shows reactive scattering signal at high collision energy while the right hand panel shows the low collision energy. The Newton diagram shown for* $Ar^+ + N_2 \rightarrow N_2^+ + Ar$ *system is just a representation of two beam direction and not scaled to energy. There is a strong ion beam signal in each image.*

Bibliography

[1] Alma observatory.

[2] https://nssdc.gsfc.nasa.gov/astro/astrolist.html.

[3] Nobel prize in chemistry 1986.

[4] *Annual Review of Astronomy and Astrophysics*, 44(1):367–414, 2006.

[5] Millard H Alexander. *The Journal of Chemical Physics*, 67(6):2703–2712, 1977.

[6] Millard H Alexander. *Faraday Discussions*, 113:437–454, 1999.

[7] Millard H Alexander and Paul J Dagdigian. *The Journal of Chemical Physics*, 79(1):302–310, 1983.

[8] Stiliana Antonova, Ao Lin, Antonis P Tsakotellis, and George C McBane. *The Journal of chemical physics*, 110(5):2384–2390, 1999.

[9] Stiliana Antonova, Ao Lin, Antonis P Tsakotellis, and George C McBane. *The Journal of Chemical Physics*, 110(24):11742–11748, 1999.

[10] F. J. Aoiz, V. J. Herrero, V. Saez Rabanos, and J. E. Verdasco. *Physical Chemistry Chemical Physics*, 6(18):4407–4415, 2004.

[11] AM Arthurs and A Dalgarno. The mobilities of ions in molecular gases. In *Proceedings of the Royal Society of London A: Mathematical, Physical and Engineering Sciences*, volume 256, pages 552–558. The Royal Society, 1960.

[12] AM Arthurs and A Dalgarno. The theory of scattering by a rigid rotator. In *Proceedings of the Royal Society of London A: Mathematical, Physical and Engineering Sciences*, volume 256, pages 540–551. The Royal Society, 1960.

[13] B. Larson, eau, R. Li, Pagani, L., Bergman, P., Bernath, P., Biver, N., Black, J. H., Booth, R. S., Buat, V., ier, J. Crovi, Curry, C. L., Dahlgren, M., Encrenaz, P. J., Falgarone, E., Feldman, P. A., Fich, M., Florén, H. G., Fredrixon, M., k, U. Fri, Gahm, G. F., Gerin, M., tröm, M. Hag, Harju, J., egawa, T. Ha, on, Å. Hjalmar, on, L. E. B. Johan, ttanont, K. Ju, Klotz, A., Kyrölä, E., Kwok, S., Lecacheux, A., tröm, T. Lilje, Llewellyn, E. J., Lundin, S., Mégie, G., Mitchell, G. F., Murtagh, D., Nordh, L. H., Nyman, L.-Å., Olberg, M., on, A. O. H. Olof, on, G. Olof, on, H. Olof, on, G. Per, Plume, R., Rickman, H., torcelli, I. Ri, Rydbeck, G., t, A. A. Sandqvi, Schéele, F. V., Serra, G., ky, S. Torchin, Tothill, N. F., Volk, K., Wiklind, T., on, C. D. Wil, Winnberg, A., and Witt, G. *AA*, 3(999-1003), 2007.

[14] J Baker, JL Lemaire, S Couris, A Vient, D Malmasson, and F Rostas. *Chemical physics*, 178(1-3):569–579, 1993.

[15] Gabriel G Balint-Kurti and Oleg S Vasyutinskii. *The Journal of Physical Chemistry A*, 113(52):14281–14290, 2009.

[16] L Beneventi, P Casavecchia, F Pirani, F Vecchiocattivi, GG Volpi, G Brocks, A Van der Avoird, B Heijmen, and J Reuss. *The Journal of chemical physics*, 95(1):195–204, 1991.

[17] Laura Beneventi, Piergiorgio Casavecchia, and Gian Gualberto Volpi. *The Journal of chemical physics*, 85(12):7011–7029, 1986.

[18] R.B. Bernstein, D.R. Herschbach, and R.D. Levine. *J. Phys. Chem.*, 91:5365–5377, 1987. Dynamical stereochemistry issue.

[19] Andre Bieler, Kathrin Altwegg, Hans Balsiger, Akiva Bar-Nun, J-J Berthelier, Peter Bochsler, Christelle Briois, Ursina Calmonte, M Combi, J De Keyser, et al. *Nature*, 526(7575):678–681, 2015.

[20] Chandan Kumar Bishwakarma, George van Oevelen, Roy Scheidsbach, David H Parker, Yulia Kalugina, and François Lique. *The Journal of Physical Chemistry A*, 120(6):868–874, 2016.

[21] John L Bohn. *Physical Review A*, 62(3):032701, 2000.

[22] LS Bontuyan, AG Suits, PL Houston, and BJ Whitaker. *The Journal of Physical Chemistry*, 97(24):6342–6350, 1993.

[23] Robert W Boyd. *Nonlinear optics.* Taylor & Francis, 2003.

[24] M Brouard, H Chadwick, CJ Eyles, FJ Aoiz, and J Kłos. *The Journal of Chemical Physics*, 135(8):084305, 2011.

[25] M Brouard, H Chadwick, CJ Eyles, B Hornung, B Nichols, FJ Aoiz, PG Jambrina, and S Stolte. *The Journal of Chemical Physics*, 138(10):104310, 2013.

[26] M Brouard, H Chadwick, CJ Eyles, B Hornung, B Nichols, FJ Aoiz, PG Jambrina, S Stolte, and MP De Miranda. *The Journal of Chemical Physics*, 138(10):104309, 2013.

[27] M Brouard, H Chadwick, CJ Eyles, B Hornung, B Nichols, JM Scott, FJ Aoiz, J Kłos, S Stolte, and X Zhang. *Molecular Physics*, 111(12-13):1759–1771, 2013.

[28] M Brouard, H Chadwick, SDS Gordon, B Hornung, B Nichols, FJ Aoiz, and S Stolte. *The Journal of Physical Chemistry A*, 119(50):12404–12416, 2015.

[29] M Brouard, H Chadwick, SDS Gordon, B Hornung, B Nichols, FJ Aoiz, and S Stolte. *The Journal of chemical physics*, 144(22):224301, 2016.

[30] M Brouard, H Chadwick, SDS Gordon, B Hornung, B Nichols, J Kłos, FJ Aoiz, and S Stolte. *The Journal of chemical physics*, 141(16):164306, 2014.

[31] M Brouard, B Hornung, and FJ Aoiz. *Physical review letters*, 111(18):183202, 2013.

[32] Mark Brouard and Claire *Tutorials in molecular reaction dynamics.* Royal Society of Chemistry, 2010.

[33] HP Butz, R Feltgen, H Pauly, and H v Vehmeyer. *Zeitschrift für Physik A Hadrons and nuclei*, 247(1):70–83, 1971.

[34] R Candori, S Cavalli, F Pirani, A Volpi, D Cappelletti, P Tosi, and D Bassi. *The Journal of Chemical Physics*, 115(19):8888–8898, 2001.

[35] Helen Chadwick, Bethan Nichols, Sean DS Gordon, Balazs Hornung, Eleanor Squires, Mark Brouard, Jacek Kłos, Millard H Alexander, F Javier Aoiz, and Steven Stolte. *The journal of physical chemistry letters*, 5(19):3296–3301, 2014.

[36] David W Chandler and Paul L Houston. *The Journal of chemical physics*, 87(2):1445–1447 0021–9606, 1987.

[37] D.W. Chandler and P.L. Houston. *J.Chem.Phys.*, 87:1445, 1987.

[38] Simon Chefdeville, Yulia Kalugina, Sebastiaan YT van de Meerakker, Christian Naulin, François Lique, and Michel Costes. *Science*, 341(6150):1094–1096, 2013.

[39] Joseph I Cline, K Thomas Lorenz, Elisabeth A Wade, James W Barr, and David W Chandler. *Journal of Chemical Physics*, 115(14):6277–6280, 2001.

[40] Yasuki Endo and Masataka Mizushima. *Japanese Journal of Applied Physics*, 21(6A):L379, 1982.

[41] André TJB Eppink and David H Parker. *Review of Scientific Instruments*, 68(9):3477–3484, 1997.

[42] Uzi Even, J Jortner, D Noy, N Lavie, and C Cossart-Magos. *The Journal of Chemical Physics*, 112(18):8068–8071, 2000.

[43] CJ Eyles, M Brouard, C-H Yang, J Kłos, FJ Aoiz, A Gijsbertsen, AE Wiskerke, and S Stolte. *Nature chemistry*, 3(8):597–602, 2011.

[44] U. Fano and J.H. Macek. *Rev.Mod.Phys.*, 45:553, 1973.

[45] U Fano and Joseph H Macek. *Reviews of Modern Physics*, 45(4):553, 1973.

[46] M Faubel and G Kraft. *The Journal of chemical physics*, 85(5):2671–2683, 1986.

[47] Eldon E Ferguson. *Reviews of Geophysics*, 5(3):305–327, 1967.

[48] Jean H Futrell. *Advances in Chemical Physics: State-Selected and State-To-State Ion-Molecule Reaction Dynamics, Part 1. Experiment, Volume 82*, pages 501–552, 1992.

[49] RD Gehrz, TL Roellig, MW Werner, GG Fazio, JR Houck, FJ Low, George H Rieke, BT Soifer, DA Levine, and EA Romana. *Review of scientific instruments*, 78(1):011302, 2007.

[50] W Ronald Gentry and Clayton F Giese. *Review of Scientific instruments*, 49(5):595–600, 1978.

[51] Joop J Gilijamse, Steven Hoekstra, Sebastiaan YT van de Meerakker, Gerrit C Groenenboom, and Gerard Meijer. *Science*, 313(5793):1617–1620, 2006.

[52] Paul F Goldsmith, René Liseau, Tom A Bell, John H Black, Jo-Hsin Chen, David Hollenbach, Michael J Kaufman, Di Li, Dariusz C Lis, Gary Melnick, et al. *The Astrophysical Journal*, 737(2):96, 2011.

[53] González-Alfonso, E., Wright, C. M., Cernicharo, J., Rosenthal, D., Boonman, A. M. S., and van Dishoeck, E. F. *AA*, 386(3):1074–1102, 2002.

[54] Gerrit C Groenenboom and Izabela M Struniewicz. *The Journal of Chemical Physics*, 113(21):9562–9566, 2000.

[55] G.E. Hall and P.L. Houston. *Annu. Rev. Phys. Chem.*, 40:375–405, 1989.

[56] G.E. Hall, N. Sivakumar, P.L. Houston, and I. Burak. *PRL*, 56:1671–1674, 1986.

[57] Tino GA Heijmen, Robert Moszynski, Paul ES Wormer, and Ad van der Avoird. *The Journal of chemical physics*, 107(23):9921–9928, 1997.

[58] IV Hertel and W Stoll. *Advances in Atomic and Molecular Physics*, 13:113–228, 1978.

[59] R Hilbig and R Wallenstein. *IEEE Journal of Quantum Electronics*, 19(2):194–201, 1983.

[60] Melissa A Hines, Hope A Michelsen, and Richard N Zare. *The Journal of Chemical Physics*, 93(12):8557–8564, 1990.

[61] DK Hoffman, JW Evans, and DJ Kouri. *The Journal of chemical physics*, 80(1):144–148, 1984.

[62] JM Hutson and S Green. *Daresbury Laboratory, UK*, 1994.

[63] Daniel Irimia, Dimitar Dobrikov, Rob Kortekaas, Han Voet, Daan A van den Ende, Wilhelm A Groen, and Maurice HM Janssen. *Review of Scientific Instruments*, 80(11):113303, 2009.

[64] Pablo G. Jambrina, Jacek Klos, F. Javier Aoiz, and Marcelo P. de Miranda. *Physical Chemistry Chemical Physics*, 14(28):9826–9837, 2012.

[65] Jeffrey J Kay, Jeffrey D Steill, Jacek Kłos, Grant Paterson, Matthew L Costen, Kevin E

Strecker, Kenneth G McKendrick, MH Alexander, and David W Chandler. *Molecular Physics*, 110(15-16):1693–1703, 2012.

[66] V Khare, DJ Kouri, and DK Hoffman. *The Journal of Chemical Physics*, 74(4):2275–2286, 1981.

[67] V Khare, DJ Kouri, and DK Hoffman. *The Journal of Chemical Physics*, 76(9):4493–4501, 1982.

[68] Y Kim and H Meyer. *Chemical physics*, 301(2):273–281, 2004.

[69] Moritz Kirste, Xingan Wang, H Christian Schewe, Gerard Meijer, Kopin Liu, Ad van der Avoird, Liesbeth MC Janssen, Koos B Gubbels, Gerrit C Groenenboom, and Sebastiaan YT van de Meerakker. *Science*, 338(6110):1060–1063, 2012.

[70] Ayelet Klein, Yuval Shagam, Wojciech Skomorowski, Piotr S Żuchowski, Mariusz Pawlak, Liesbeth MC Janssen, Nimrod Moiseyev, Sebastiaan YT van de Meerakker, Ad van der Avoird, Christiane P Koch, et al. *Nature Physics*, 2016.

[71] Peter J Knowles, Claudia Hampel, and Hans-Joachim Werner. *The Journal of chemical physics*, 99(7):5219–5227, 1993.

[72] Bengt Larsson, René Liseau, Laurent Pagani, Per Bergman, Peter Bernath, Nicolas Biver, JH Black, RS Booth, Veronique Buat, and Jacques Crovisier. *Astronomy Astrophysics*, 466(3):999–1003

[73] Yuan Tseh Lee. *Science*, 236(4803):793–798, 1987.

[74] Mikhail Lemeshko and Bretislav Friedrich. *Physical Review A*, 79(1):012718–, 01 2009.

[75] Robert J LeRoy, Carey Bissonnette, Thomas H Wu, Ashok K Dham, and William J Meath. *Faraday Discussions*, 97:81–94, 1994.

[76] Raphael D Levine. *Molecular reaction dynamics*. Cambridge University Press, 2009.

[77] RD Levine. *RB Bernstein Molecular reaction dynamics*. 1974.

[78] François Lique. *The Journal of chemical physics*, 132(4):044311, 2010.

[79] R Ogorzalek Loo, WJ Marinelli, PL Houston, S Arepalli, JR Wiesenfeld, and RW Field. *The Journal of chemical physics*, 91(9):5185–5200, 1989.

[80] K Thomas Lorenz, David W Chandler, James W Barr, Wenwu Chen, George L Barnes, and Joseph I Cline. *Science*, 293(5537):2063–2066, 2001.

[81] K Thomas Lorenz, David W Chandler, and George C McBane. *The Journal of Physical Chemistry A*, 106(7):1144–1151, 2002.

[82] E Luzzatti, F Pirani, and F Vecchiocattivi. *Molecular Physics*, 34(5):1279–1286, 1977.

[83] Howard R Mayne and Mark Keil. *The Journal of Physical Chemistry*, 88(5):883–891, 1984.

[84] George C McBane. Simulation and analysis of image data from crossed beam experiments. ACS Publications, 2001.

[85] George C McBane and Slawomir M Cybulski. *The Journal of chemical physics*, 110(24):11734–11741, 1999.

[86] JM Mestdagh, JP Visticot, P Meynadier, O Sublemontier, and AG Suits. *J. Chem. Soc., Faraday Trans.*, 89(10):1413–1418, 1993.

[87] Henning Meyer. *The Journal of Physical Chemistry*, 99(4):1101–1114, 1995.

[88] Jennifer Meyer and Roland Wester. *Annual Review of Physical Chemistry*, 68:333–353, 2017.

[89] J Mikosch, U Frühling, S Trippel, D Schwalm, M Weidemüller, and R Wester. *Physical Chemistry Chemical Physics*, 8(25):2990–2999, 2006.

[90] J Mikosch, S Trippel, C Eichhorn, R Otto, U Lourderaj, JX Zhang, WL Hase, M Weidemüller, and R Wester. *Science*, 319(5860):183–186, 2008.

[91] Masataka Mizushima et al. *Theory of rotating diatomic molecules*. Wiley, 1975.

[92] Yuxiang Mo and Toshinori Suzuki. *The Journal of chemical physics*, 109(11):4691–4692, 1998.

[93] Robert Moszynski, Tatiana Korona, Paul ES Wormer, and Ad van der Avoird. *The Journal of Physical Chemistry A*, 101(26):4690–4698, 1997.

[94] RB Nerf and MA Sonnenberg. *Journal of Molecular Spectroscopy*, 58(3):474–478, 1975.

[95] B Nichols, H Chadwick, SDS Gordon, CJ Eyles, B Hornung, M Brouard, MH Alexander, FJ Aoiz, A Gijsbertsen, and S Stolte. *Chemical Science*, 6(4):2202–2210, 2015.

[96] ML Niu, EJ Salumbides, D Zhao, N De Oliveira, D Joyeux, L Nahon, RW Field, and W Ubachs. *Molecular Physics*, 111(14-15):2163–2174, 2013.

[97] Keith S Noll, TR Geballe, and Mark S Marley. *The Astrophysical Journal Letters*, 489(1):L87, 1997.

[98] Jolijn Onvlee, Sean DS Gordon, Sjoerd N Vogels, Thomas Auth, Tijs Karman, Bethan Nichols, Ad van der Avoird, Gerrit C Groenenboom, Mark Brouard, and Sebastiaan YT van de Meerakker. *Nature Chemistry*, 2016.

[99] Tadeusz Orlikowski. *Molecular Physics*, 56(1):35–46, 1985.

[100] A.J. Orr-Ewing and R.N. Zare. *Annu. Rev. Phys. Chem.*, 45:315–365, 1994.

[101] David H Parker. *Accounts of chemical research*, 33(8):563–571, 2000.

[102] D.H. Parker and A.T.J.B. Eppink. *J. Chem. Phys.*, 107:2357–2362, 1997.

[103] Linsen Pei and James M Farrar. *The Journal of chemical physics*, 136(20):204305, 2012.

[104] Linsen Pei and James M Farrar. *The Journal of Chemical Physics*, 137(15):154312, 2012.

[105] Kirk A Peterson and George C McBane. *The Journal of chemical physics*, 123(8):084314, 2005.

[106] David Pullman, Bretislav Friedrich, Dudley Herschbach, et al. *Journal of Physical Chemistry*, 99:7407–7407, 1995.

[107] Evelyne Roueff and François Lique. *Chemical reviews*, 113(12):8906–8938, 2013.

[108] Andrew M Smith and Theodore P Stecher. *The Astrophysical Journal*, 164:L43

[109] Tony C Smith, David A Hostutler, Gordon D Hager, Michael C Heaven, and George C McBane. *The Journal of chemical physics*, 120(5):2285–2295, 2004.

[110] Verne V Smith, Takashi Tsuji, Kenneth H Hinkle, Katia Cunha, Robert D Blum, Jeff A Valenti, Stephen T Ridgway, Richard R Joyce, and Peter Bernath. *The Astrophysical Journal Letters*, 599(2):L107, 2003.

[111] Philip Solomon, Keith B Jefferts, Arno A Penzias, and Robert W Wilson. *The Astrophysical Journal*, 163:L53

[112] Lei Song, Gerrit C Groenenboom, Ad van der Avoird, Chandan Kumar Bishwakarma, Gautam Sarma, David H Parker, and Arthur G Suits. *The Journal of Physical Chemistry A*, 119(50):12526–12537, 2015.

[113] Martin Stei, Eduardo Carrascosa, Martin A Kainz, Aditya H Kelkar, Jennifer Meyer, István Szabó, Gábor Czakó, and Roland Wester. *Nature chemistry*, 8(2):151, 2016.

[114] Jeffrey D Steill, Jeffrey J Kay, Grant Paterson, Thomas R Sharples, Jacek Kłos, Matthew L Costen, Kevin E Strecker, Kenneth G McKendrick, MH Alexander, and David W Chandler. *The Journal of Physical Chemistry A*, 117(34):8163–8174, 2013.

[115] AG Suits, LS Bontuyan, PL Houston, and BJ Whitaker. *The Journal of chemical physics*, 96(11):8618–8620, 1992.

[116] Arthur G Suits, Chandan Kumar Bishwakarma, Lei Song, Gerrit C Groenenboom, Ad van der Avoird, and David H Parker. *The Journal of Physical Chemistry A*, 119(23):5925–5931 1089–5639, 2014.

[117] ZF Sun, AD von Zastrow, and DH Parker. *The Journal of Chemical Physics*, 147(1):013909, 2017.

[118] Fu-Ming Tao and Yuh-Kang Pan. *The Journal of chemical physics*, 97(7):4989–4995, 1992.

[119] Ondřej Tkáč, Qianli Ma, , Martin Stei, Andrew J Orr-Ewing, and Paul J Dagdigian. *The Journal of chemical physics*, 142(1):014306, 2015.

[120] Ondřej Tkáč, Ashim K Saha, Jérôme Loreau, Qianli Ma, Paul J Dagdigian, David H Parker, Ad van der Avoird, and Andrew J Orr-Ewing. *Molecular Physics*, 113(24):3925–3933, 2015.

[121] S Trippel, M Stei, JA Cox, and R Wester. *Physical review letters*, 110(16):163201, 2013.

[122] Andreas Tunnermann, Carsten Momma, Kasem Mossavi, Caroline Windolph, and B Welleghausen. *Quantum Electronics, IEEE Journal of*, 29(4):1233–1238, 1993.

[123] Sebastiaan YT Van De Meerakker, Hendrick L Bethlem, and Gerard Meijer. *Nature Physics*, 4(8):595–602, 2008.

[124] Sjoerd N Vogels, Jolijn Onvlee, Simon Chefdeville, Ad van der Avoird, Gerrit C Groenenboom, and Sebastiaan YT van de Meerakker. *Science*, 350(6262):787–790, 2015.

[125] Sjoerd N Vogels, Jolijn Onvlee, Alexander von Zastrow, Gerrit C Groenenboom, Ad van der Avoird, and Sebastiaan YT van de Meerakker. *Physical review letters*, 113(26):263202, 2014.

[126] Alessandro Volpi and John L Bohn. *The Journal of chemical physics*, 119(2):866–871, 2003.

[127] Alexander Von Zastrow, Jolijn Onvlee, Sjoerd N Vogels, Gerrit C Groenenboom, Ad Van Der Avoird, and Sebastiaan YT Van De Meerakker. *Nature chemistry*, 6(3):216–221

[128] Alexander von Zastrow, Jolijn Onvlee, Sjoerd N Vogels, Gerrit C Groenenboom, Ad van der Avoird, and Sebastiaan YT van de Meerakker. *Nature chemistry*, 2014.

[129] Elisabeth A Wade, K Thomas Lorenz, David W Chandler, James W Barr, George L Barnes, and Joseph I Cline. *Chemical physics*, 301(2):261–272, 2004.

[130] Elisabeth A. Wade, K. Thomas Lorenz, David W. Chandler, James W. Barr, George L. Barnes, and Joseph I. Cline. *Chemical Physics*, 301(2–3):261–272, 6 2004.

[131] Roland Wester. *Physical Chemistry Chemical Physics*, 16(2):396–405, 2014.

[132] CM Western. *University of Bristol Research Data Repository*, 10, 2014.

[133] Colin M Western. *Journal of Quantitative Spectroscopy and Radiative Transfer*, 186:221–242, 2017.

[134] Alex W Wiederkehr, Hansjürg Schmutz, Michael Motsch, and Frédéric Merkt. *Molecular Physics*, 110(15-16):1807–1814, 2012.

[135] RW Wilson, KB Jefferts, and AA Penzias. *The Astrophysical Journal*, 161:L43

[136] Shiou-Min Wu, Xueming Yang, and David H Parker. *Molecular Physics*, 103(13):1797–1807, 2005.

[137] B. Yan, P. F. H. Claus, B. G. M. van Oorschot, L. Gerritsen, A. T. J. B. Eppink, S. Y. T. van de Meerakker, and D. H. Parker. *Review of Scientific Instruments*, 84(2):–, 2013.

[138] C-H Yang, G Sarma, DH Parker, JJ Ter Meulen, and L Wiesenfeld. *The Journal of chemical physics*, 134(20):204308, 2011.

[139] Robert J Yokelson, RJ Lipert, and WA Chupka. *The Journal of chemical physics*, 97(9):6153–6167, 1992.

Summary

This thesis describes experimental work on inelastic scattering of CO and O_2 with rare gases. There are four major components: the first part explains the astrophysical importance of CO and O_2. The second part shows the experimental techniques including the application of velocity map imaging, VUV light production and their usage for detecting collision induced alignment moments. The third part highlights a novel direct extraction technique for determining collision induced alignment moments for inelastic scattering studies. We used this method for the CO-He CO-Ar systems. The fourth part showcases the study of inelastic scattering of O_2 with He.

First part: Carbon monoxide (CO) is the most abundant C-bearing molecule in the universe. CO is one of the major constituents in the formation of methanol, which is often described as the building block of the universe. Due to the presence of a dipole moment, it also acts as a tracer for the interstellar medium; hence it is important in astrophysics and astrochemistry. Molecular oxygen (O_2) is the most important molecule in our daily life. It protects us from harmful UV light coming from the solar spectrum. As a homonuclear molecule, it is very difficult to detect by optical methods. The recent detection of O_2 in comet tails by mass spectrometers on the Rosetta mission has attracted the interest of many scientists, and especially for those who are searching for life outside mother Earth. DCSs obtained from our experiments provide a stringent test of potential energy surfaces calculated by theory. Accurate potential energy surfaces are key to building accurate astrophysical models. Therefore, inelastic scattering studies of CO and O_2 help us test models for interpreting astrophysical data.

Second part: For our studies we performed crossed-molecular beam experiments to probe rotational excitation of CO and O_2 due scattering with Ar and Helium. Velocity map imaging (VMI) was combined with state-selective detection by (2+1) & $(1 + 1^{'} + 1^{''})$ resonance enhanced multi-photon ionization (REMPI) using vacuum ultraviolet (VUV) as the laser light source. Differential cross sections were extracted from the experimental image after density-to-flux corrections. The measured DCSs were compared with DCSs obtained from theoretical calculations. We have placed the emphasis on angle-resolved measurement of collision-induced alignment and show that our VUV laser probe is particularly sensitive to alignment effects. In this work, tunable VUV radiation around 150 to 154 nm was produced by resonant four-wave difference frequency mixing in Xenon gas. The scattered product was probed with horizontal and vertical VUV probe laser polarization.

Third Part: This part presents a novel means of analyzing velocity map images probing angular momentum polarization in inelastic scattering. Without using any fitting or basis-set functions, alignment moments can be directly extracted from the linear combination of angular distributions obtained with the laser polarization parallel and perpendicular to the scattering plane. Chapter 4 & 5 of the thesis presents imaging studies of CO with Argon and Helium. Rotationally excited CO molecule was detected with state selective detection by a $(1+1^{'}+1^{''})$ REMPI scheme. The DCSs obtained from different polarizations of light is termed a polarization dependent DCS or PDDCS. The detected scattered images show a remarkable difference in appearance which manifests strong collision induced alignment. Like the CO-Ar system, CO-He also shows strong collision induced alignment effects. We used the direct extraction method in order to calculate alignment moments from PDDCSs for both rare gases.

Fourth Part: This part showcases the state-to-state inelastic scattering of O_2 with Helium at collision energy 660 cm^{-1}. Velocity map imaging was combined with state selective detection of O_2 using a (polarization insensitive) 2+1 REMPI process. The obtained raw images were corrected from density-to-flux and the differential cross-section were then extracted for six different O_2 final states. There was a good agreement with experiment and theoretical DCSs. The agreement clearly demonstrates the ability to model both theoretically and experimentally the inelastic scattering of O_2 molecule with rare gases.

Samenvatting

Dit proefschrift beschrijft het experimentele werk en de studie naar de inelastische verstrooiing van astrofysisch belangrijk koolstofmonoxide (CO) en moleculair zuurstof (O_2) met edelgassen.
Deel 1 van het proefschrift beschrijft het astrofysische belang van CO en O_2. CO is het meest voorkomende koolstof houdende molecuul in het heelal. CO is een hoofdbestanddeel van de vorming van methanol, dat vaak wordt beschreven als een belangrijke bouwsteen van het heelal. Wetenschappers, zoals astrofysici en astrochemici, gebruiken CO om het interstellair medium te traceren. O_2 is het belangrijkste molecuul in ons dagelijks leven. O_2 beschermt ons tegen het schadelijke ultraviolet (UV) van het zonnespectrum. O_2 is een homo nucleair molecuul en daardoor moeilijk te detecteren. Recente detectie van O_2 in het interstellair medium heeft veel wetenschappers aangetrokken, vooral degene die op zoek zijn naar leven buiten moeder aarde. Deze wetenschappers gebruiken de studie naar inelastische verstrooiing van CO en O_2 om hun astrofysische data te modelleren, waarin een nauwkeurige potentieel energie oppervlak (PES) van belang is. De (hoek distributie of differentile botsing/werkzame doorsnede) (DCS'en) uit onze experimenten worden (gebruikt om de PES's te testen) vergeleken met de theoretische DCS'en, die berekend zijn uit PES'en.
Deel 2 beschrijft de gekruist moleculair bundel experimenten die we gedaan hebben om rotatie-excitatie van CO en O_2 te onderzoeken door verstrooiing met Argon (Ar) en Helium (He). Hiervoor wordt velocity map imaging (VMI) gecombineerd met een toestand selectieve detectie methode, namelijk $(2 + 1)$ en $(1 + 1^{'} + 1^{''})$ resonantie versterkte multi-foton ionisatie (REMPI). DCS'en worden afgeleid uit de experimentele beelden. Deze DCS'en worden vergeleken met de DCS'en verkregen uit theoretische berekeningen. De nadruk is gelegd op hoek afhankelijkheidsmetingen vande, door botsing veroorzaakte, impuls moment polarisatie en laten zien dat vooral de (detectie met) VUV sonde gevoelig is voor deze impuls moment effecten. Hiervoor is een VUV lichtbron gemaakt, dat gebruik maakt van een resonante "four-wave difference frequency mixing" techniek in Xenon (Xe) gas wat resulteert in een scangebied tussen de 150 en 154 nm. Vervolgens ishet verstrooide (gebotste) product gedetecteerd met horizontaal en verticaal gepolariseerd VUV laser licht.

Deel 3 beschrijft een nieuwe manier om uit de VMI plaatjes/afbeeldingen de impuls moment polarisatie van inelastische vertrooiing (botsing te extraheren) te analyseren. Met eenvoudige functies is het mogelijk om de polarisatie moment direct uit het verschil van plaatjes te halen die respectievelijk bij horizontaal en verticaal gepolariseerd licht zijn gemeten. In hoofdstukken 4 en 5 wordt de verstrooiing/botsing tussen CO met Ar/He dat met de VMI techniek is gemeten gepresenteerd. Rotatie gexciteerde CO moleculen worden gedetecteerd met toestand selectieve detectie door middel van $(1 + 1^{'} + 1^{''})$ REMPI. De DCS'en verkregen uit de verschillende polarisaties van het VUV licht worden ook polarisatie afhankelijke PDS'en (PDDCS'en) genoemd. De VMI plaatjes van horizontaal en verticaal gepolariseerd VUV laser licht, van zowel het CO-Ar en CO-He botsingssysteem, laten een duidelijk verschil zien wat duidt op een sterk impuls moment polarisatie effect.
Deel 4 beschrijft de toestand-tot-toestand of 'state-to-state' inelastische verstrooiing van O_2 met He met een botsingsenergie van 660 cm^{-1}. De VMI techniek is gecombineerd met toestand selectieve ionisatiedetectie van O_2 met een (2+1) REMPI methode. Hierna worden de DCS'en afgeleid voor 6 zes verschillende eindtoestanden van O_2, hieruit blijkt dat de experimentele en theoretische DCS'en heel goed met elkaar overheen komen. De grote overeenkomst toont duidelijk de mogelijkheid aan om zowel experimenteel als theoretisch inelastische verstrooiing van O_2 met edelgassen te modelleren.

Curriculum Vitae

2014 - present	Design Engineer (Optical performance & Integration, CO_2 laser expert). Company: ***ASML***
2010- 2014	PhD Student at the Department of Molecular and laser physics, Radboud University Nijmegen. **Title thesis**: ***Inelastic scattering studies of CO and*** O_2 ***for Astrophysical applications***
2008 - 2010	Master of Science in Physics, Indian Institute of Technology(IIT), Guwahati, Assam, India. **Master Thesis**: ***Pulsed laser ablation of Titanium in ambient Oxygen: Formation of Titanium oxide***
2005 - 2008	Bachelor of Science (Physics Hons.), Banaras Hindu University (BHU), Varanasi , India

Publications

Direct extraction of alignment moments from inelastic scattering images.
Arthur G. Suits, **Chandan Kumar Bishwakarma**, Lei Song, Gerrit C. Groenenboom, Ad van der Avoird, and David H. Parker
The Journal of Physical Chemistry A, 119(23):5925-5931 1089-5639, 2014

Inelastic Scattering of CO with He: Polarization Dependent Differential State-to-State Cross Sections
Lei Song, Gerrit C. Groenenboom, Ad van der Avoird, **Chandan Kumar Bishwakarma**, Gautam Sarma, David H. Parker, and Arthur G. Suits
The Journal of Physical Chemistry A 119, 12526-12537 (2015)

State-to-state inelastic scattering of O_2 *with helium*
Chandan Kumar Bishwakarma, George van Oevelen, Roy Scheidsbach, David H. Parker, Yulia Kalugina, and Franois Lique
The Journal of Physical Chemistry A, 120(6):868-874, 2016.

State-to-state resolved differential cross sections for rotationally inelastic scattering of ND_3 *with He*
Ondrej Tkac, Ashim Kumar Saha, Jolijn Onvlee, Chung-Hsin Yang, Gautam Sarma, **Chandan Kumar Bishwakarma**, Sebastiaan Y. T. van de Meerakker, Ad van der Avoird, David H. Parker* and Andrew J. Orr-Ewing
Phys. Chem. Chem. Phys., 2014,16, 477-488

Collision Energy dependence of state-to-state Differential and Relative Integral Cross Sections for Rotationally Inelastic Scattering of H_2O *by He*
Gautam Sarma, Ashim Kumar Saha, **Chandan Kumar Bishwakarma**, Roy Scheidsbach, Chung-Hsin Yang, David Parker, Laurent Wiesenfeld, Udo Buck, Lazaros Mavridise and Sarantos Marinakis
Phys. Chem. Chem. Phys., 2017,19, 4678-4687

Future upcoming Publications

Inelastic Scattering of CO with Ar: Polarization Dependent Differential State-to-State Cross Sections
Chandan Kumar Bishwakarma, Gautam Sarma, David H. Parker, Arthur G. Suits, Lei Song, Gerrit C. Groenenboom and Ad van der Avoird,

State-to-state inelastic scattering of O_2 *with* H_2
Chandan Kumar Bishwakarma, George van Oevelen, Roy Scheidsbach, David H. Parker, Yulia Kalugina and Franois Lique

Acknowledgments

"I slept and dreamt that life was joy. I awoke and saw that life was service. I acted and behold, service was joy"

—*Rabindranath Tagore*

Life is a journey full of collection of the moments and when you look them back, it brings your imagination alive of that particular time of the moment. On the day of 'Holi' (*Color festival of India*), during last semester at IITG, Prof. dr. A.K. Srinivasan informed me that Prof. dr. David H. Parker has called him for his feedback and he was positive to give me the Ph.D. opportunity. I am grateful for the support of Prof. dr. A.K. Srinivasan. This was one of the best gifts God could have given me at that moment of time. My heart was filled with joy not only because I can pursue higher studies but also I would be able to support my family, which was struck by financial crisis due to my brother's illness. I would like to thanks, Prof. dr. David H. Parker from bottom of my heart for giving a lifetime opportunity. My Ph.D. journey was full of learning and joy. This journey would not have been possible without the constant support of my supervisor Prof. dr. David H. Parker. You always encouraged us. You were always there for the help whenever we need something for our work. You always pointed out our mistakes as a good teacher so that we can improve on it.(*I have to improve my writing skills*) I am thankful for your guidance, patience and trust. Thank you for all the help you have given me with my Ph.D. research. Thank you for being my 'Guru'.

I joined my Ph.D. as a Marie Curie fellow as a part of the ICONIC (Imaging and Control in Chemistry) network within the seventh Initial Training Network of the European Union. It was a wonderful multicultural platform for young talents where we can interact, share and discuss our results. It was a great opportunity and pleasure to meet many fellow scientists (Andreas, Aneta, Bin, Balazs, David, Dimitrios, Eduardo, Gloria, Jaro, Martin, Mikael, Mohammad, Ondrej, Orla, Pavle) and to learn from them. I would like especially like to thanks, Martin Stei for his never dying effort to help in with ion source for ion-molecule reaction in our lab.

I would like to express my gratitude to the manuscript committee members, Prof. dr. Jos Oomens, Prof. dr. Mark Brouard and Prof. dr. Bas Y.T. van de Meerakker for the evaluation of my thesis.

Work becomes fun when you have wonderful colleagues. During my Ph.D. research I was lucky enough to have some wonderful colleagues. Without their support, it would have been a difficult journey. I would like to thanks Magda Speijers for letting us not worry about any administrative work. I would like to thanks, late Leander Gerritsen for his technical support for my research experiments. Whenever I needed him he was always available for help. Our electronics 'wizard' Peter's magic touch on laser was often needed to fix laser problem. I am grateful for your support. I would like to thanks, Roy Scheidsbach, Jolijn Onvlee, Alex von Zastrow and George van Oevelen for their help and support. I hereby thank all the colleagues within the department "Molecule and Laser Physics" for their presence, guidance, encouragement and all which certainly provided me a very pleasant working atmosphere.

I would especially like to thanks, Gautam Sarma for his constant help and guidance in the experimental work. He taught me crossed-beam experimental setup workings and how to align a laser. Apart from experimental work, I learned photography from him. Gautam was our gadget master. My thanks to Dr. Andre Eppink for many useful discussions and help. I have to admit that Andre can handle spicier Indian food than me.

With presence of Raj and Ashim, l realized that life could be so colorful. They made me feel like at home during my stay in Nijmegen. We played cricket together and very often we prepare Indian food (Idli, Biryani, Mutton curry and Ashim special chai) together. Raj (the fast bowler) had always cricket controversy with Ashim (the athletic all rounder) and as usual I (the Batsmen) used to enjoy these cricket controversies. The next day every thing was sorted out automatically. We played together for Quick 1888 cricket club.

I cannot imagine this Ph.D. journey without constant support and effort from Dr. Rachna Pandey. She always pushed me to complete my thesis. Whenever I lost my track, she will pull me back on the right track. I will say she is the charming gardener who makes my soul blossom. If innocence and simplicity have to be personified then it will take the form of you.

I cherish the time, which I spent in Nijmegen with friends. It provided a work-life balance and made me feel like home. Let's start with our lunch group (Sudip da, Anup bhaiya, James, Ashim, Raj, Anil, Asha, Chandra di, Suresh, Gautam). It was really a refreshing break from our hectic work. I would like to thanks Anup, Rupali and Ritika. *(Thank you Anup bhaiya and bhabhi and my nanhi pari Ritika (Your Kaka always miss you))*, Anil, Asha and Shruti, *(It was always pleasant to meet you. It was even better when I met your daughter Shruti in Boston)* Shubra di & Nandini, *(Always an energetic inspirational multi talented gifted personality, looking forward to meet Nandini)*Pragnya,*(The evergreen diva of Nijmegen)* Kuntal & Agnes, *(Thank you Kuntal ji and Agnes for your evergreen support)* Lokesh *(The helping jugadu marwari, we met first time at Nijmegen McDonalds for our poetry performance for Diwali 1.0)* Sonny, *(you were always available for help)* Desouza Uncle Aunty, *(You both are absolutely wonderful)* Sisir, Amarnath, Vishnupriya, Bhawana, Aravind, Venkat, Aarthy, Manvendra, Swapneel, Kriti, Rahul, Suruchi, Prasenjit,*(Our multi talented Babu Mosai, thank you for singing my on-demand song, "Oh majhi re, dekhecho ki")* Papori, Ann, Payaswani, Suhas, Ashutosh, Rambir, Pooja, Princess Amaira, Arghya, Dipanwita, Prince Ayush, Neha and Nivesh.

I take this opportunity to thanks my ASML colleagues for their support. I would like to thanks Nelis Rutjes, *(Whenever I needed some days off for my thesis, I got it. I am lucky to have an inspirational manager like him)* Leon Teeuwen, *(He always asked me when is the book ready. Thank you for translating my thesis summary in Dutch)*

Edwin Meijer, *(Whenever I need help, he always stood behind me)* Frank Valkenaars, Rob Verstappen, Frans Tille, Erwin van der Sterren, Veerendra Gudduru *(Thanks for giving me your timely advise)*, Sergiy Osylak, Karen Mu, Sukumar Rudra.

I would also like to thanks, Prof. dr. Wim van der Zande. Whenever he sees me in ASML canteen, he always asked me about the thesis. I always admire him as a scientist.

Finally, I would like to express my deepest regards to my closest family members. I would like to thanks, my brothers Anand and Sawan for their selfless support. I am proud of you. I wish you both a great, successful and happy life ahead. God bless you. Words are powerless to express gratitude for my parents. My parents are my first "Guru". What I am is because of blessings from you. You 'll be with me like a handprint on my heart.

List of Acronyms

CM	Center of mass frame
CIA	Collision induced alignment
CCD	Charged coupled device
DAVIS	Data acquisition and visualization software
DCS	Differential cross section
HIP	Horizontal in-plane
HOOP	Horizontal out-of-plane
ICS	Integral cross sections
IMSIM	IMage SIMulation
KM	Kinematic apse
LTE	Local thermodynamic equilibrium
MCP	Micro channel plate
PDDCS	Polarization dependent differential cross section
PES	Potential energy surface
REMPI	Resonance enhanced multi photon ionization
TOF	Time of flight
UV	Ultra violet
VIP	Vertical in-plane
VMI	Velocity Map Imaging
VOOP	Vertical out-of-plane
VUV	Vacuum ultra violet